

NOTE TO USERS

The original manuscript received by UMI contains pages with slanted print. Pages were microfilmed as received.

This reproduction is the best copy available

UMI

A Fast and Accurate Analysis of High Q Patch
Resonators

by

Alireza Torabian-Esfahani

A thesis
presented to the University of Waterloo
in fulfilment of the
thesis requirement for the degree of
Doctor of Philosophy
in
Electrical Engineering

Waterloo, Ontario, Canada, 1998

©Alireza Torabian-Esfahani 1998



National Library
of Canada

Acquisitions and
Bibliographic Services

395 Wellington Street
Ottawa ON K1A 0N4
Canada

Bibliothèque nationale
du Canada

Acquisitions et
services bibliographiques

395, rue Wellington
Ottawa ON K1A 0N4
Canada

Your file *Votre référence*

Our file *Notre référence*

The author has granted a non-exclusive licence allowing the National Library of Canada to reproduce, loan, distribute or sell copies of this thesis in microform, paper or electronic formats.

The author retains ownership of the copyright in this thesis. Neither the thesis nor substantial extracts from it may be printed or otherwise reproduced without the author's permission.

L'auteur a accordé une licence non exclusive permettant à la Bibliothèque nationale du Canada de reproduire, prêter, distribuer ou vendre des copies de cette thèse sous la forme de microfiche/film, de reproduction sur papier ou sur format électronique.

L'auteur conserve la propriété du droit d'auteur qui protège cette thèse. Ni la thèse ni des extraits substantiels de celle-ci ne doivent être imprimés ou autrement reproduits sans son autorisation.

0-612-32864-3

The University of Waterloo requires the signatures of all persons using or photocopying this thesis. Please sign below, and give address and date.

Abstract

With the advent of high-temperature superconductivity, it is now possible to construct very high Q patch resonators. Because of their light weight, small volume and low expense, they are widely used for satellite communications.

In high Q filters, say $Q > 100$, one in fact requires accurate analysis, with an error of less than 1%. Such accuracy is normally not attainable by regular numerical methods, such as moment method, for most arbitrarily shaped patches. Such accuracy is attainable by two-dimensional (2D) methods, like modal or contour integral, where a magnetic wall is considered at the edge of the structure.

This research starts with a fast 2D method, and analyzes a patch considering a magnetic wall at the edge. Then the magnetic wall assumption is removed to include the fringing field effect. This new formulation is three dimensional (3D), and is based on a variational expression which guarantees the accuracy. Our modeling is based on adding a correction term in the form of a line integral to a 2D method. This new hybrid (2D/3D) method has the speed of computation for 2D methods and the higher accuracy of regular numerical 3D methods.

To reduce the effect of circuit connection on the performance, gap coupling is used in most high Q filters. In this work gap coupling is analyzed, and for a special kind of gap structure a novel model is presented. This model is then added to our hybrid method to analyze gap coupled patch resonators.

The new hybrid method is then extended to analysis of coupling between different patches. Compared with conventional numerical methods, our formulation is more accurate and faster. Using this analysis, we are able to analyze high order filters such as Chebyshev.

Acknowledgments

The author would like to express his sincere gratitude and appreciation to his supervisor Professor Y.L. Chow. His guidance, criticism, and kind advice in various steps of this research have been essential to the successful completion of the work. His deep physical insight into the problem helped the author to start and continue this research.

The author wishes to thank Professors R.H. MacPhie, S.K. Chaudhuri and W.P. Huang for all they taught him during stay at Waterloo, and for their fruitful comments on this work. This tribute extend to other members of the Ph.D. examination committee, Prof. L. Shafai, Prof. S. Safavi-Naeini, Dr. R.R. Mansour and Prof. D. Hemming.

The assistance of the ComDev in Cambridge, Ontario, in providing the Sonnet results and some circuit layouts is acknowledged, particularly the helpful comments and guidance of Dr. R.R. Mansour, and the help of Mr. Soeren Peik.

A special gratitude is reserved for Professor S. Safavi-Naeini whose excellent skills in teaching Electromagnetics have developed the author's interest in this field, and encouraged him to pursue this area of research.

The author would like to thank Dr. R. Faraji-Dana for helping him to develop a program for moment method. Thanks are also due to Dr. N. Hojjat and Dr. A. Omar to develop programs on Complex images and contour integral.

Last and foremost, the author would like to thank his wife for her love and devotion throughout the rough Ph.D. journey. Her patience, understanding and moral support helped the author to overcome the difficulties of the work during the various stages of this research. The author send his love to his little son, Parsa, who entered the joy to his life.

To my wife and little son, Parsa,
To my late mother and my father.

Contents

1	Introduction	1
1.1	Motivation	1
1.2	Definition of the problem	3
1.3	Existing Methods	4
1.3.1	Planar Circuit Methods - <i>2D</i> Methods	5
1.3.2	Integral Equation Technique - <i>3D</i> method	9
1.4	Our New Method	10
1.5	Organization of Thesis	11
2	Available Methods	14
2.1	Introduction	14
2.2	Modal Analysis - <i>2D</i> Method [12]	16
2.3	Multiport Network Method - <i>2D</i> Method	21
2.3.1	Segmentation method	23
2.3.2	Desegmentation method	26

2.4	Contour Integral Method - 2D Method	28
2.5	Moment Method - 3D Method	31
3	New Hybrid Method	34
3.1	Introduction	34
3.2	Our Proposed Method	35
3.2.1	The Cavity with Magnetic Wall - 2D formulation	35
3.2.2	The Cavity with Magnetic Wall - 3D formulation	36
3.2.3	The Patch - Cavity without Magnetic Wall	37
3.3	Numerical Results	40
3.3.1	One Port Circuit, Patch Antenna	41
3.3.2	2 Port Canonical Shape Filters	43
3.3.3	Dual Mode Filters	50
3.3.4	Multiport circuits, Power divider	52
4	Gap Coupling	55
4.1	Introduction	55
4.2	Modeling of the Gap	57
4.2.1	Parameters of the Transmission Line	58
4.2.2	Symmetrical Gap	62
4.3	Effect of Ground Plane and Finite Dielectric	65
4.4	Numerical Results	66

5 Coupling between Patches	71
5.1 Introduction	71
5.2 Hybrid Method	72
5.2.1 Cascaded Blocks	73
5.2.2 Mutual Couplings	77
5.3 Numerical Results	80
5.3.1 Chebyshev Filter	80
5.3.2 Elliptic Filter	88
6 Simulated Images	92
6.1 Introduction	92
6.2 Green's Functions of Multilayer Structure	94
6.3 Simulated Images Technique	96
6.4 Numerical Results	98
6.4.1 Microstrip Structure	99
6.4.2 Multilayer Structure	102
7 Conclusion and Future Work	107
7.1 Conclusion	107
7.2 Future Work	109
A Expansion of Green's Function by Eigenfunctions	112
B Weber's Solution Using Cylindrical Waves	115

C	2D Green's Functions of Regular Patches	118
C.1	Rectangular Patch	119
C.1.1	Z-matrix of a Rectangular Patch	119
C.2	Circular Patch	120
C.3	Annular Ring	120
C.4	Circular Sector	121
C.5	Annular Sector	122
C.6	Equilateral Triangle	123
C.7	Right-Angled Isosceles Triangle	123
C.8	30° – 60° Right-Angled Triangle	124
D	Green's Functions	125
	Bibliography	128

List of Figures

1.1	General structure of a planar circuit.	3
1.2	Other methods of feed for patch (a)Coaxial line feed (b)Gap coupling.	4
1.3	Example of approximation of curved boundary.	10
2.1	The structure of a canonical shaped planar circuit.	16
2.2	(a) Planar circuit, composite of two canonical shapes, can be analyzed by segmentation method (b) Non-canonical planar circuit which will have a canonical shape by adding a canonical shape, can be analyzed by desegmentation method.	22
2.3	Port names in the segmentation method	24
2.4	Planar circuit suitable to be analyzed by desegmentation method .	26
2.5	Configuration of arbitrarily shaped planar circuit.	29
3.1	The structure of patch filter.	36
3.2	The rectangular patch antenna.	42
3.3	Return loss of the rectangular antenna.	43

3.4	Rectangular patch filter.	44
3.5	The amplitude of S_{11} for the rectangular patch filter.	45
3.6	The amplitude of S_{21} for the rectangular patch filter.	46
3.7	Circular patch filter.	47
3.8	The amplitude of S_{11} for the circular patch	48
3.9	The amplitude of S_{21} for the circular patch	49
3.10	Dual mode patch filter.	50
3.11	The amplitude of S_{11} for the dual mode filter.	51
3.12	The amplitude of S_{21} for the dual mode filter.	52
3.13	Power divider	53
3.14	The amplitude of S_{11} for the power divider	54
3.15	The amplitude of S_{21} for the power divider	54
4.1	Ordinary structure of a gap coupling	56
4.2	General structure of a filter with gap coupling	57
4.3	Structure of the transmission line	58
4.4	Conformal mapping z & w plane	59
4.5	Impedance of line $Z_o(\Omega)$ for three kinds of substrate (ϵ_r)	63
4.6	Transmission Line with its dual	64
4.7	Dual mode filter with gap coupling	66
4.8	Return loss of gap coupled dual mode filter	67
4.9	Insertion loss of gap coupled dual mode filter	67

4.10	Gap coupled dual mode filter when longer stub is considered.	69
4.11	Gap coupled dual mode filter when longer stub is considered.	69
5.1	4-pole Chebyshev dual mode filter	73
5.2	Three blocks in 4-pole Chebyshev dual mode filter	74
5.3	2D contour integral method, and our 2D/3D method.	81
5.4	Insertion loss of one patch with direct coupling and gap coupling.	82
5.5	Insertion loss of filter with and without coupling between patches.	83
5.6	Results of S_{21} from our method and Sonnet.	84
5.7	Results of S_{11} from our method and Sonnet.	85
5.8	IE3D and Momentum results for the structure with radiation (no box).	86
5.9	S_{11} from IE3D and Momentum simulations.	87
5.10	4-pole Elliptic filter.	89
5.11	S_{21} for Elliptic filter from our method and Sonnet.	90
5.12	Results of S_{11} from our method and Sonnet.	91
6.1	Multilayer planar structure with embedded source.	95
6.2	Microstrip structure.	99
6.3	The amplitude of the vector potential A_{zz}	100
6.4	The amplitude of the scalar potential Q_z	100
6.5	The amplitude of images for A_{zz}	101
6.6	The amplitude of images for Q_z	102

6.7	Geometry of structure with 2-layer dielectric.	103
6.8	The amplitude of $\int A_{zz} dx$ for 2-layer dielectric structure.	104
6.9	The amplitude A_{zz} for 2-layer dielectric structure.	105
6.10	The amplitude Q_z for 2-layer dielectric structure.	106
C.1	Two port rectangular patch filter	119
C.2	(a) Circular Patch (b) Annular Ring	121
C.3	(a) Circular Sector (b) Annular Sector	122
C.4	Triangle patches, (a) Equilateral (b) Right-angled isosceles (c) $30^\circ - 60^\circ$ right-angled	124

Chapter 1

Introduction

1.1 Motivation

Microstrip structures are the most widely used form of the planar microwave circuits at the present time. They can be manufactured inexpensively in a compact form. However, they are lossy as compared to waveguides. This disadvantage, their loss, is not of major concern for many applications. The dominant loss mechanism in planar microwave circuits is conductor loss.

Since the discovery of high temperature superconductivity (HTS) capable of operating at temperatures above the boiling point of liquid nitrogen (77 K), a major effort has been expanded into the development of loss-free microwave planar circuits. The main advantage of using HTS for planar microwave filters lies in the fact that HTS planar circuits of small size and weight can realize a resonator with Q equal to or better than those achieved by bulky waveguide resonators. However, HTS circuits need a cooling system, and cannot handle as much power as waveguide circuits.

Applications such as space communication systems, radio telescopes and military infrared systems already utilize cryogenic cooling for various components. Therefore addition of HTS microwave circuits may be relatively simple and inexpensive. Properties of HTS microwave circuits, such as light weight and high Q , make them a proper candidate for satellite application.

In most communication systems, to fully utilize the allocated frequency spectrum, high Q filters with sharp cutoff are required. Using HTS in high Q filters would satisfy this requirement. For instance, in mobile communication, high Q filters are used for filter banks in cellular base stations [1].

When a microstrip circuit is realized with HTS, such as YBCO, on a substrate with high permittivity, such as lanthanum aluminate, $LaAlO_3$, the conductor loss becomes extremely small and the dominant losses are typically those due to radiation and surface wave modes [2]. The Q factor of 20000 or more was reported for these circuits in [3].

Due to the fact that HTS microstrip or strip line filters are not amenable to tuning or trimming mechanisms, we need a very accurate (i.e. error $< 1\%$) computer aided design and simulation tool. The available software packages use the numerical methods to analyze the circuit, and invariably they have at least two or three percents error in their analysis. Therefore, an alternate approach is sought to analyze the high Q circuits.

On the other hand an accurate method of analysis could be useful in design tools, if the analysis method is reasonably fast. Using such a method with an optimization method can provide a useful design package. Therefore, in addition to accuracy, the analysis should be fast.

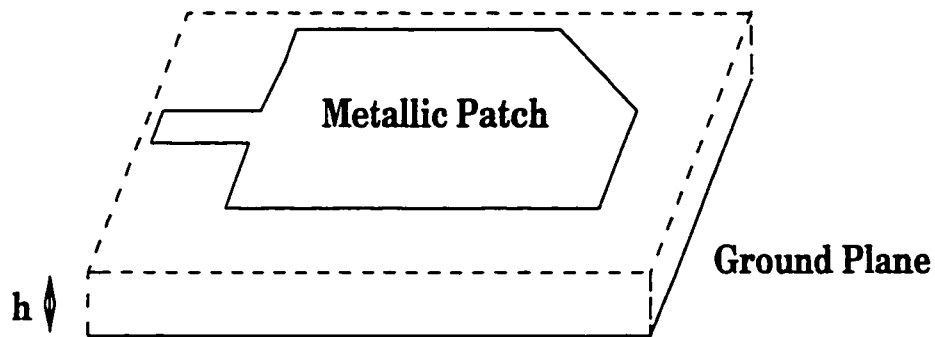


Figure 1.1: General structure of a planar circuit.

1.2 Definition of the problem

The general configuration of a microstrip filter is shown in Figure 1.1. The electromagnetic fields are concentrated between the metallic patch and the ground plane, so this structure acts as a cavity. We may approximate that the cavity is enclosed by a magnetic wall around the edge and two electric conductors at the top and bottom. If the slab is thin and the dielectric constant, ϵ_r , is high, the assumption of the magnetic wall is quite accurate. For low values of ϵ_r there will be radiation field from the edge of the cavity, therefore, we will have radiation loss. The other kind of loss, as mentioned earlier, is the conduction loss; it will be very low if HTS circuit is used. Therefore, a high Q should be realized with HTS on high dielectric constant substrate.

The patch resonator can be excited by different methods. A simple method is a microstrip transmission line directly connected to the edge of the patch as shown in Figure 1.1. A similar direct connection is a coaxial feed through the ground plane, as shown in Figure 1.2-a.

While a patch may have very high unloaded Q , such direct connections give a low loaded Q . Therefore, coupling may also be achieved by using loose capacitive

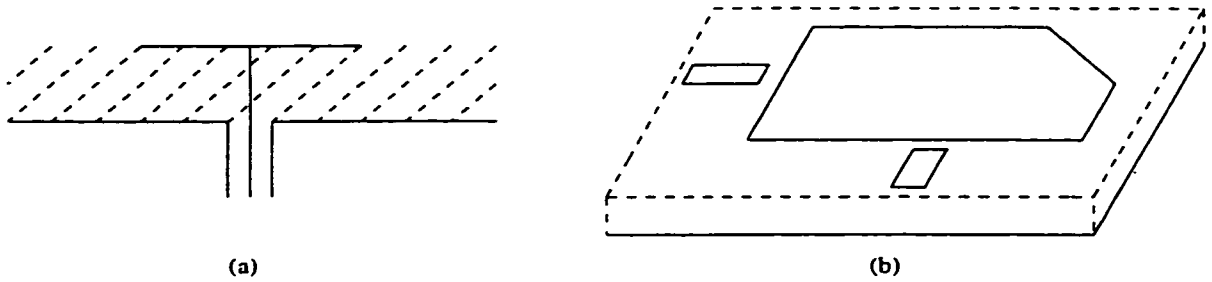


Figure 1.2: Other methods of feed for patch (a)Coaxial line feed (b)Gap coupling.

coupling between the patch and the line, Figure 1.2-b. In this case the impedance of the line feed has very low effect on the patch. Therefore, this kind of connection gives very high loaded Q and is useful for high Q patch resonators.

In this research, as a general planar structure, we consider the patch resonator as a N -port circuit having direct coupling, by microstrip line or coax line, or indirect capacitive coupling by gap. In this work, a new method is presented to analyze the patch with direct feed line or coax. The gap coupling is also included in the analysis using an accurate and simple model presented in this thesis.

1.3 Existing Methods

Patch resonators, like other microwave circuits, can be analyzed by different numerical methods as collected by Itoh [4], such as finite difference method [5], finite element method [6], transmission line matrix method [7], integral equation-moment method using three-dimension (3D) Green's functions [8], two-dimension (2D) planar circuit methods by Gupta [9, 10, 11], Okoshi [12] and others [13].

Numerical methods are chosen on the basis of trade-offs between accuracy, speed, storage requirement and are often structure dependent. For example, fi-

finite difference method and transmission line matrix method are usually suitable for closed structures and also need long computation time. The error in these numerical methods are around 5%. In this research, to have accurate results (less than 1 % error), we present a new method which is a combination of planar circuit method (*2D* analysis) and 3D moment method.

The most popular analyses of the microstrip patch resonators are planar circuit methods [9, 12](*2D* analysis) and integral-equation moment method [8, 14](*3D* analysis). However, microstrip structures were also analyzed using finite difference methods [15, 16]. In the following sections those two methods, *2D* and *3D* analyses, are briefly addressed.

1.3.1 Planar Circuit Methods - *2D* Methods

In patches, the height of substrate (say along z) is much smaller than the wavelength and the planar dimensions are comparable to the wavelength. Assuming no field variation along the height direction, these patches are called *2D* circuits by Okoshi [12] and the methods making use of this fact are called *2D* methods.

With the above assumption ($\partial/\partial z = 0$) the perfect magnetic wall can be considered around the edge of the patch [12]. Therefore, for regular shaped patches there are analytical solutions, and for irregular shapes a numerical solution is available based on contour integral formulation. These methods are simple and fast in comparison with *3D* methods. However, the fringe field is ignored in *2D* methods, and they are not accurate enough (error around 5%) for analyzing high Q circuits.

There are different *2D* methods in the literature, and most of them are briefly explained in this section.

Modal Method - Regular Shaped Patches

For canonical shaped patches the eigenfunctions (modes) of two dimensional wave equation can be analytically obtained under the patch. Gupta presented the eigenfunctions of triangular patch [10] circular sectors, annular rings and annular sectors [11] in strip line structure. Similar work was also done for microstrip structure [13]. The field and currents on the structure can be expanded in terms of the modes. Then, the input impedance of the circuit, or Z matrix of multiport circuit, is expressed in terms of the modes. This method is called modal analysis and can be used only for regular shaped patches [9, 12].

The simplicity of the modal method and its analytical solution are two advantages of this method. However, in some cases, we have to use a huge number of modes for convergence of solution and this makes the method very slow.

Contour Integral Method - Arbitrary Shape Patches

If the patch has an arbitrary shape, even with magnetic wall, the derivation of eigenfunctions is difficult. In this case the impedance matrix of the circuit can be obtained using the contour integral method developed by Okoshi [17] and Gupta [9]. In this approach, Green's theorem expressed in cylindrical coordinates and Weber's solution for cylindrical waves are used to convert the two-dimensional wave equation into a contour integral. The resulting contour integral relates the voltages and currents along the planar circuit periphery. Then, the impedance matrix can be found in terms of these contour integrals.

In 1988, the contour integral method was used [18] to analyzed prod-fed and strip-fed patch resonators. This method was also applied to planar devices in anisotropic media [19].

Multiport Network Methods (Segmentation - Desegmentation)

For the planar circuit with canonical shape, modal method can be used. On the other hand, analysis of planar circuits with completely arbitrary shapes, for which a Green's function (mode) cannot be obtained, can be done by contour integral method.

Between these two extreme cases, there is a class of planar circuits in which the shape of the circuit is a composite of simple configurations. In these cases, the 2D composite shapes can be decomposed into either all regular shapes or a combination of some regular shapes. The process of breaking down a composite shape into simpler shapes is called *segmentation* [17, 20].

The term segmentation refers to the network theoretic method for characterizing a combination of multiport components when the individual characteristics of each component is known. The implementation of this segmentation method may be carried out in terms of S, Z, or Y-parameters.

In addition to the segmentation method, there is also a complementary process called *desegmentation* [21], which is suitable for analyzing a special class of planar circuit configurations. These circuits cannot be decomposed into regular shapes, but by adding a regular shape, we end up with a regular shape. It has been shown [22] that if the impedance matrices of the added segment to the original configuration and the impedance matrix of the augmented configuration are known, the impedance matrix of the original planar circuit can be obtained using desegmentation formulation. This procedure is mainly used for 2D planar structures. Segmentation procedure can also be done in terms of Z, Y and S-matrices.

Other methods

Since 2D methods, modal or contour integral, are relatively simple and fast, some researcher tried to enhance these methods using other techniques.

In modal method, the assumption of the magnetic wall, the edge effect is not taken into account. In the 1960's Wheeler [23, 24] defined equivalent width for microstrip line using the (static field) conformal mapping to include the fringe field at the edge of the microstrip line. Some researchers [25] used the Wheeler's results and effective dielectric constant in modal analysis to include the effect of the fringe field in their analysis of the patch. This improvement is for the static field and therefore, is only an approximation. This method is very useful, if a few percent error can be tolerated in the results. However, the shape of frequency response around the resonant frequency may not be accurate.

Other researchers [26] used effective dielectric constant in 2D modal method to find the resonant frequency of a patch antenna. This is a fast and simple method to find resonant frequency. In most empirical equations, to include the fringe fields the effective dielectric constant has been used.

A more general method has been developed by Gupta and Abuzahra [27] to analyze planar circuits including the radiation, fringe fields and coupling. This method is called multi-network modeling (MNM). In this method the fields under the patch and the external fields (radiated, surface waves and fringe field) are modeled separately in terms of a multiport subnetwork. Then fields on both sides of an interface are matched at a discrete number of points. In this approach, the edge fields (fringing, surface wave and radiation) are modeled by introducing equivalent edge admittance networks (EAN) connected to the edges of the patch. This method was also developed to include the coupling between patches of a broad

band microstrip antenna[28]. In this case, an EAN is placed between two patches to include the coupling between patches.

1.3.2 Integral Equation Technique - 3D method

To consider the edge effect in patch resonators, for more accurate analysis, the integral equation method using 3D Green's function could be used. The speed of this 3D method is less than 2D methods.

In this method the boundary conditions are formulated in the form of integral equations. Mosig [29, 30] presented the formulation for mixed potential integral equation to be used in analyzing the microstrip structures. The integral equations can be solved by moment method [31] to find the currents on the structure. Then, from these currents the Z-matrix of the circuit can be calculated. This numerical method can analyze canonical or arbitrarily shaped patches considering the fringe field at the edges.

In 1995, Mittra et al [32] developed a method based on moment method integral equation method using closed form Green's function for multilayer structure, complex image technique developed by Chow et al [33]. In this work the accurate numerical analysis was presented, based on accurate Green's functions. They analyzed a patch resonator with an extra layer on the patch using the Green's function of a multilayer structure.

Using regular segmentation in moment method (e.g. each segment length = $\lambda/20$), we can get the results with 3 or 4 % error. This may count to 200 segments in a patch and therefore, the computation will be time consuming. Finer segmentation will substantially increase the computation time. In addition, sometimes it is not possible to fit each segment in moment method into a curved boundary of the patch,

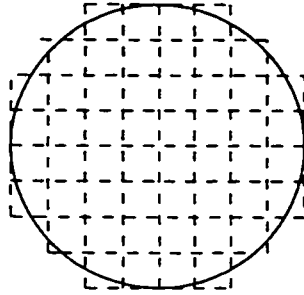


Figure 1.3: Example of approximation of curved boundary.

e.g. Figure 1.3. Therefore, there will be truncation error at the edge of patch.

Recently, in most of microwave circuit simulators, such as Maxwell/Ansoft or IE3D/Zeland, triangular segments are chosen near the edge. Therefore, a better approximation for the curved boundary of the patch is achieved. However, there is still truncation error at the edges. On the other hand the segments cannot be very small, because the coefficient matrix will be ill condition and it reduces the accuracy of the method. These two kinds of software are good for many application, however, they are not very accurate for structure with high dielectric, or high Q circuits.

The other commercial software, Sonnet, is also using moment method. This software is accurate, if its segmentation (grid) fits the structure. Sonnet is accurate enough and can be used for analyzing high Q circuits. However it is very slow.

1.4 Our New Method

In high Q circuits, we have to analyze the circuit very accurately (less than 1% error). The 2D methods, modal or contour integral, are fast and simple, as mentioned in Section 1.3.1. However, with magnetic wall assumption they do not consider the

fringe field. Therefore, the results of this method have errors more than 5 % which are not suitable for high Q circuits. As mentioned in Section 1.3.2, to consider the fringe field, a numerical method such as moment method with 3D Green's functions has to be used, e.g. Mittra [32]. However, the error of the results in this method is still around 3 %, and in some structures, such as circular patch or square patch with corner cut, there will be additional truncation error at the patch edge. In addition, this numerical method cannot be employed in design tools because of long computation time.

To overcome the above difficulties for analysis of high Q microstrip patch resonator, we present a novel method uses a combination of one of the above 2D methods and with 3D moment method. Each method is used to compensate the deficiency of the other one.

Our new method is a combination of 2D and 3D methods. This hybrid method starts with 2D method, contour integral or modal. Then, to include the fringe field, deletion of magnetic wall, we use a variational expression based on 3D Green's function. This variational expression increases the accuracy of our method.

Our method is very fast, because we use the fast convergent 2D methods for the main area of the patch, and accurate, because we use 3D Green's function and variational formulation to include the fringe field around the patch.

1.5 Organization of Thesis

The new method developed in this research is explained in Chapter 3. Analysis of gap coupling and coupling between patches, are explained as two major topics related to high Q planar filters. In this thesis, there is no separate chapter for

numerical results of our analysis. At the end of each chapter, some numerical results are presented.

A brief description of each chapter is given below.

Chapter 2 - As a basis of our method, we use two methods, *2D* and *3D* methods. In this chapter, these methods are explained in more details. There are also some details on the segmentation method which will be used in analysis of coupling between patches, Chapter 5. This chapter can be considered as background of our work. Since we have no contribution on its material, this chapter can be skipped, if the reader is familiar with these methods.

Chapter 3 - The major contribution of this research is presented in this chapter. Our new hybrid method is explained, and a number of planar structures are analyzed by our method. The new method is compared with different methods in terms of accuracy and speed.

Chapter 4 - This chapter focuses on patch resonators with gap coupling. A new model for gap coupling is presented in this chapter. This model of the gap is simple and accurate. To analyze high *Q* filters with gap coupling, this model of the gap is then added to our patch analysis presented in Chapter 3. A numerical result of our method is compared with other methods.

Chapter 5 - As a next step of this research, coupling between patches is studied. In this chapter, our new hybrid method is extended to analyze the coupling between patches in higher order filters. The segmentation method has also been used in this analysis.

Chapter 6 - In this chapter a new method is presented to calculate the 3D Green's functions of multilayer structures. This method is called *simulated images* and it can be considered as a simplified complex images method developed by Prof Y.L.

Chow and his associates in previous years. The simulated images method is used to calculate the magnetic field required in our hybrid methods presented in Chapter 3 and Chapter 5.

Chapter 7 - This chapter concludes the thesis by reviewing some of the important concepts of this research. As a future work, this chapter also proposes some areas which require more research.

Appendix A to C - These appendices present some of the mathematical proofs and derivation used in 2D analysis.

Appendix D - A closed form of Green's function of multilayer structures in frequency domain is listed in this appendix. Those formulas were extracted from previous works of researchers [34] in our group.

Chapter 2

Available Methods

2.1 Introduction

As microwave technology evolves toward the use of higher frequencies and more sophisticated circuits and components, a considerable theoretical effort is required in order to improve the characterization and modeling of microwave structures. In the set up of CAD techniques, usually one has to compromise between accuracy and simplicity. To achieve accurate results, when using numerical methods, such as moment method or finite difference method, a large number of computation and CPU time are required.

The available techniques for analyzing microstrip, or in general planar, circuits can be categorized into two broad classes: two dimensional field analysis techniques based on the planar waveguide model of microstrip and full wave three dimensional numerical analysis techniques.

The two-dimension (2D) approach includes a wide range of analyses such as modal analysis, multiport network technique, and contour integral method. In

modal analysis [9, 12] the Green's function as applied to planar components of regular shapes is expressed in terms of modes (eigenfunctions of wave equation) in the planar structure. This analysis yields impedance matrix characterization of the structure with reference to the number of ports that exist at selected locations on the edges of, or inside, the structure.

Multiport network techniques are also known as segmentation and desegmentation methods [20, 21]. These techniques have been developed for two dimensional analysis of microwave planar components, and microstrip antennas. These methods can also be applied to full wave analysis techniques (three dimensional fields) based on mode matching approach. Multiport network techniques are suitable for irregular shape structure composites of regular shapes.

Contour integral method allows analysis of generalized geometrical shapes unlike the modal method (for regular shapes) and multiport network techniques (for composites of regular shapes) [12].

The three-dimension (3D) approach can be divided into two categories: integral equation analysis and differential equation analysis. The integral equation approach employs moment method solution to find the current distribution on the metalization of a structure [29, 32]. Characteristics of the structure are derived from this current distribution. Both space domain and frequency domain formulation can be used.

Differential equation based analysis, such as finite-difference [16] or transmission line matrix (TLM) [7], have been used extensively for time domain analysis of microwave structures. These approaches are more generalized formulations, as compared to integral equation based methods, for incorporating vertically oriented currents in microwave structures, or structures in a closed region such as a box.

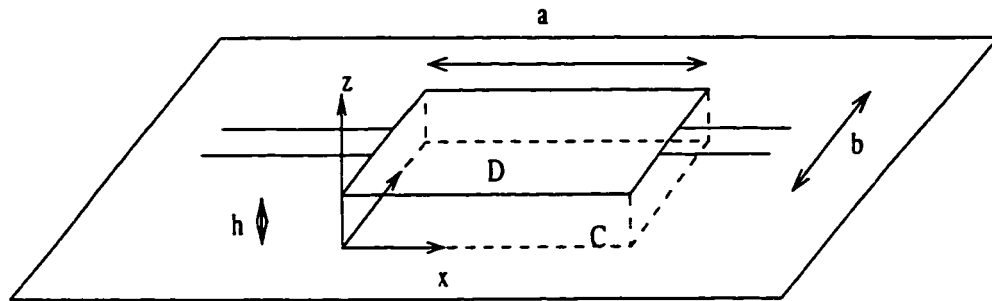


Figure 2.1: The structure of a canonical shaped planar circuit.

However, larger computer memory and run times are often needed.

In this chapter the modal method, contour integral method, and multiport network technique (segmentation - desegmentation method) are explained as the 2D analysis. Then, as a 3D analysis, the integral equation moment method is explained. These methods, one of the 2D methods and 3D moment method, will be the basis of our new hybrid method which is proposed in the next chapter. Segmentation method is also part of our analysis in Chapter 5, when the structure has more than one patch.

2.2 Modal Analysis - 2D Method [12]

Consider a thin canonical shaped conductor plate placed on top of a ground plane with a spacing h as shown in Figure 2.1 with several coupling ports having widths W_i, W_j, \dots . The rest of the periphery is assumed to be open-circuited. The x, y and z coordinates are shown in Figure 2.1. When the spacing h is much smaller than the wavelength and the dielectric is homogeneous and isotropic, we can assume that $\frac{\partial}{\partial z} = 0$ and $H_z = E_x = E_y = 0$. Therefore, Maxwell's equations are simplified to:

$$\frac{\partial H_y}{\partial x} - \frac{\partial H_x}{\partial y} = j\omega\epsilon E_z \quad (2.1)$$

$$\frac{\partial E_z}{\partial y} = -j\omega\mu H_x \quad (2.2)$$

$$\frac{\partial E_z}{\partial x} = j\omega\mu H_y \quad (2.3)$$

where ω, ϵ, μ are the angular frequency, permittivity and permeability of the substrate, respectively. Note that for the structure in Figure 2.1, the other remaining Maxwell's equations become trivial. From the above three equations, (2.1) to (2.3), we arrive at the following 2D Helmholtz equation, in terms of E_z within the planar circuit cavity

$$(\nabla_t^2 + k^2)E_z = 0 \quad (2.4)$$

where

$$k = \omega\sqrt{\mu\epsilon} \quad , \quad \nabla_t^2 = \frac{\partial^2}{\partial x^2} + \frac{\partial^2}{\partial y^2}$$

where k is the wavenumber in the substrate.

Next, we consider the boundary conditions. On the top and bottom plate if we denote the surface current density by \vec{J} , then

$$\vec{J} = \hat{n} \times \vec{H} \quad (2.5)$$

when $\hat{n} = \hat{z}$, we have,

$$H_y = -J_x \quad , \quad H_x = J_y$$

Therefore, we obtain from (2.1) and (2.5)

$$-\nabla \cdot \vec{J} = j\omega\epsilon E_z$$

On the peripheral magnetic wall, we first consider the case where no external circuit is connected to the periphery. Therefore, the boundary condition along the open boundary periphery of the circuit is

$$\frac{\partial E_z}{\partial n} = 0 \quad (2.6)$$

where n is the local coordinate pointing outward and normal to the periphery. If V denotes the voltage at each point of the circuit with respect to the ground conductors,

$$V = E_z h$$

therefore the problem to be solved is formulated as

$$(\nabla_t^2 + k^2)V = 0 \quad , \text{ in } D \quad (2.7)$$

$$\frac{\partial V}{\partial n} = 0 \quad , \text{ on } C \quad (2.8)$$

where C and D are the periphery and the region inside the periphery, respectively, as shown in Figure 2.1.

Equations (2.7) and (2.8) describe an eigenvalue problem. The nonzero solution of (2.7) exists only for an infinite number of discrete values of k . These values k_0, k_1, \dots are called eigenvalues, and they correspond to resonant angular frequencies $\omega_0, \omega_1, \dots$, where $\omega_i = ck_i$ (c the velocity of light). To each eigenvalues, k_i , a specific field solution Φ_i exists and is called the eigenfunction.

Now we consider the case where external ports are present. At the junction with external circuits, (2.8) is no longer valid. From (2.2), (2.3) and (2.5) we can say that if an external circuit having admittance Y is connected to this port, Y is related to the voltage V at the port as,

$$Y = \frac{\int_W J_n \cdot dl}{\frac{1}{W} \int_W V dl} = \frac{W \int_W H_s \cdot dl}{\int_W V dl} = \frac{-jW \int_W \frac{\partial V}{\partial n} dl}{\omega \mu h \int_W V dl} \quad (2.9)$$

where W is the width of the port, J_n is the inward surface current density and normal to the contour C , and H_s is the magnetic field intensity along C . All the above integrals are performed along the periphery C .

If the circuit has several ports, assuming that the widths of the ports are much smaller than the wavelength, we may define the terminal voltage v_i , and terminal current I_i as

$$v_i = \frac{h}{W_i} \int_{W_i} E_z dl \quad (2.10)$$

$$I_i = \int_{W_i} J_n dl \quad (2.11)$$

Using the voltage and current of each port, we can define the impedance matrix of the network. The elements of impedance matrix can then be defined as

$$Z_{ij} = \frac{v_i}{I_j} \quad (2.12)$$

To derive the expression for Z_{ij} , we use the Green's function of the structure, G , which has a dimension of impedance. This Green's function will be derived in terms of modes in the structure. The Green's function G , satisfies

$$V(x, y) = \int \int_D G(x, y | x_0, y_0) J(x_0, y_0) dx_0 dy_0 \quad (2.13)$$

where D is the region inside the structure, as shown in Figure 2.1. The open boundary condition for G is

$$\frac{\partial G}{\partial n} = 0 \quad \text{along } C \quad (2.14)$$

In planar circuits, current is injected from the periphery where coupling ports are present. We are usually concerned only with the voltage along the periphery,

we can express this voltage by a line integral in terms of current density along the periphery as

$$V(l) = \oint_C G(l|l_0) J_n(l_0) dl_0 \quad (2.15)$$

where l and l_0 are used to denote distance along C .

Since J_n is present only at coupling ports, the integral in (2.15) should be calculated only over the widths of the ports. Thus we can compute the terminal voltage defined in (2.10) directly from (2.15) as

$$\begin{aligned} v_i &= \frac{1}{W_i} \sum_j \int_{W_i} \int_{W_j} G(l|l_0) J_n(l_0) dl_0 dl \\ &= \sum_j \frac{I_j}{W_i W_j} \int_{W_i} \int_{W_j} G(l|l_0) dl_0 dl \end{aligned} \quad (2.16)$$

where

$$I_j = \int_{W_j} J_n(l_0) dl_0$$

I_j represents the current flowing into the j th port on the circuit plate. In deriving Equation (2.16), we assume that $W_i, W_j \ll \lambda$, and therefore G does not vary appreciably within W_i and W_j , so that the average value of GJ_n can be approximated as the product of the average of G and the average of J_n .

Equation (2.16) shows that the ij th element of the impedance matrix of a N -port planar circuit, i.e. $Z_{ij} = v_i/I_j$, is given by

$$Z_{ij} = \frac{1}{W_i W_j} \int_{W_i} \int_{W_j} G(l|l_0) dl_0 dl \quad (2.17)$$

When the shape of the circuit is canonical (e.g. rectangular or circular), we can obtain the Green's function of the wave equation analytically and derive the equivalent circuit parameters directly from that Green's function using (2.17). The

Green's function can be expressed in terms of eigenfunctions, Φ_n , and eigenvalues, k_n , as

$$G(x, y|x_0, y_0) = j\omega\mu h \sum_n \frac{\Phi_n(x_0, y_0)\Phi_n(x, y)}{k_n^2 - k^2} \quad (2.18)$$

The details of how to derive the above Green's function can be found in some literatures [9, 12], and is briefly given in Appendix A. In Appendix C, the Green's function for some simple shapes is given based on the eigen function expansion (2.18). As mentioned before, derivation of Φ_n is practical only for canonical shapes. The list of canonical shapes with their eigenfunctions and eigenvalues, Φ_n and k_n are given in [20].

Setting (2.18) into (2.17), we find that element of the impedance matrix is expressed as

$$Z_{ij} = \frac{j\omega\mu h}{W_i W_j} \int_{W_i} \int_{W_j} \sum_n \frac{\Phi_n(l_0)\Phi_n(l)}{k_n^2 - k^2} dl_0 dl \quad (2.19)$$

The above equation shows that the term having k_n closest to k is the dominant term. Therefore, when we are concerned only with the circuit characteristics at frequencies close to the resonance point, we can simply use the predominating term from (2.19) to simplify the analysis.

2.3 Multiport Network Method - 2D Method

Modal analysis of two dimensional planar components with regular shapes has been presented in the last section. On the other hand, analysis for planar circuits with completely arbitrary shapes, for which modal expansions of Green's function cannot be obtained, is discussed in the next section.



Figure 2.2: (a) Planar circuit, composite of two canonical shapes, can be analyzed by segmentation method (b) Non-canonical planar circuit which will have a canonical shape by adding a canonical shape, can be analyzed by desegmentation method.

Between these two extreme cases, there is a class of planar circuits which the shape of the circuit is a composite of canonical configurations, or removal of a canonical shape from another canonical shape. Examples of these two types of this class of circuits are shown in Fig. 2.2a and 2.2b. The method of analysis for these structures are called *segmentation* and *desegmentation* [17, 20].

These two terms, segmentation and desegmentation, refer to the network methods for characterizing a combination of multiport components when the characteristics of each component is known. The implementation of these methods can be carried out in terms of S-parameters, Z-parameters or Y-parameters. Since we present other methods of analysis based on Z-parameters, these methods are explained based on Z-parameters.

These methods have been used extensively for analyzing the two-dimensional planar circuits. As major 2D methods, and because of their application in our work in Chapter 5, these methods are briefly explained.

2.3.1 Segmentation method

The name of this method, segmentation, has been given by Okoshi and his colleagues [17]. The idea of this method is to divide a circuit configuration into simpler segments which have regular shapes. The segmentation method gives us the overall characteristic of the circuit when the characterization of each segment is known. This is the main advantage of this method, and we do not need to analyze the whole circuit. On the other hand, couplings between segments are not considered in this method.

The basis of the segmentation approach is the transformation of the field matching along the interface between two regions into an equivalent network connection problem. Matching of the tangential magnetic field is realized by the current continuity condition enforced by Kirchoff's current law. The continuity of the tangential electric field is achieved by enforcing equivalence of voltages at the connected ports. Therefore, the electromagnetic field problem is solved in terms of an equivalent network interconnection problem.

Recently, the segmentation approach has also been applied to three dimensional electromagnetic problems, such as full wave analysis of via hole ground in microstrip [35]. In these cases, the structure is divided into various regions sharing common interfaces. A network characterization of each region is obtained in terms of say Z matrices. These matrices are then connected together by the segmentation procedure to enforce the continuity of currents at the interface which corresponds to the continuity of the tangential components of magnetic fields at the boundary.

The segmentation method was originally formulated in terms of S matrices of each segments by Okoshi; however, it was found that a Z matrix formulation is more efficient for microwave planar circuits. In this section, the segmentation method is

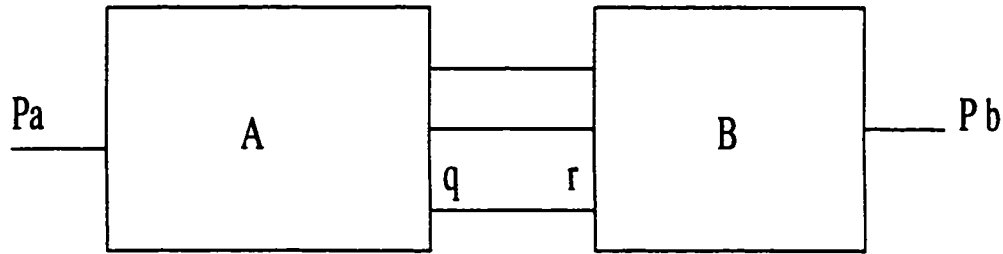


Figure 2.3: Port names in the segmentation method

described based on Z matrix formulation.

This method can be explained by considering the connection of the two segments in Fig. 2.3. As shown in the figure, The ports of segment A on the common boundaries with segment B are called q -ports. The corresponding ports on segment B are called r -ports. The ports on segment A and B which are not on the common boundaries are called p_a and p_b ports, respectively. The Z matrices of segments A and B can be arranged as,

$$Z_A = \begin{bmatrix} Z_{p_a p_a} & Z_{p_a q} \\ Z_{q p_a} & Z_{qq} \end{bmatrix} \quad (2.20)$$

$$Z_B = \begin{bmatrix} Z_{p_b p_b} & Z_{p_b r} \\ Z_{r p_b} & Z_{rr} \end{bmatrix} \quad (2.21)$$

The above Z matrices can be written together as,

$$\begin{bmatrix} V_p \\ V_q \\ V_r \end{bmatrix} = \begin{bmatrix} Z_{pp} & Z_{pq} & Z_{pr} \\ Z_{qp} & Z_{qq} & 0 \\ Z_{rp} & 0 & Z_{rr} \end{bmatrix} \begin{bmatrix} I_p \\ I_q \\ I_r \end{bmatrix} \quad (2.22)$$

where

$$V_p = \begin{bmatrix} V_{p_a} \\ V_{p_b} \end{bmatrix}, \quad I_p = \begin{bmatrix} I_{p_a} \\ I_{p_b} \end{bmatrix} \quad (2.23)$$

and

$$Z_{pp} = \begin{bmatrix} Z_{p_a p_a} & 0 \\ 0 & Z_{p_b p_b} \end{bmatrix}, \quad Z_{pq} = \begin{bmatrix} Z_{p_a q} \\ 0 \end{bmatrix}, \quad Z_{pr} = \begin{bmatrix} 0 \\ Z_{p_b r} \end{bmatrix} \quad (2.24)$$

As a result of the interconnections of q and r ports, we can write,

$$V_q = V_r \quad \text{and} \quad I_q = -I_r \quad (2.25)$$

Substituting (2.25) into (2.22) to eliminate V_q , V_r , I_q and I_r , we obtain,

$$V_p = [Z_{AB}]I_p \quad (2.26)$$

where

$$[Z_{AB}] = \begin{bmatrix} Z_{p_a p_a} & 0 \\ 0 & Z_{p_b p_b} \end{bmatrix} + \begin{bmatrix} Z_{p_a q} \\ -Z_{p_b p_b} \end{bmatrix} [Z_{qq} + Z_{rr}]^{-1} [-Z_{qp_a}, \quad Z_{rp_b}] \quad (2.27)$$

It should be noted that higher accuracy can be obtained by increasing the number of ports, i.e. q , on the common boundary. From the computational point of view, the most time consuming step is the evaluation of the inverse of the matrix of size $(q \times q)$, interconnected ports. Therefore, there is a trade off between speed and accuracy.

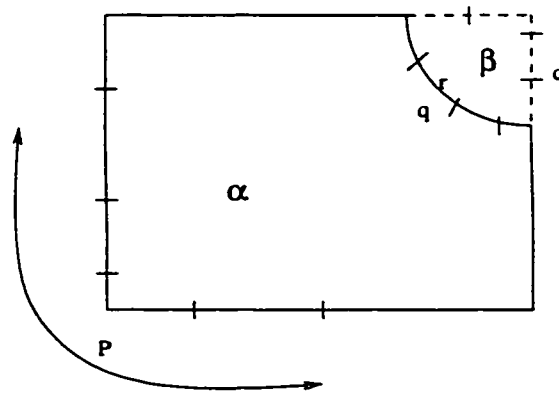


Figure 2.4: Planar circuit suitable to be analyzed by desegmentation method

2.3.2 Desegmentation method

The desegmentation method is a complementary method used for two dimensional circuits. This method is applicable in cases where the addition of one or more regular shapes to the shape of the circuit yields another regular shape, such as Fig. 2.4. This method was developed by Gupta [21, 20] in terms of S matrices or Z matrices. In this section, this method is briefly explained based on Z matrices.

As shown in Figure 2.4, let α denote the shape of the circuit to be analyzed. On the addition of one or more simple shape, called β , a simple shape γ is obtained. The Z parameter of β and γ can be found using modal method explained in last section. The ports of α which are not on common boundaries between α and β are called p ports. The port of α on common boundaries between α and β are called q ports. The ports of β are called r when they are on the common boundary, and called d when they are not.

The Z matrices for β and γ , Z^β and Z^γ , can be evaluated using modal method as,

$$\begin{bmatrix} V_r \\ V_d \end{bmatrix} = \begin{bmatrix} Z_{rr} & Z_{rd} \\ Z_{dr} & Z_{dd}^\beta \end{bmatrix} \begin{bmatrix} I_r \\ I_d \end{bmatrix} = Z^\beta \begin{bmatrix} I_r \\ I_d \end{bmatrix} \quad (2.28)$$

and

$$\begin{bmatrix} V_p \\ V_d \end{bmatrix} = \begin{bmatrix} Z_{pp} & Z_{pd} \\ Z_{dp} & Z_{dd}^\gamma \end{bmatrix} \begin{bmatrix} I_p \\ I_d \end{bmatrix} = Z^\gamma \begin{bmatrix} I_p \\ I_d \end{bmatrix} \quad (2.29)$$

For the circuit to be analyzed, α shown in Figure 2.4, we have

$$\begin{bmatrix} V_p \\ V_q \end{bmatrix} = \begin{bmatrix} Z_{pp}^\alpha & Z_{pq} \\ Z_{qp} & Z_{qq} \end{bmatrix} \begin{bmatrix} I_p \\ I_q \end{bmatrix} = Z^\alpha \begin{bmatrix} I_p \\ I_q \end{bmatrix} \quad (2.30)$$

where Z^α is to be found from Z^β and Z^γ defined in (2.28) and (2.29). As a result of connection of the q ports to the corresponding r ports, we have

$$V_q = V_r \quad (2.31)$$

and

$$I_q + I_r = 0 \quad (2.32)$$

Using the segmentation procedure, Z^γ can be expressed in terms of Z^α and Z^β .

With some arrangement of submatrices, the submatrices of Z^α can be found as,

$$Z_{qq} = -Z_{rr} - N \quad (2.33)$$

$$Z_{pq} = -Z_{pd} Z_{rd}^t (Z_{rd} Z_{rd}^t)^{-1} N \quad (2.34)$$

$$Z_{qp} = -N (Z_{dr}^t Z_{dr}^t)^{-1} Z_{dr}^t Z_{dp} \quad (2.35)$$

$$Z_{pp}^\alpha = Z_{pp}^\gamma - Z_{pd} (Z_{dd}^\gamma - Z_{dd}^\beta)^{-1} Z_{dp} \quad (2.36)$$

where

$$N = Z_{rd} Z_{rd}^t [Z_{dr}^t (Z_{dd}^\gamma - Z_{dd}^\beta) Z_{rd}^t]^{-1} Z_{dr}^t Z_{dr} \quad (2.37)$$

To have more accurate results, we may increase the number of q ports. However, this reduces the speed of calculation.

As mentioned before, this method can be use only for a special class of circuits, and cannot be applied to arbitrarily shaped planar circuit. The contour integral is a general method, and is explained in the next section.

2.4 Contour Integral Method - 2D Method

As opposed to the canonical shapes, we now consider an arbitrarily shaped planar circuit having several coupling ports as shown in Figure 2.5. Solving the wave equation (2.4) over the entire arbitrary area D inside the circuit periphery C will require a long computer time. However, when we are concerned only with voltage along the periphery, such a computation is not necessary. The wave equation can be converted into a contour integral form which relates the voltage and current along the circuit periphery.

Using Weber's solution for cylindrical wave, the potential at a point on the periphery is found to satisfy the following integral equation [9] (the details of the derivation are given in Appendix B).

$$v(s) = \frac{1}{2j} \oint [k \cos \Theta H_1^{(2)}(kr) v(s_0) + j\omega\mu h H_0^{(2)}(kr) J_n(s_0)] ds_0 \quad (2.38)$$

where

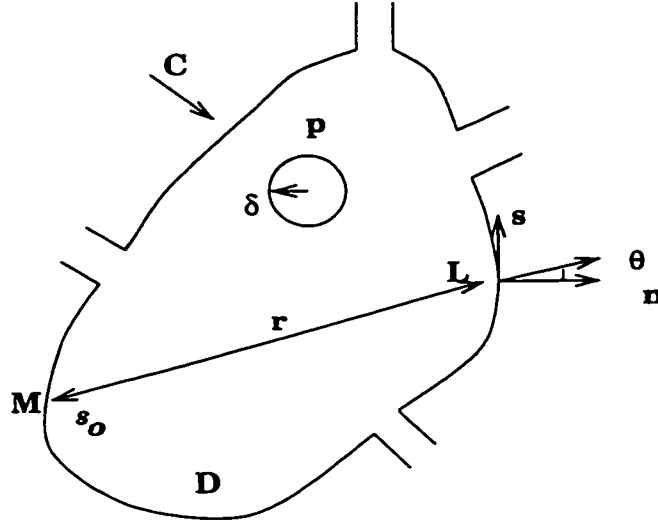


Figure 2.5: Configuration of arbitrarily shaped planar circuit.

- $H_0^{(2)}$ and $H_1^{(2)}$ are the zero-order and first-order Hankel functions of the second kind, respectively.
- $J_n(s_0)$ denotes the current density in a port flowing into the periphery.
- s and s_0 denote the distance along contour C . The variable r denotes distance between points M and L represented by s and s_0 .
- Θ denotes the angle made by the straight line from point M to point L and the normal at point L , as shown in Figure 2.5.

Equation (2.38) gives the relation between the voltage and current distributions along the periphery. When $J_n(s_0)$ is given, this equation is a Fredholm integral equation of the second kind in terms of the voltage. To solve (2.38) with moment method, we divided the circuit periphery into N segments numbered as $1, 2, \dots, N$, having widths W_1, W_2, \dots, W_N . Coupling ports are assumed to occupy a segment or if necessary, we may assume that a port occupies two or more segments.

When we assume that the magnetic current (i.e. electric field intensity) is constant over each width of these segments, the above integral equation results in a system of matrix equations as [12]

$$\sum_{j=1}^N u_{ij} V_j = \sum_{j=1}^N h_{ij} I_j \quad i = 1, 2, \dots, N \quad (2.39)$$

where

$$u_{ij} = \delta_{ij} - \frac{k}{2j} \int_{W_j} \cos \Theta H_1^{(2)}(kr) ds \quad (2.40)$$

$$h_{ij} = \frac{\omega \mu h}{2} \begin{cases} \frac{1}{W_j} \int_{W_j} H_0^{(2)}(kr) ds & i \neq j \\ 1 - \frac{2j}{\pi} (\ln(\frac{kW_i}{4}) - 1 + \gamma) & i = j \end{cases} \quad (2.41)$$

$$\delta_{ij} = \begin{cases} 1 & i = j \\ 0 & i \neq j \end{cases}$$

where $\gamma = 0.5772$ is Euler's constant. The second formula in Equation (2.41) has been derived by integrating the asymptotic expression of $H_0^{(2)}(kr)$ for $kr \ll 1$, assuming the i th segment is straight.

Solving (2.39), we can obtain the voltage on each sampling point as

$$V = U^{-1} H I \quad (2.42)$$

where V and I denote column vectors consisting of V_i and I_i , and U and H are $N \times N$ matrices consisting of u_{ij} and h_{ij} , respectively. If we consider that all N segments on the periphery are coupling ports and the planar circuit is represented by an N -port equivalent circuit, then, from the above relations, the impedance matrix of the equivalent N -port circuit is obtained as

$$Z = U^{-1} H \quad (2.43)$$

In practice, however, most of the N ports described above are open circuited. When external admittances are connected to several of them and the rest of the ports are left open circuited, the reduced impedance matrix can be derived without difficulty, by constructing the impedance matrix by choosing only necessary elements of (2.43).

2.5 Moment Method - 3D Method

The analysis of the patch filters like other MIC structures can be treated using the well known electric field integral equation (EFIE) technique. In this method, the 3D Green's functions are used and the fringe field is automatically included. However, this method is more complicated than 2D methods because of the calculation of 3D Green's functions.

In 1968 Harrington [14] introduced a modified EFIE, called the mixed potential integral equation (MPIE). The new formulation reduces the complexity of Green's function, however, two types of Green's function should be calculated. In this method the auxiliary magnetic vector potential \vec{A} and the scalar electric potential Φ represent the electric and magnetic fields intensities \vec{E} and \vec{H} .

$$\begin{aligned}\vec{H} &= \nabla \times \vec{A} \\ \vec{E} &= -j\omega\mu\vec{A} - \nabla\Phi\end{aligned}$$

Then the MPIE can be written as

$$\hat{n} \times \vec{E}^i(\vec{r}) = \hat{n} \times \left[j\omega\mu \int_s \vec{G}_A(\vec{r}|\vec{r}') \cdot \vec{J}_s(\vec{r}') ds' + \nabla \int_s G_q(\vec{r}|\vec{r}') \frac{\rho_s(\vec{r}')}{\epsilon} ds' \right] \quad (2.44)$$

where \vec{G}_A and G_q are Green's function for the vector and scalar potentials. The details of the Green's functions are given in [36, 34]. The frequency domain Green's function of multilayer structure is listed in Appendix D.

To apply EPIE or MPIE, we have to first compute the Green's functions, and then solve the integral equation by a numerical method. The first step can be done using the simulated image technique which is explained in Chapter 6 of this thesis. The resulting integral equation is most frequently solved using the moment method [14].

The integral equation for the patch filter problem can be represented in the operator form

$$L J = g \quad (2.45)$$

where L is the linear integral operator and J is the unknown current distribution on the patch (a conductor). On the right hand side g , represents the known excitation of the structure. The unknown current distribution J is expanded in terms of a suitable set of chosen *basis functions* J_n ,

$$J = \sum_{n=1}^N I_n J_n \quad (2.46)$$

where I_n are the unknown coefficients to be found. Now the operator equation (2.45) can be written as

$$\sum_{n=1}^N I_n (L J_n) = g \quad (2.47)$$

Define the *inner product* as

$$\langle f_1, f_2 \rangle = \int_s f \cdot g \, ds \quad (2.48)$$

By choosing an appropriate set of *weighting functions* w_m , one can take the inner product of (2.47) with these w_m to form a set of N linear equations. That is

$$\sum_{n=1}^N \langle w_m, L J_n \rangle I_n = \langle w_m, g \rangle \quad , \quad m = 1, \dots, N \quad (2.49)$$

or, in the matrix form

$$[Z_{mn}][I_n] = [V_m] \quad (2.50)$$

where

$$Z_{mn} = \langle w_m, LJ_n \rangle \quad (2.51)$$

and

$$V_m = \langle w_m, g \rangle \quad (2.52)$$

Since $[Z_{mn}]$ and $[V_m]$ are known, we may solve for the unknown current distribution on the patch from (2.50), then the scattering parameters of the circuit are computed. The details of how to choose the basis functions and weighting functions, as well as details on the derivation of Z_{mn} and V_m are given in [37]. The most time consuming part of the analysis is the calculation of the $[Z_{mn}]$ elements, (2.50). Based on MPIE formulation and applying method of moment, Z_{mn} has the following form [14],

$$\begin{aligned} Z_{mn} = & j\omega\mu\hat{l}_m\hat{l}_n \int \int J_m(s)G^A(s|s')J_n(s') ds ds' + \\ & \frac{1}{j\omega\epsilon} \int \int (J_{m+}(s) - J_{m-}(s))G^q(s|s')(J_{n+}(s') - J_{n-}(s')) ds ds' \end{aligned} \quad (2.53)$$

As it shows in (2.53), for each element of Z matrix, we have to calculate a few double surface integrals. Therefore, this method is very slow, especially when the number of segments is high.

This method could be used to analyze any kind of circuit, regardless of shape. This is the most important advantage of this method. On the other hand, this scheme is a numerical technique which typically gives a few percent error in the final results. Due to this fact, this method is not suitable for high Q circuits.

Chapter 3

New Hybrid Method

3.1 Introduction

In a communication system, to fully utilize the allocated frequency spectrum, narrow band filters with sharp transient edges are required. In planar microwave circuits, a high temperature superconductor (HTS) patch satisfies such requirements in its unloaded Q .

In high Q circuits, say $Q \geq 100$, one in fact requires analysis that is accurate to less than 1% error. For most arbitrarily shaped patches, such accuracy is normally not attainable by the numerical methods such as moment methods [29, 32] because of segmentation and truncation error. On the other hand, to have more accurate results these numerical methods are time consuming. Such high accuracy is attainable by modal method, for canonical patch shapes, or two-dimension (2D) planar circuit method (Okoshi's method), for arbitrary shapes [12]. These latter methods are fast; however, a magnetic wall is considered around the circuit and the fringing field is also ignored.

Other 2D methods, i.e. multiport network methods, explained in last chapter, are not accurate enough for analyzing a high Q circuit. Not only the fringing field is not included in those methods, but the interface between two segments is approximated by a limited number of ports which reduces the accuracy of analysis.

In this research, for high Q circuits, we make use the advantages of both types of methods. That is: 2D (modal or contour integral) method to have fast and relatively accurate results, and then numerical method using three-dimension (3D) Green's function to remove the magnetic wall and include the fringing field for more accurate results. In the second step, the formulation of the numerical method is modified to have a fast procedure.

3.2 Our Proposed Method

Our method is based on a 2D method, modal or contour integral. First, using a 2D method the parameters of the circuit, Z -matrix, are calculated very fast. Then, we will remove the magnetic wall around the patch to include fringe fields and have an accurate result. The later formulation is done through a variational method to reduce the error.

3.2.1 The Cavity with Magnetic Wall - 2D formulation

Figure 3.1 shows the structure of a microstrip patch resonator. When a canonical patch is considered, the 2D modal method can be used to analyze the structure. Let us consider the element of Z -matrix of the structure calculated by a 2D method as Z_{ij}^{2D} which are used in the next section.

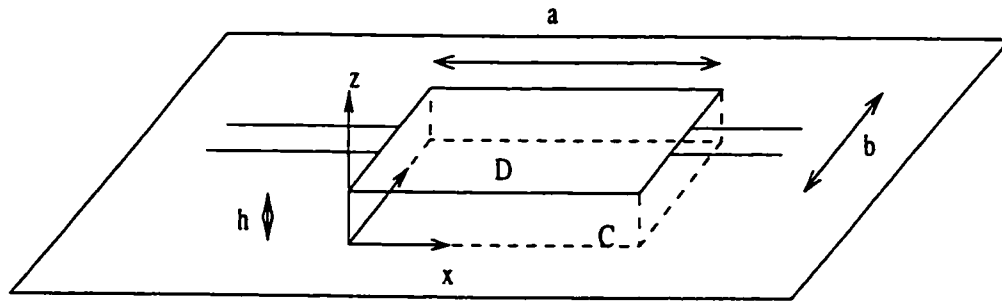


Figure 3.1: The structure of patch filter.

3.2.2 The Cavity with Magnetic Wall - 3D formulation

For the same cavity with magnetic wall, the same results as in the 2D method can be obtained using 3D Green's functions for the electric and magnetic currents.

The electric current \vec{J} and magnetic currents \vec{M} on the 3D cavity with magnetic walls are given as:

$$\vec{J} = \hat{n} \times \vec{H} \quad (3.1)$$

$$\vec{M} = \vec{E} \times \hat{n} \quad (3.2)$$

where \vec{H} and \vec{E} are the modal magnetic and electric fields, respectively. Therefore \vec{J} and \vec{M} are modal currents. The total tangential electric field on the metallic patch from 3D Green's functions is given by,

$$\vec{E}_{ti} = \vec{E}_t(\vec{J}_i) + \vec{E}_t(\vec{M}_i) \quad (3.3)$$

This tangential electric field is zero on the patch except at the feed points. The input impedance of the cavity with the magnetic wall can be calculated by a variational formula [38] as

$$Z_{ij}^{2D} = \frac{1}{I_i I_j} \int_{Patch} \vec{E}_{ti} \cdot \vec{J}_j ds + \frac{1}{I_i I_j} \int_{Edge} \vec{H}_{ti} \cdot \vec{M}_j ds \quad (3.4)$$

Since $\vec{H}_t = 0$ on the magnetic wall, the (3.4) reduces to

$$Z_{ij}^{2D} = \frac{1}{I_i I_j} \int \vec{E}_t \cdot \vec{J}_j ds \quad (3.5)$$

where I_i and I_j are currents at port i and j , respectively. Substituting (3.3) in (3.5), yields

$$Z_{ij}^{2D} = \frac{1}{I_i I_j} \int_{Patch} [\vec{E}_t(\vec{J}_i) + \vec{E}_t(\vec{M}_i)] \cdot \vec{J}_j ds \quad (3.6)$$

or

$$Z_{ij}^{2D} = \frac{1}{I_i I_j} \int_{Patch} \vec{E}_t(\vec{J}_i) \cdot \vec{J}_j ds + \frac{1}{I_i I_j} \int \vec{E}_t(\vec{M}_i) \cdot \vec{J}_j ds \quad (3.7)$$

As a reminder, it should be mentioned that the left hand side of the above equation Z_{ij}^{2D} is calculated by 2D method, and on the right hand side electric fields are calculated using 3D Green's functions.

3.2.3 The Patch - Cavity without Magnetic Wall

The real patch structure is a 3D one with fringe field at the edges, and there is only electric current \vec{J}' on the patch. The element of the Z matrix of the patch, similar to (3.5), is

$$Z_{ij} = \frac{1}{I'_i I'_j} \int_{Patch} \vec{E}_t(\vec{J}'_i) \cdot \vec{J}'_j ds \quad (3.8)$$

where I'_i and I'_j are the input currents. Equation (3.8) is also variational. Let us assume J'_i and J'_j are the *exact* solution for the patch; however, we do not have the exact solution. By replacing \vec{J}' with \vec{J} , the modal currents of the 3D cavity with magnetic wall, we have a good variational approximation of element of Z matrix, Z_{ij} in (3.8). Therefore, we have,

$$Z_{ij} = \frac{1}{I_i I_j} \int_{Patch} \vec{E}_t(\vec{J}_i) \cdot \vec{J}_j ds \quad (3.9)$$

Using (3.9) in (3.7) results

$$Z_{ij}^{2D} = Z_{ij} + \frac{1}{I_i I_j} \int_{Patch} \vec{E}_t(\vec{M}_i) \cdot \vec{J}_j ds \quad (3.10)$$

and reordering the above equation results,

$$Z_{ij} = Z_{ij}^{2D} - \frac{1}{I_i I_j} \int_{Patch} \vec{E}_t(\vec{M}_i) \cdot \vec{J}_j ds \quad (3.11)$$

The above expression shows that Z-parameter of a patch can be calculated using the 2D modal method, and then corrected by removing the effect of magnetic current to include the fringe field.

In Equation (3.11) The tangential electric field due to the magnetic current, $\vec{E}_t(\vec{M}_i)$, vanishes rapidly when we go far from the edges. This means that we need to calculate the integration in (3.11) only on the patch surface close to the edges. This property increases the speed of computations compared to the regular 3D moment method. In the regular moment method, the integration for the matrix coefficient (2.53) is carried over the entire area of the patch.

Although the integration on the patch in the second term of (3.11) is relatively fast, it can be simplified further. Using reciprocity theorem between the patch and the edge, we can change the last term in Equation (3.11), the integral, as,

$$Z_{ij} = Z_{ij}^{2D} + \frac{1}{I_i I_j} \int_{Edge} \vec{H}_t(\vec{J}_j) \cdot \vec{M}_i ds \quad (3.12)$$

On the other hand, on the magnetic wall we have,

$$\vec{H}_t = \vec{H}_t(\vec{J}_j) + \vec{H}_t(\vec{M}_j) = 0 \quad (3.13)$$

Using (3.13) in (3.12) yields,

$$Z_{ij} = Z_{ij}^{2D} - \frac{1}{I_i I_j} \int_{Edge} \vec{H}_t(\vec{M}_j) \cdot \vec{M}_i ds \quad (3.14)$$

which integrates not on the patch, but only along a line at the edge. So far in the above procedure we considered a canonical patch, so we could use 2D modal method. However, we can use 2D contour integral method for an arbitrary patch. In this case, the magnetic current \vec{M} in Equation (3.14) is not the modal current. Solving the patch with PMC using 2D contour integral method, we find the magnetic current on the edge, Equation (2.42), as well Z_{ij}^{2D} . Therefore, we are able to calculate both terms in (3.14).

In Equation (3.14), Z_{ij}^{2D} is the *exact* impedance of the patch with magnetic wall (lossless cavity) and can be calculated very fast for canonical patches by modal method or contour integral Okoshi's method for arbitrary patches [12]. The second term in Equation (3.14) is the correction with the *magnetic wall deleted*. The solution Z_{ij} in (3.14) is highly accurate because of: i) the variational principle of (3.8), ii) since most of the error is in the correction term and this is a small perturbation, one can actually afford a large relative error and still be accurate in the absolute value.

With the reduction from (3.11) to (3.14) and that Z_{ij}^{2D} is calculated very fast (2D contour integral method for arbitrary patches, and analytical solution for canonical

patches), the double surface integral is reduced to two line integrals over the strip of magnetic current.

Regular integral equation - moment method [8, 14] uses Equation (3.8) which is a double integral over the patch. If we want to have more accurate results in moment method, it will be very time consuming, because of huge number of segments. The accuracy of the results are around a few percent, say 5%, and cannot be much improved because of numerical and truncation error.

To calculate $H_t(M)$ in (3.14), we used a Green's function calculated by simulated images method [39]. Simulated images is a very fast and simple method to calculate Green's functions in multilayer structures. The details of simulated images method is given in Chapter 6.

3.3 Numerical Results

In this section, we present some numerical results to compare our method with present methods. In this work, we use three methods to analyze the structure. They are;

- 2D analysis, modal analysis for canonical shape patches or contour integral (Okoshi's) method for arbitrary shape patches
- Method of Moment (MoM) as a regular numerical method
- Our new hybrid method.

Since, we believe our method is accurate, the results of our method should be compared with experimental results. In experiment, there are tolerances in

dielectric constant and dimensions of a circuit. Therefore, the experimental results may change from sample to sample. However, to verify our method, we need a reliable result. Here, the results of our method are compared with the results of a software called Sonnet, as a bench mark.

This software is very accurate in analyzing high Q circuits. However, the segmentation of the circuit (grid) should be fit to the circuit. The accuracy of Sonnet is good, however, it is very slow. In this work, the Sonnet results are provided by ComDev.

Sonnet considers the structure in a box. However, in our simulation, we use the Green's function of a multilayer structure. To compare our results with Sonnet results, we consider a metallic plate as top cover and delete the real part of Z-parameters to delete the radiation from the structure.

In this chapter, different examples are presented to verify our method. First, we start with a one port patch antenna, and calculate the input impedance of the antenna. Then some canonical shape patches, such as rectangular and circular shapes, are analyzed. As an arbitrary shape filter, a dual mode filter is analyzed. The last example, as a multiport network, a 3-way power divider is analyzed.

3.3.1 One Port Circuit, Patch Antenna

The modal or contour integral methods are widely used in microwave circuits because of their simplicity and high speed. However, for a patch antenna, a one port patch, 2D methods are not applicable to find the input impedance. However, Lo *et al* [40] used the results of 2D modal method, the magnetic current at the edge of a patch, and calculated the far field pattern of the antenna using the 3D Green's function. Other methods such as moment method or finite-difference time-domain

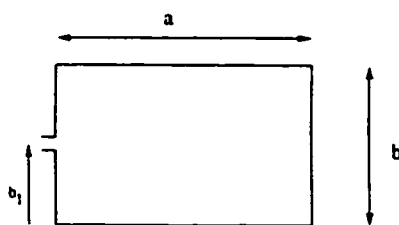


Figure 3.2: The rectangular patch antenna.

method [16] are the common methods for analyzing patch antenna.

Since our method considers the fringe field and radiation, the input impedance of a patch antenna can be calculated by our method. A rectangular patch antenna is shown in Figure 3.2. The dimensions of the patch are $a = 16 \text{ mm}$, $b = 12.45 \text{ mm}$, and the position of line feed is $b_1 = 2.09 \text{ mm}$, and the dielectric constant is $\epsilon_r = 2.2$, with substrate thickness of $h = 0.794 \text{ mm}$, and the width of feed line is $w = 2.46 \text{ mm}$.

The S_{11} of the antenna is given in Figure 3.3. The experimental results from [41] and moment method results are also shown in this figure. As we can see, our method is more accurate in predicting the resonant frequency than moment method. The difference between resonant frequencies from our method and the experiment is about 0.7%. However, for moment method the difference is about 2.5%.

The speed of our analysis is very high, and for this example our method spends about 6 sec. for each frequency. Moment method spends more than 70 sec. for each frequency on the same machine which is a HP-Unix machine (series 735). This shows that our method is more than 11 times faster than moment method.

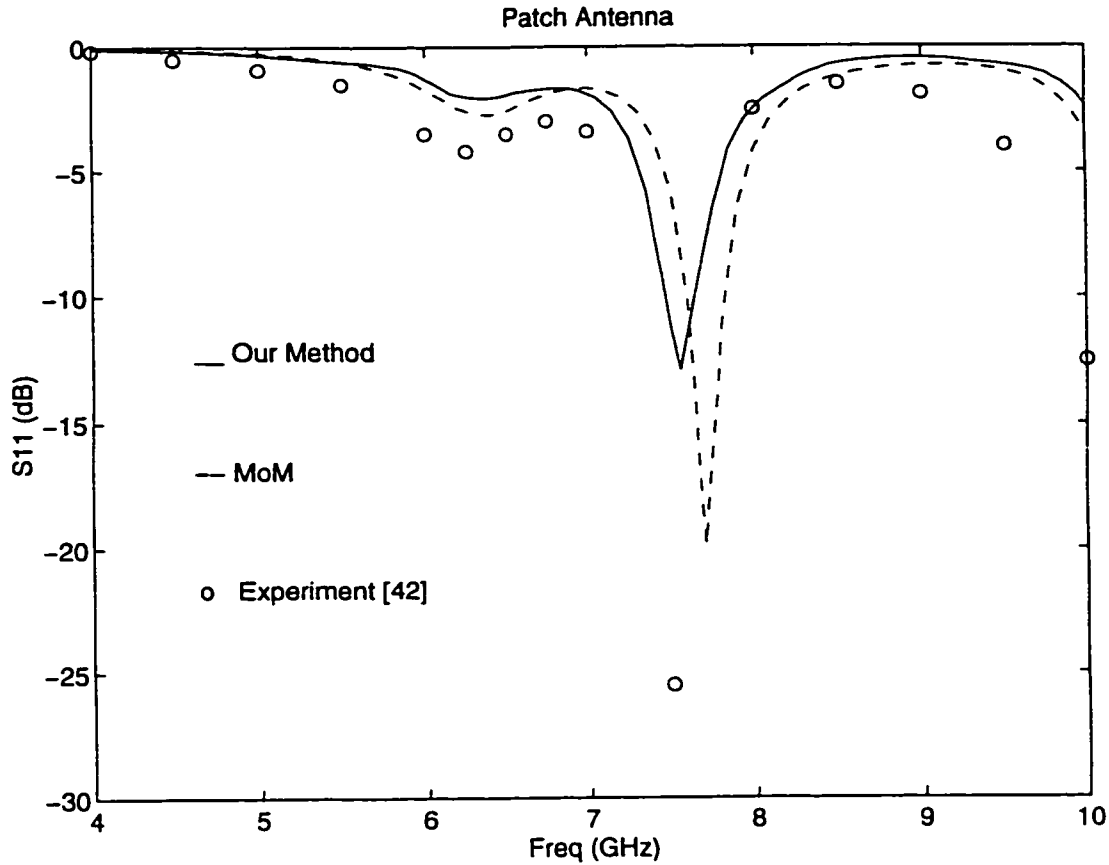


Figure 3.3: Return loss of the rectangular antenna.

3.3.2 2 Port Canonical Shape Filters

Rectangular Patch

A rectangular patch with 2 port direct feed is shown in Figure 3.4. For a rectangular patch, the Z-matrix can be calculated analytically by 2D modal analysis. The details are given in Appendix C.

To apply our method, we need the equivalent magnetic current around the edge of the patch. This magnetic current can be derived from modal solution or from

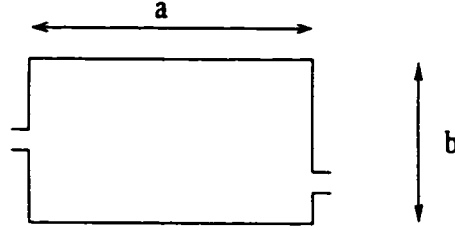


Figure 3.4: Rectangular patch filter.

2D Okoshi's contour integral solution. To find the magnetic current from modal solution, we can use waveguide theory. In TM_{mn} modes in rectangular wave guide with magnetic wall, we have

$$E_z = \cos(k_x x) \cos(k_y y) \quad (3.15)$$

where

$$k_x = \frac{m\pi}{a} \quad k_y = \frac{n\pi}{b}$$

So the magnetic current around the edge can be derived as,

$$\vec{M} = \vec{E} \times \hat{n} \quad , \quad \text{on the Edge} \quad (3.16)$$

Using the above magnetic current in Equation (3.14), we can calculate the Z-matrix of the structure. Then from Z-matrix, S-matrix can be calculated.

The dimensions of the structure shown in Figure 3.4 are $a = 16.5 \text{ mm}$, $b = 10 \text{ cm}$, and the two ports are connected to 50Ω lines, width of feed lines is $w = 0.635 \text{ mm}$. Two feed lines are located at the center of each side. The dielectric constant is $\epsilon_r = 10$ and height of the substrate is $h = 0.635 \text{ mm}$.

The numerical results of our method are compared with the Sonnet results from ComDev and moment method in Figures 3.5 and 3.6. As we can see the results of

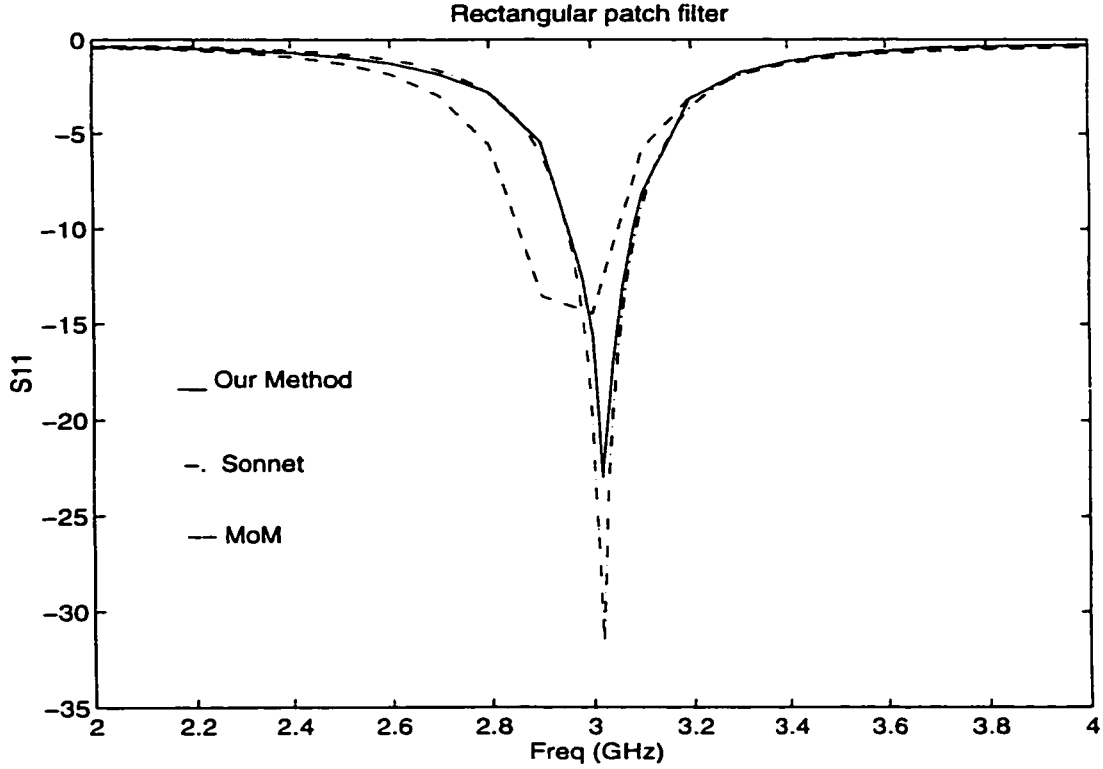


Figure 3.5: The amplitude of S_{11} for the rectangular patch filter.

our method are very accurate, and it predicts the resonant frequency as 3.07 GHz which is about 0.7% higher than the Sonnet result, 3.05 GHz .

As mentioned earlier, as an empirical method to find the resonant frequency of a regular shape patch, the 2D modal method is used with the effective dielectric constant. The effective dielectric constant can be found as [26],

$$\epsilon_e = \frac{\epsilon_r + 1}{2} + \frac{\epsilon_r - 1}{2} \left(1 + \frac{10h}{b}\right)^{-1/2} = 9.32 \quad (3.17)$$

and the resonant frequency is,

$$f_r = \frac{c}{\sqrt{\epsilon_e} 2a} = 2.98 \text{ GHz} \quad (3.18)$$

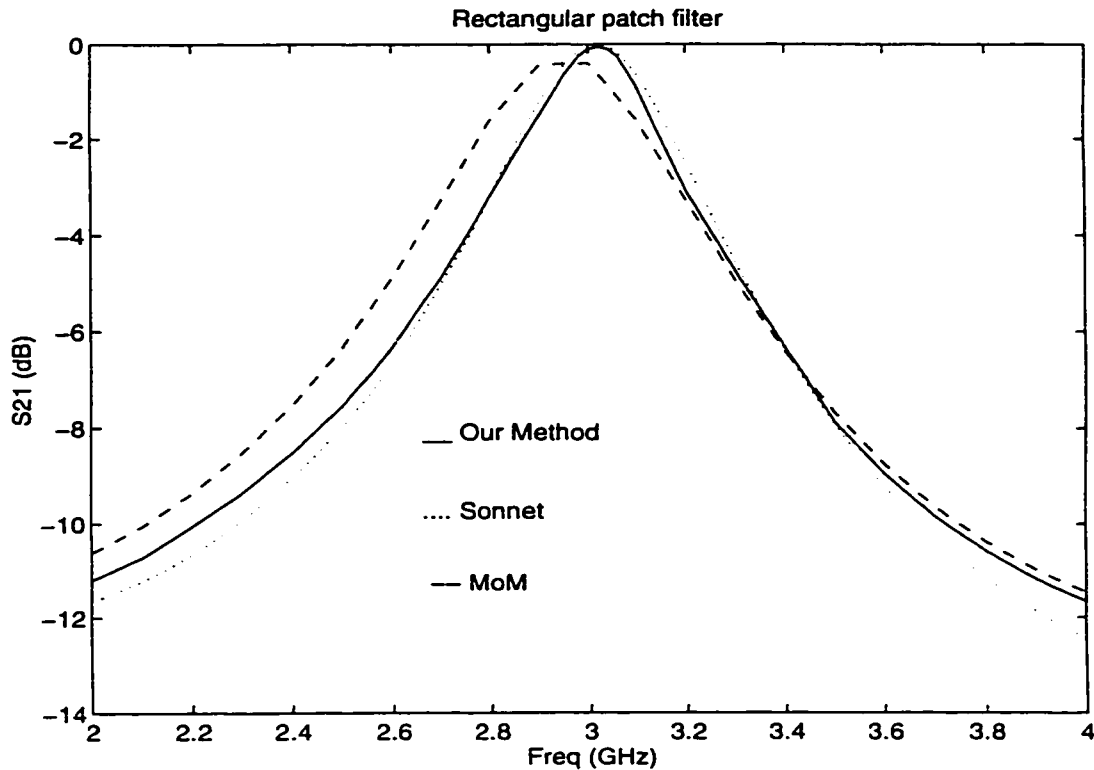


Figure 3.6: The amplitude of S_{21} for the rectangular patch filter.

which is 2.3% lower than the Sonnet result. The resonant frequency from the moment method, about 2.95 GHz, is 3.3% lower than the Sonnet result.

Similar to the first example, our method is also fast. For this example our method is more than 12 times faster than moment method.

Circular Patch

The structure of a circular patch is shown in Figure 3.7. For a circular patch, the Z-matrix can also be calculated analytically. Similar to the rectangular patch in the last section, we can calculate the magnetic current at the edge of the patch based on the electric field under the patch as,

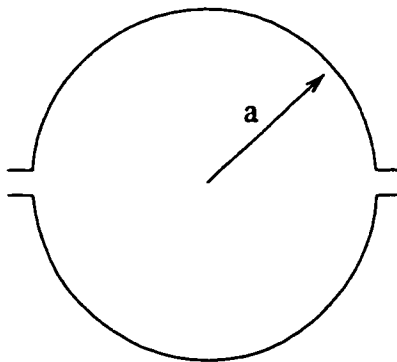


Figure 3.7: Circular patch filter.

$$\vec{E} = J_n(k_n \rho) \cos(n\phi) \hat{z} \quad (3.19)$$

$$\vec{M} = \vec{E} \times \hat{\rho} = J_n(k_n \rho) \cos(n\phi) \hat{\phi} \quad (3.20)$$

where J_n is the Bessel function of first kind order n , and $k_n = 1.84/a$ for $n = 1$, where a is the radius of the circular patch. Using the above current in our method in Equation (3.14), we can easily calculate the Z-matrix of the circular patch.

For this structure, the radius of the circle is $a = 5 \text{ mm}$, the dielectric constant is $\epsilon_r = 10$, and height of substrate is $h = 0.635 \text{ mm}$, and the width of feed lines is $w = 0.635 \text{ mm}$. The results of our method and regular moment method and Sonnet from ComDev, S_{11} and S_{21} , are shown in Figures 3.8 and 3.9. As we can see our result is very accurate, especially in predicting the resonant frequency. The error in resonant frequency in our method and moment method, in comparison with Sonnet, are 0.9% and 1.7%, respectively. This shows the higher accuracy of our method in comparison with moment method, because of the edge of the circuit. At the edge of circular patch, there is a truncation error in moment method. This

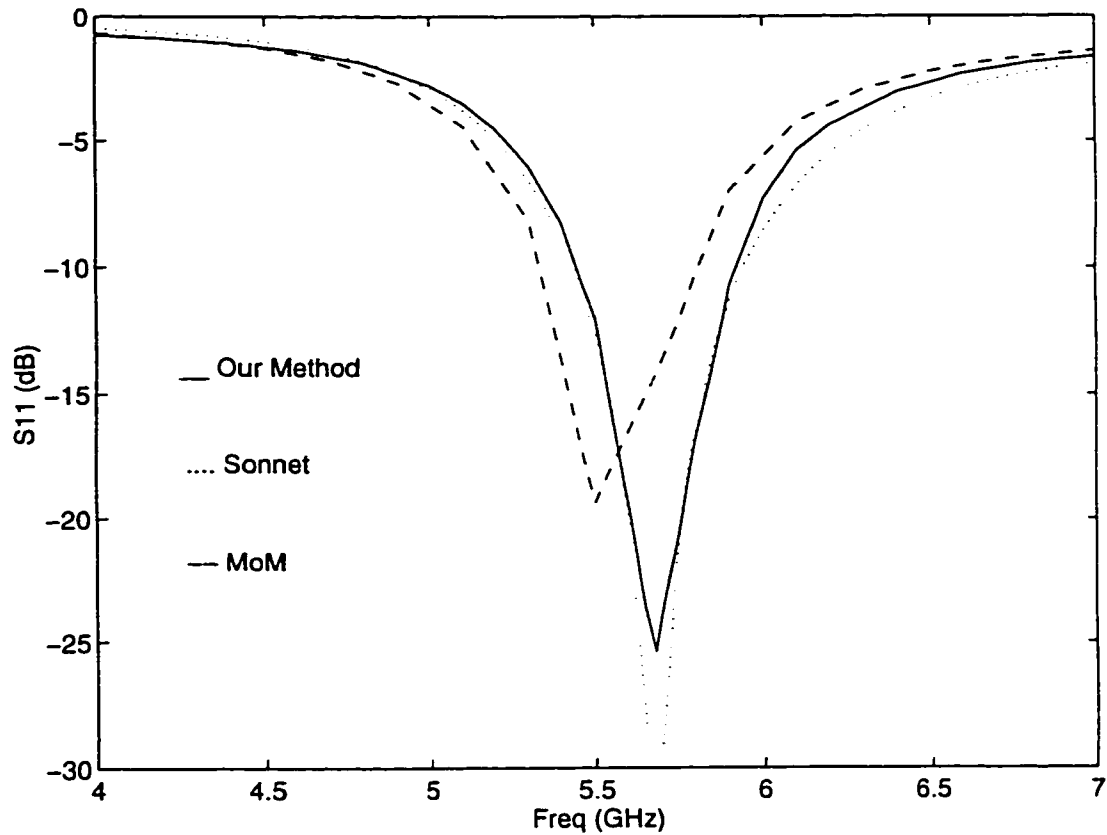


Figure 3.8: The amplitude of S_{11} for the circular patch

example can be solved by moment method using fine segmentation or more complex segmentation. However, this makes the moment method very time consuming.

In terms of speed, for this example our method is much faster than moment method. Our method spends 6 sec. for each frequency, and moment method spends about 75 sec on HP-Unix machine (series 735). This shows that our method is more than 12 times faster than moment method.

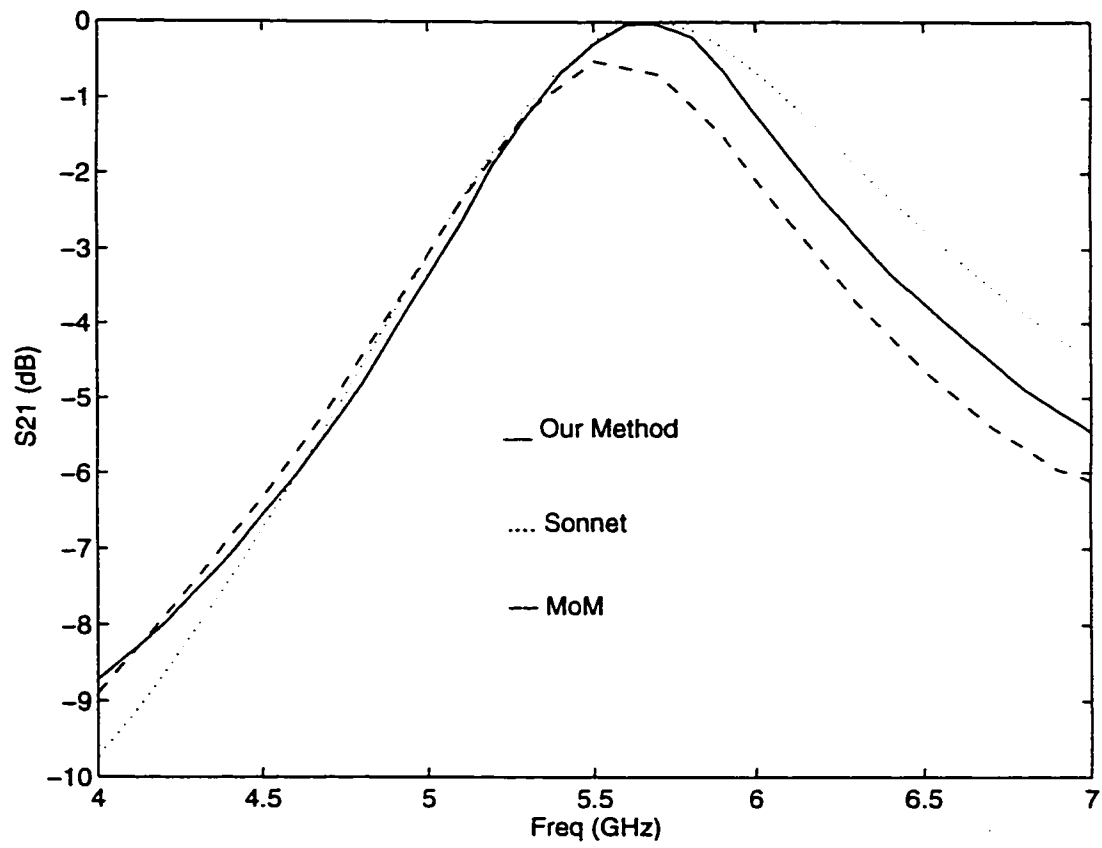


Figure 3.9: The amplitude of S_{21} for the circular patch

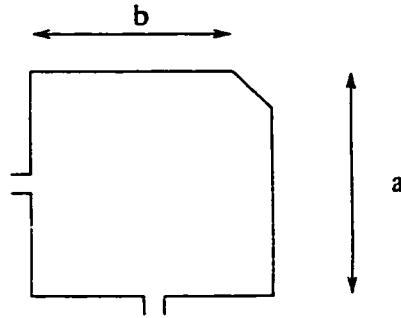


Figure 3.10: Dual mode patch filter.

3.3.3 Dual Mode Filters

The structure of a dual mode filter is shown in Figure 3.10. Since this structure does not have a canonical shape, the 2D modal solution cannot be used, and we have to use other 2D methods such as contour integral method or desegmentation method. To analyze this structure with our method, we start with 2D contour integral method, and the magnetic wall is then removed using the method explain in Section 3.1.

The general shape of a dual mode filter is a square patch with corner cut, shown in Figure 3.10. In this example the corner cut is symmetric, $a = 7.419 \text{ mm}$ and $b = 6.426 \text{ mm}$. The dielectric height is $h = 0.508 \text{ mm}$, and $\epsilon_r = 24$. The width of feed lines is $w = 0.175 \text{ mm}$. This structure has been analyzed by 2D contour integral method, our method and Sonnet from ComDev, and results, S_{11} and S_{21} are shown in Figures 3.11 and 3.12. There is a good agreement between our results and Sonnet results. The contour integral method result has a frequency shift, because the fringe field is not considered in the analysis.

From the result of this example, we can easily say that our analysis is very accurate. There is a very good agreement between our result and Sonnet result.

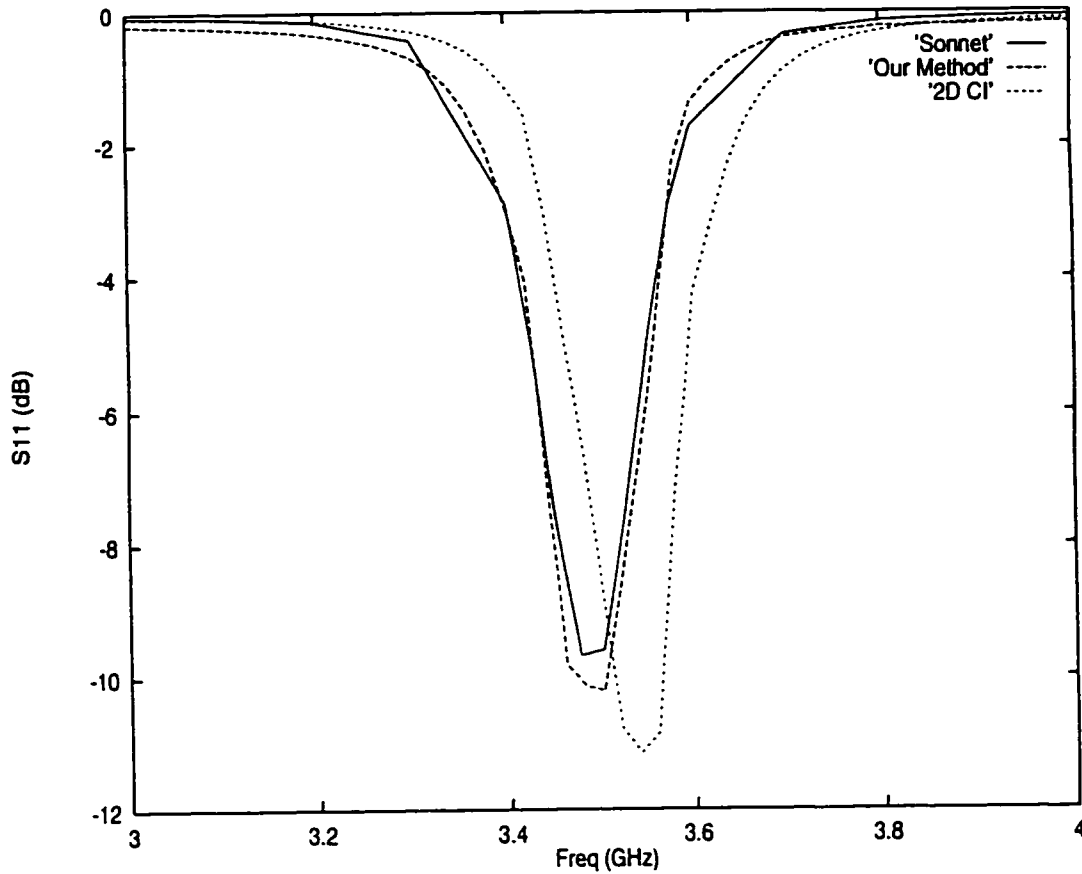


Figure 3.11: The amplitude of S_{11} for the dual mode filter.

The error between 2D contour integral and ours (or Sonnet) is about 1.4%. As mentioned earlier, since the circuit is in the box for Sonnet simulation, we delete the real part of Z-matrix to delete the radiation from the circuit. As with other examples, in this case our method is very fast.

This dual mode structure has been used in higher order filters, such as a Chebyshev filter, which will be analyzed in Chapter 5. The analysis of one patch element was given in this chapter, and in Chapter 5, coupling between patch elements are investigated.

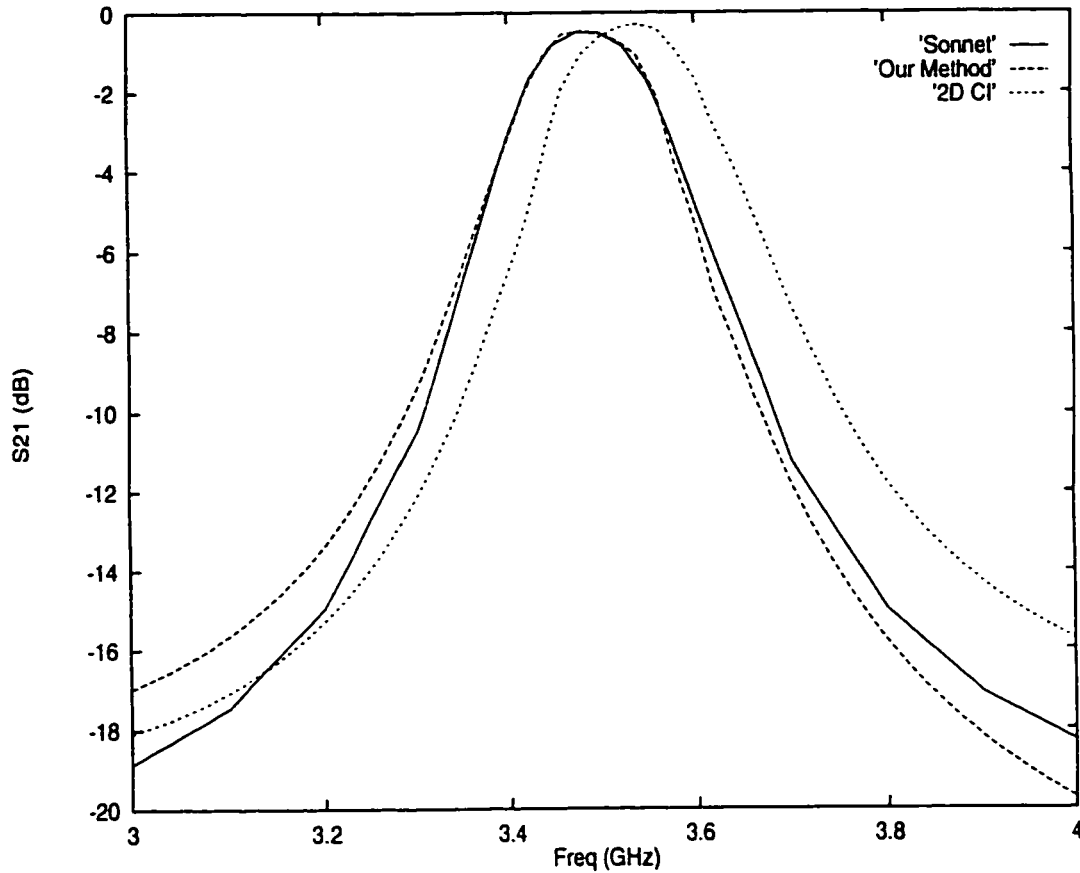


Figure 3.12: The amplitude of S_{21} for the dual mode filter.

3.3.4 Multiport circuits, Power divider

The last example of this section, a 3-way power divider, is analyzed as an example of a multiport network. The microstrip sectorial 3-way power divider is shown in Figure 3.13.

This structure has already been analyzed by Abouzahra and Gupta [42] based on 2D modal method (Green's function is represented as an expansion of eigenfunctions). However, their model is valid only if the sector angle α takes on certain discrete values which is π/m where m is an integer. The more general analysis was

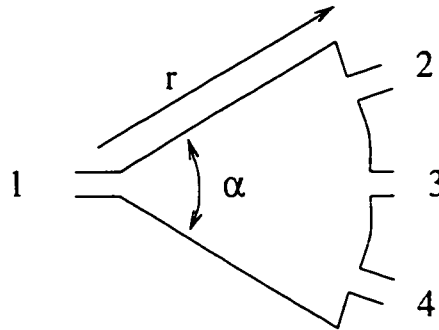


Figure 3.13: Power divider

done using contour integral method for any arbitrary value of α [43]. In both cases a fringe field was not considered, because a 2D model was used.

To consider the fringe field and radiation loss, we use our method which is the 2D contour integral method and the correction term, 3D line integral, which removes the magnetic wall considered in the 2D method [44].

The parameters of the structure are as follows: $r = 32 \text{ mm}$, $\alpha = 50^\circ$, $\epsilon_r = 2.2$ and $h = 0.79 \text{ mm}$. The responses of the power divider, S_{11} and S_{21} , are shown in Figures 3.14 and 3.15. The experimental results from [43] are also shown in those graphs. The error of our analysis is less than the error in 2D contour integral results. The error of our analysis is about 0.6 % in comparison with the experimental results. Other transmission responses, S_{31} and S_{41} , are also calculated, and they are very close to S_{21} , however, they are not shown here.

As we saw, in all examples, the proposed method gives more accurate results than other methods. This method is also much faster than regular numerical methods.

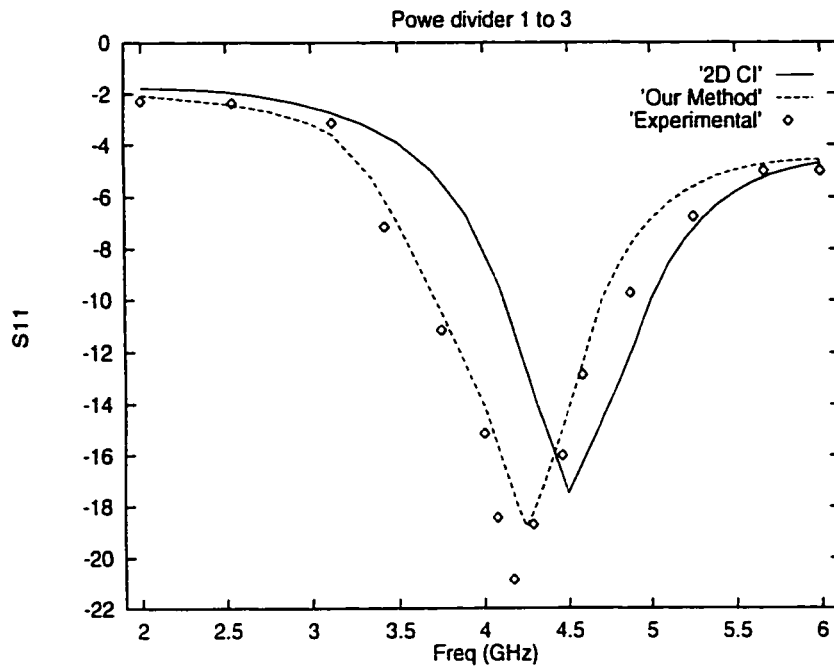


Figure 3.14: The amplitude of S_{11} for the power divider

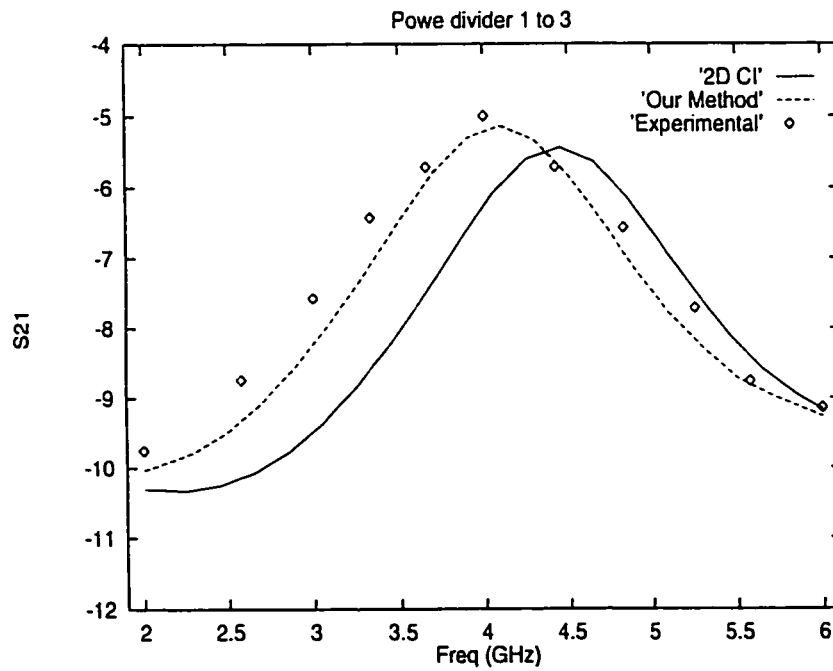


Figure 3.15: The amplitude of S_{21} for the power divider

Chapter 4

Gap Coupling

4.1 Introduction

Microstrip filters may have high unloaded Q . To ensure that the loaded Q remains high, instead of direct connections, couplings by a narrow gap are frequently used to link the patch to other parts of the circuit. Because of the high Q , high accuracies are required to model both the patch itself and the gap coupling without sacrificing the speed of computation. In the previous chapter, a new hybrid method was presented for accurate analysis of a patch. In this chapter, an accurate method for a narrow gap, a novel transmission line model, is presented.

A general structure of gap coupling is shown in Figure 4.1. The equivalent circuit (π -model, which consists of three capacitors) of this gap was given in literature for various microstrip-microstrip coupling [45, 46]. However, for planar circuit-microstrip coupling no detailed data are available. The electrostatic field analysis would become three dimensional and very difficult to perform. There are some typical and experimental data are available in the literature [47]. Therefore, almost



Figure 4.1: Ordinary structure of a gap coupling

in all cases the model of microstrip-microstrip coupling is used. To have a more accurate analysis, one can apply the regular moment method for the patch filter with gap structure.

In conventional gap coupling, Figure 4.1, the coupling between the patch and feed network is very weak. To increase the coupling, the feed line should be put very close to the patch. Because of manufacturing limitation, the line cannot be put very close to patch. Therefore, a new gap structure was introduced in [48] as shown in Figure 4.2a.

In this chapter, the gap structure shown in Figure 4.2a is modeled. This gap is frequently quite narrow and is formed between a narrow microstrip and the patch. To adequately consider the rapid field changes around the narrow gap and strip, the segments in a moment method analysis have to be quite small. This makes the number of segments in the structure impractically large. On the other hand the accuracy of the moment method could be reduced because of very small segments (small segmentation makes the coefficient matrix ill condition).

In this chapter a new method is presented [49, 50] to overcome such difficulty so that the number of segments remains small and the accuracy remains high. To verify the accuracy of the gap model, the result of our simulation is compared with results from ComDev.

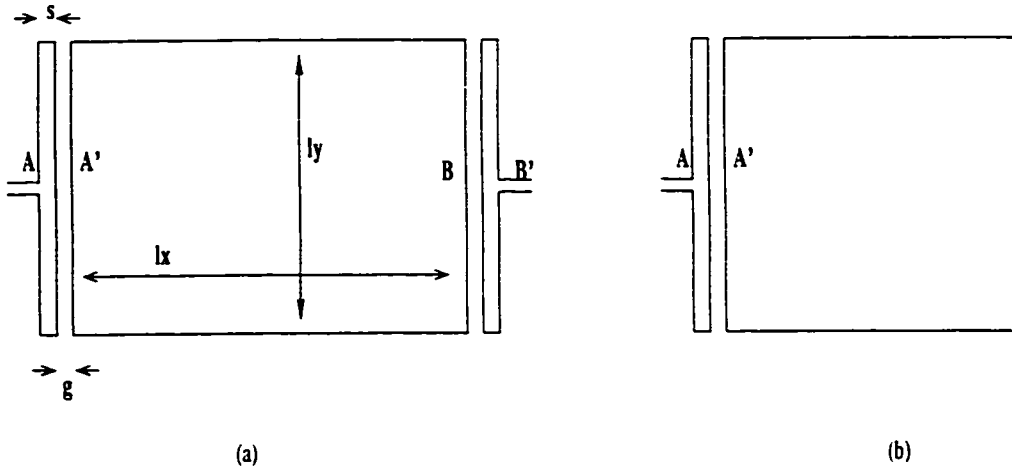


Figure 4.2: General structure of a filter with gap coupling

4.2 Modeling of the Gap

The general of a gap coupling is shown in Figure 4.2a. In this structure, the gap at A is formed between the narrow microstrip and the patch. Let us assume the width of strip and gap as s and g respectively, and dimensions of the patch as l_x and l_y as shown in Figure 4.2a. As an approximation if $s, g \ll l_x, l_y$, which is valid in most practical cases, the narrow strip and patch can be considered as a transmission line. This transmission line consists of a strip and a half plane on top of a dielectric. The narrow microstrip and the patch in fact form two transmission line stubs, one on each side of the feed point A' of the input port. Each stub is shorter than $\lambda/4$ so that their impedances are capacitive. This means that point A' is equivalently connected to point A by two capacitors in parallel, $2C$. This equivalence is presented at the other feed point, B-B'. The task now is to find the characteristic impedance of the line, Z_o , and the propagation constant β of the transmission line. Then the impedance of the each open circuit stub (above or below A-A') is,

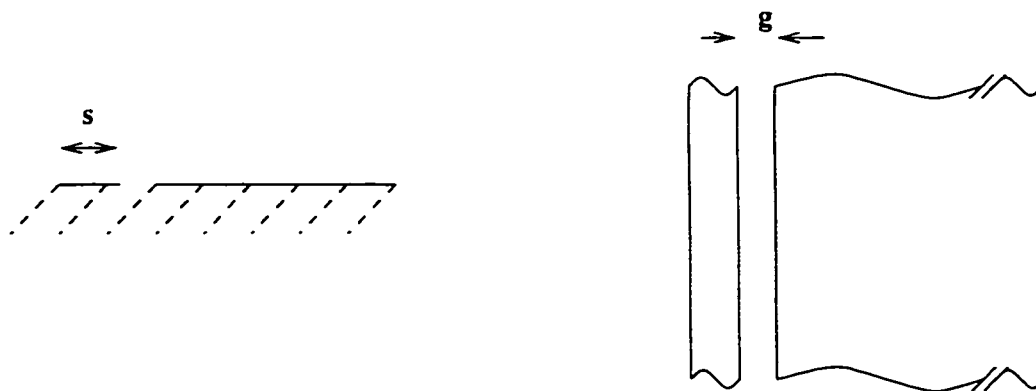


Figure 4.3: Structure of the transmission line

$$Z = -jZ_o \cot(\beta l) = \frac{1}{j\omega C} \quad (4.1)$$

The second equality in Equation (4.1) is given since l is smaller than $\lambda/4$. Since there are two stubs in parallel from A-A', the equivalent capacitance is $2C$ as shown in port B-B'.

In the next section, we present a new model to find the characteristic impedance of the transmission line, Z_o . In this analysis, the propagation constant, β , of the transmission line is also found. First, we consider a general structure for the gap, and then a symmetrical gap (when $s = g$), as a special case, is also analyzed with a simpler method and verified by the general method.

4.2.1 Parameters of the Transmission Line

As an approximation, the gap and the microstrip width are considered much narrower than the dielectric substrate ($g, s \ll h$), this is valid in most practical cases. As a results, the ground plane below the substrate may be neglected or, better, dragged to minus infinity $h \rightarrow -\infty$. Now, as shown in Figure 4.3, the transmission

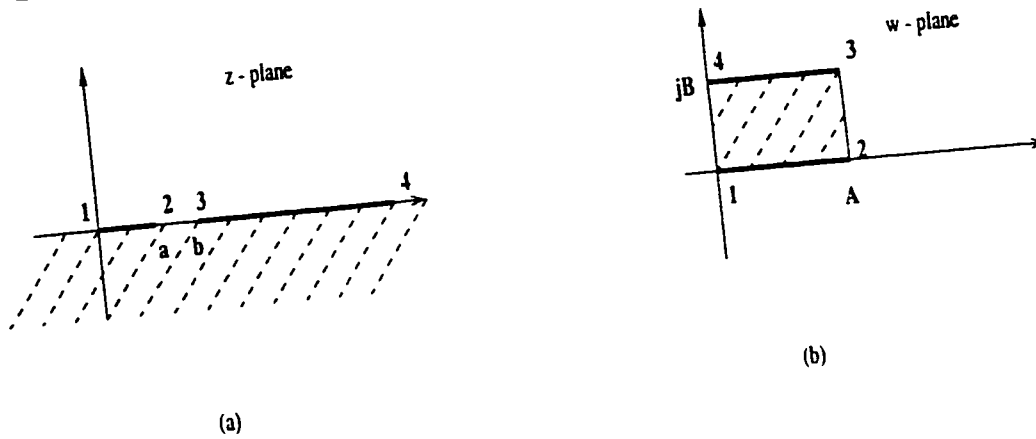


Figure 4.4: Conformal mapping z & w plane

line can be considered as a strip next to a conductive half plane sitting on a half space of dielectric. To find the characteristic impedance of this transmission line, we can start with the capacitance of the line, and then find characteristic impedance of the line.

To find the capacitance of the line, we use the conformal mapping. For simplicity, let us make our notation simpler as $a = s$ and $b = s + g$ which is shown in Figure 4.4a. Using Schwartz-Christofer method [51], z -plane will be transformed to w -plane, Figure 4.4b, by the following transformation:

$$w = \int_0^z \frac{dt}{\sqrt{t(t-a)(t-b)}} \tag{4.2}$$

Notice that in this transformation origin is fixed, i.e. $z = 0 \rightarrow w = 0$. As shown in Figure 4.4, with the above transformation, the lower half space of z -plane is mapped to the inside region of the rectangle in w -plane. To calculate the above integral, (4.2), we simplify it as,

$$w = \int_0^{z/a} \frac{dt}{\sqrt{b}\sqrt{t(1-k^2t)(1-t)}} \quad (4.3)$$

where

$$k^2 = \frac{a}{b} \quad (4.4)$$

Integral in (4.3) is in the form of Elliptic integral of the first kind. Elliptic integral of the first kind is defined as [52],

$$F(k, \phi) = \frac{1}{2} \int_0^{\sin \phi} \frac{dt}{\sqrt{t(1-k^2t)(1-t)}} \quad (4.5)$$

Therefore (4.3) can be written as

$$w = \frac{2}{\sqrt{b}} F(k, \phi) \quad (4.6)$$

where

$$\phi = \arcsin\left(\frac{z}{a}\right) \quad (4.7)$$

Using the rectangle in w -plane, Figure 4.4, the capacitance of the lower half space (C_l) of the transmission line (in z -plane) can be found as,

$$C_l = \epsilon_o \epsilon_r \frac{A}{B} \quad (4.8)$$

The length A is transformed from the distance between points 1 and 2 in z -plane.

Hence, we have

$$A = \int_0^a \frac{dt}{\sqrt{t(1-k^2t)(1-t)}} = \frac{2}{\sqrt{b}} F(k, \pi/2) = \frac{2}{\sqrt{b}} K(k) \quad (4.9)$$

where $K(k)$ is the complete elliptic integral of the first kind. The length B is transformed from the distance between points 1 and 4 in z -plane. So, we have

$$jB = \int_0^\infty \frac{dt}{\sqrt{t(1-k^2t)(1-t)}} = \frac{2j}{\sqrt{b}} F(k, \infty) = \frac{2j}{\sqrt{b}} K'(k) \quad (4.10)$$

where $K'(k)$ is complete elliptic integral of the second kind. Finally, using (4.9) and (4.10) in (4.8) the capacitance will be,

$$C_l = \epsilon_o \epsilon_r \frac{K(k)}{K'(k)} \quad (4.11)$$

The capacitance of the upper half space of the transmission line can be found using Equation (4.11) and setting $\epsilon_r = 1$,

$$C_u = \epsilon_o \frac{K(k)}{K'(k)} \quad (4.12)$$

Therefore, the total capacitance of the line is,

$$C = \epsilon_o (1 + \epsilon_r) \frac{K(k)}{K'(k)} \quad (4.13)$$

To find the effective dielectric constant ϵ_{eff} , we first set the $\epsilon_r = 1$ and find the capacitance of the structure with the air, C_{air} . Then, ϵ_{eff} is found as follows,

$$\epsilon_{eff} = \frac{C}{C_{air}} = \frac{1 + \epsilon_r}{2} \quad (4.14)$$

Therefore (4.13) can be written as,

$$C = 2\epsilon_o \epsilon_{eff} \frac{K(k)}{K'(k)} \quad (4.15)$$

An accurate but simple expression of the ratio K/K' is available in the handbooks [53] and is included here,

$$\frac{K(k)}{K'(k)} = \begin{cases} \pi / \ln[2(1 + \sqrt{k'}) / (1 - \sqrt{k'})] & 0 \leq k \leq 0.707 \\ \ln[2(1 + \sqrt{k}) / (1 - \sqrt{k})] / \pi & 0.707 \leq k \leq 1 \end{cases} \quad (4.16)$$

where $k' = \sqrt{1 - k^2}$. As a reminder, we defined $k = \sqrt{a/b} = \sqrt{s/(s + g)}$. After finding C in (4.13), we can easily find the characteristic impedance of the line.

For any Quasi-TEM transmission line, the phase velocity and the characteristic impedance can be written as,

$$v_p = \frac{1}{\sqrt{LC}} = \frac{1}{\sqrt{\mu\epsilon}} \quad (4.17)$$

and

$$Z_o = \sqrt{\frac{L}{C}} \quad (4.18)$$

Where $\epsilon = \epsilon_o\epsilon_{eff}$. Using (4.17) in (4.18), we have

$$Z_o = \frac{\sqrt{\mu\epsilon}}{C} \quad (4.19)$$

Using (4.13) in (4.19), the characteristic impedance can be written as,

$$Z_o = \frac{1}{2} \sqrt{\frac{\mu}{\epsilon}} \frac{K'(k)}{K(k)} \quad (4.20)$$

The impedance of the line is plotted for three different substrates (ϵ_r) in Figure 4.5.

Using (4.14), the propagation constant of the line can be written as,

$$\beta = \omega \sqrt{\mu_o\epsilon_o\epsilon_{eff}} = \omega \sqrt{\mu_o\epsilon_o(1 + \epsilon_r)/2} \quad (4.21)$$

Now, using Z_o and β defined by (4.21) and (4.20), the impedance of the open circuit stub can be found using (4.1).

4.2.2 Symmetrical Gap

There is a special case in the gap structure, when the width of the strip is the same as width of the gap, i.e. $s = g$, and we call it a symmetric gap structure. The characteristic impedance of the transmission line in the symmetric case can be

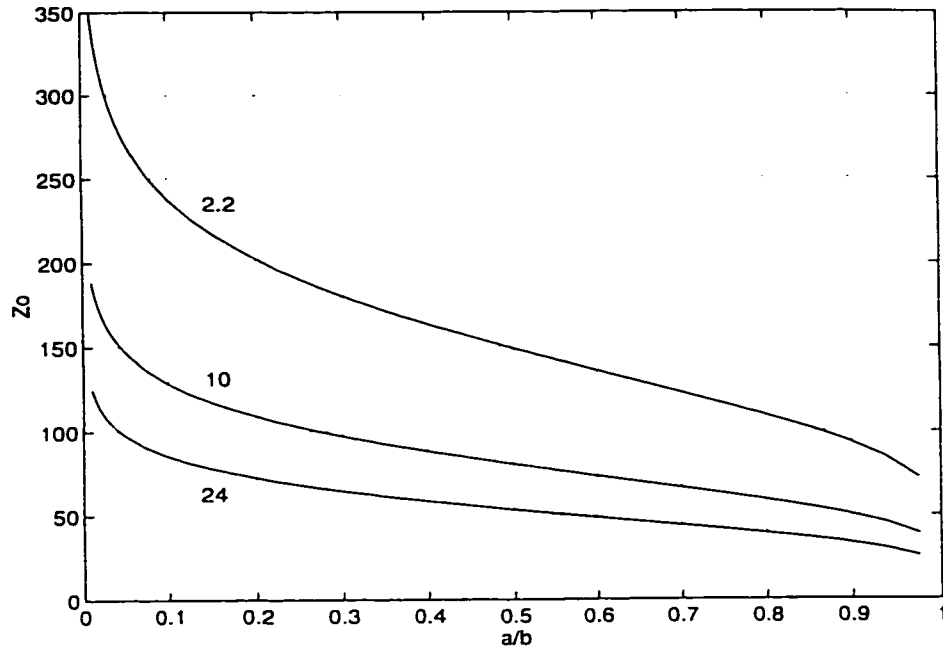


Figure 4.5: Impedance of line $Z_0(\Omega)$ for three kinds of substrate (ϵ_r)

calculated by the general Equation (4.13). However, for this special case, we can directly find the characteristic impedance of the transmission line more easily, using another method. In this section, the characteristic impedance of the transmission line is derived using a simpler method, and compare with the general method given in the last section.

As in the general case, since the strip and gap are small in terms of wavelength, the transmission line can be taken to be in a *homogeneous dielectric* with an averaged dielectric constant of,

$$\epsilon_{eff} = (1 + \epsilon_r)/2$$

Similar to the general case, the propagation constant of the transmission line can be written as

$$\beta = \omega \sqrt{\mu_0 \epsilon_0 (1 + \epsilon_r)/2} \quad (4.22)$$

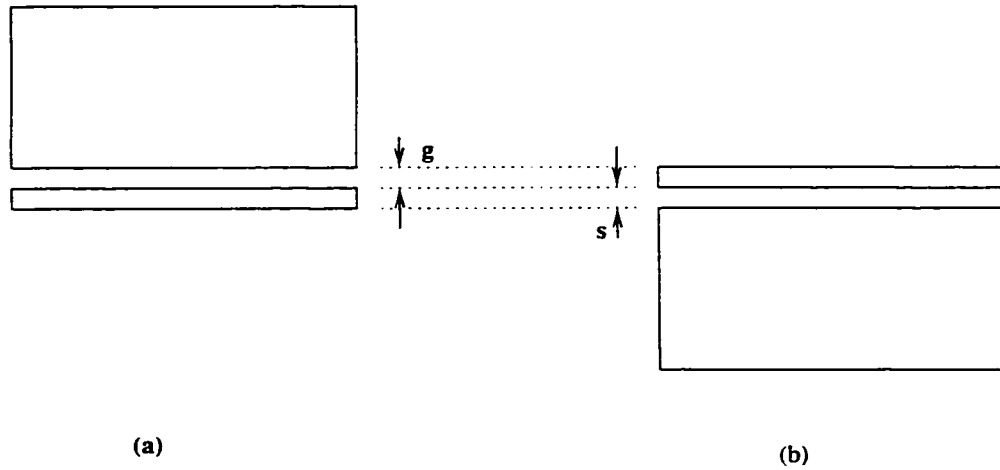


Figure 4.6: Transmission Line with its dual

The transmission line can be considered as a strip next to a conductive half plate sitting on a half space of dielectric. If we consider the dual of the transmission line, we have the same structure, because $s = g$, as shown in Figure 4.6. It means that the structure is self complementary. Through the Babinet's principle, which has also been used in complementary antenna, the relationship between the characteristic impedance of these two lines is,

$$Z_o \cdot Z_o^d = \eta^2/4 \quad (4.23)$$

where Z_o and Z_o^d are the characteristic impedance of the line and its dual. Since the structure is the same as its dual, we have $Z_o = Z_o^d$. Therefore Equation (4.23) reduces to

$$Z_o = \eta/2 \quad (4.24)$$

The result with this method in (4.24) agrees with the general solution in (4.20). Using the result of the general analysis in the last section, for a symmetric gap we

have,

$$s = g \rightarrow k = 0.707 \rightarrow C = 2\epsilon$$

and then

$$Z_o = \frac{1}{2} \sqrt{\frac{\mu}{\epsilon}} = \eta/2$$

4.3 Effect of Ground Plane and Finite Dielectric

When the gap width, g , and strip width, s , are not very small in comparison with the height of dielectric, h , we should consider the effect of ground plane and finite dielectric height. A similar investigation was done [54] for coplanar wave guide, and it was found that if $h/s > 4$, the effect of ground plane can be ignored (i.e. $h \rightarrow \infty$). For our practical example, from ComDev, $h/s > 10$, therefore we believe considering the ground plane, and finite dielectric height does not effect our results. However, it is possible to use image theory, to consider the ground plane effect, and then with a similar method, we can find the capacitance of the structure for the general case.

In this section, to include these effects a method is briefly outlined. Since we do not include this general case in our analysis, the detail of the method is not given in this section. This procedure can be added to our analysis, for accurate and general analysis, as a future work.

For the analysis of this structure, Figure 4.3, we invoke the assumption that total capacitance is the sum of the free space capacitance, the upper half-plane, and the capacitance of the dielectric space, the lower half-plane. The free space capacitance for the upper half-plane is exactly the same as before, C_u . However, to Calculate C_l , we have to consider the effect of ground plane. To include this effect,

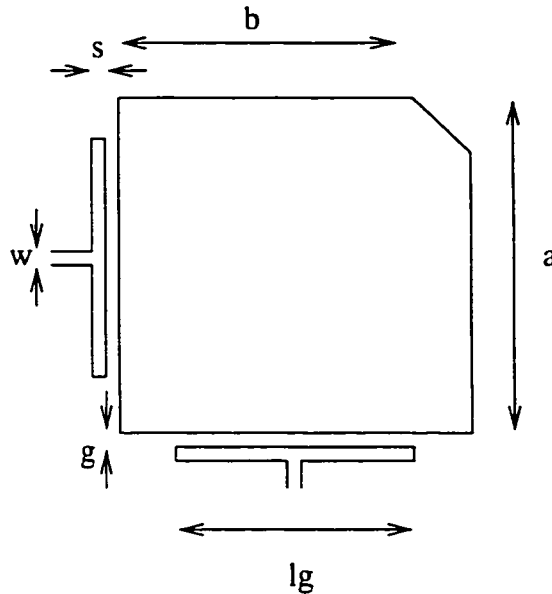


Figure 4.7: Dual mode filter with gap coupling

the quasi-dynamic images [55] can be considered. If the dielectric is high, we can choose a few images to have a fast convergent solution.

The capacitance of the line should be calculated including the images. Then, the impedance of the line is derived using (4.19).

4.4 Numerical Results

In this section, to verify the presented method for modeling of gap structure, we compare the results of our method with Sonnet results from ComDev. As mentioned before, Sonnet results provided by ComDev have been used as a bench mark in our research.

The structure of dual mode filter with gap coupling is shown in Figure 4.7. In this structure, the symmetric gap, $s = g$, is considered. The dimensions are

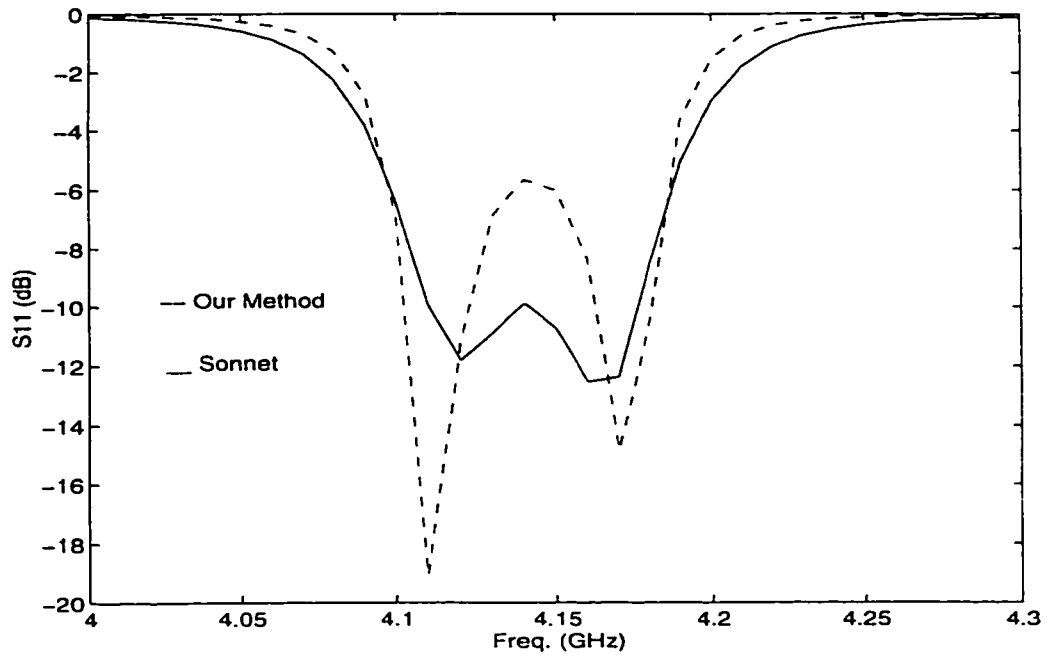


Figure 4.8: Return loss of gap coupled dual mode filter

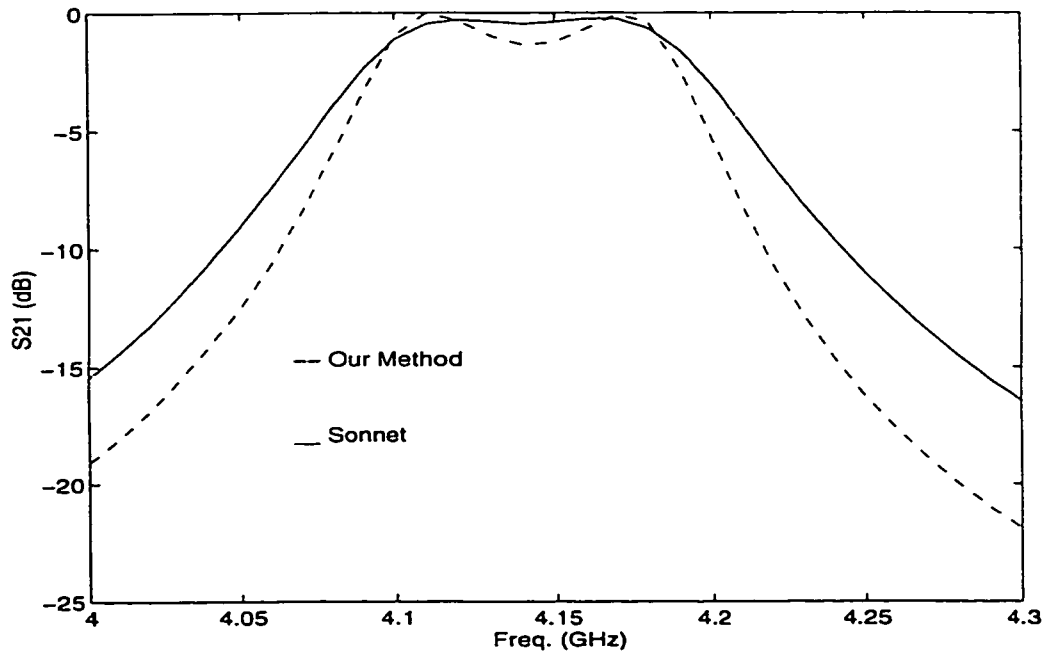


Figure 4.9: Insertion loss of gap coupled dual mode filter

as follow: $a = 7.419 \text{ mm}$, $b = 6.368 \text{ mm}$, $s = g = 58.42\mu\text{m}$, $l_g = 5.083 \text{ mm}$, $w = 0.175 \text{ mm}$. The substrate parameters are as follow: $h = 0.508 \text{ mm}$, $\epsilon_r = 24$.

It should be mentioned that Sonnet simulate the circuit is in a box. Therefore, to comare our result with Sonnet, in our simulation the real part of Z-parameter is removed to delete the radiation.

First, we analyzed the circuit without the gap using our new proposed method in Chapter 3. Then the gap is added to the structure, with the capacitive model explained in this Chapter. The return loss and insertion loss of the filter with the gap are given in Figures 4.8 and 4.9. The Sonnet results from ComDev are also shown in those Figures. As we can see, the results of our method agree with Sonnet results. There is about 0.4% difference in resonant frequency. Our method, especially the model for gap coupling, is very simple and fast in comparison with other methods.

There are good agreement between the resonant frequency in Figures 4.8 and 4.9. However, the return loss and insertion loss in these two figures are not the same as Sonnet results in pass bands. There are 5 dB difference in S_{11} , and 0.8 dB difference in S_{21} . We believe this happened, because of the fringe field at the end of open circuit stubs, in gap structure.

To include the effect of fringing fields at the end of the open circuit stubs, the length of stubs are increased by $h/2 = 0.254 \text{ mm}$. Considering longer stub length in our analysis, we get a better results. The results of our analysis with longer stub are shown in Figure 4.11 and 4.10. As we can see from the graph, in this case a better result could be achieved.

In this case the resonant frequency moves toward lower frequencies, but there is a better match in pass band. The error in resonant frequency is reduced to 0.2%.

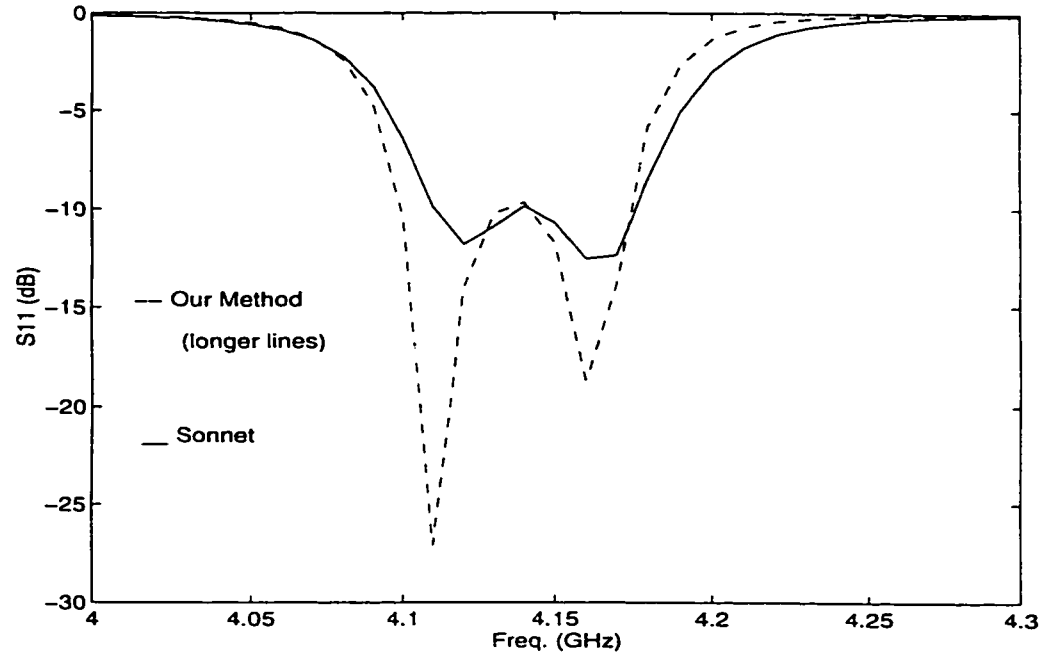


Figure 4.10: Gap coupled dual mode filter when longer stub is considered.

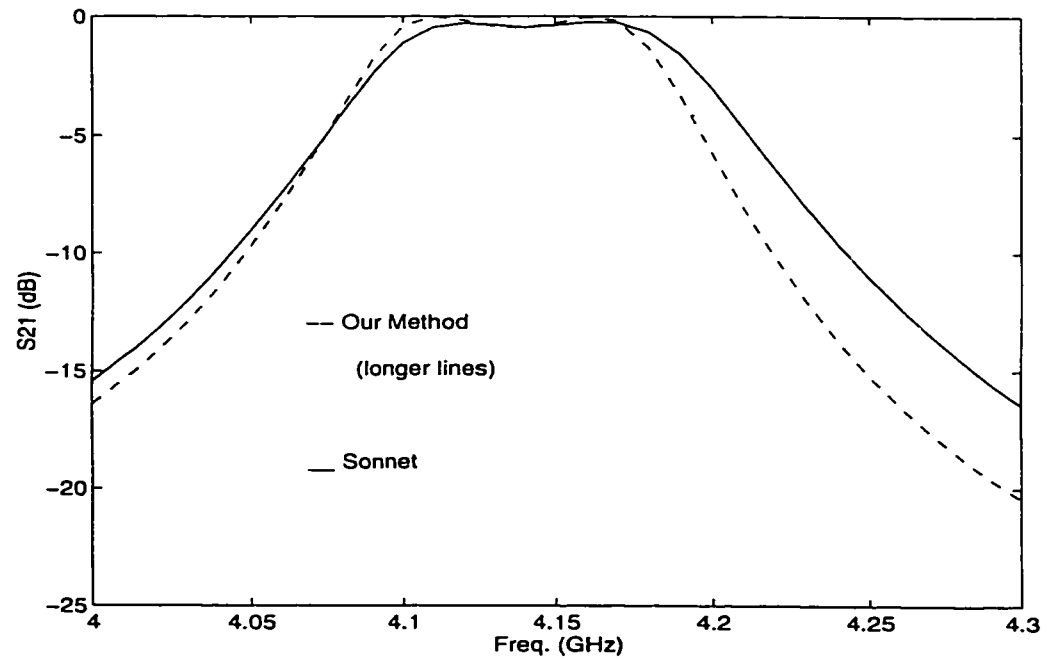


Figure 4.11: Gap coupled dual mode filter when longer stub is considered.

There is no difference between our analysis and Sonnet in pass band.

In these figures, the result of our simulation is not quite matched with Sonnet. There is possibility of error in Sonnet results. We believe Sonnet did not simulate the pass band since in dual mode filters usually there are two peaks and we can hardly get a flat curved in pass band.

There are some other similar filters which was designed by ComDev. For those structure better results were achieved, and our method was tested on those structures as well [56].

In this part of this research, we used two approximations to simplify our analysis. First approximation was in calculation of capacitance of the transmission line where the effect of ground plane was ignored. The second one was the open circuit stub model and ignoring the fringe field at the end of stub. In future, these approximations may be improved to have more accurate analysis.

Chapter 5

Coupling between Patches

5.1 Introduction

A patch structure is one of the simplest structures in microwave circuits and antennas. This structure is used as an element for complicated microwave circuits or in antenna arrays.

With the increasing interest in using patch elements for manufacturing of millimeter wave antennas, there is a need to accurately model the coupling as well as radiation in order to predict the input and far field pattern of antenna. Printed antennas tend to be formed into array of elements, and therefore coupling and feed line effects should also be considered in the design procedure. Some general field solving techniques which are used in the analysis of patch antenna such as FDTD [15] or MoM [57], can be applied to determine the characteristics of an array of microstrip patches. However, these methods are very slow when the number of elements increases and coupling between all elements are needed.

In some wide band antenna applications a patch is used with other elements

which are patch parasitic elements. In those structures, the analysis of coupling between the patch and different elements is important and should be accurately considered in analysis.

In microwave circuits, patch filters may have more than patch elements, such as 4-pole filters shown in Figure 5.1. In these case, coupling between different patches should be included in analysis of the filter.

In previous chapters, a new method was presented to analyze a single patch structures. In this chapter, we extend our method to analyze structures with more than one patch. In this analysis, the coupling between two patches is modeled by a fast and accurate method. In compare with other numerical methods, such as moment method, our presented method is faster and still accurate.

As examples for high order filters, we analyze 4-pole Chebyshev and Elliptic dual mode filters. The results of our method are compared with Sonnet results, as a bench mark, from ComDev.

5.2 Hybrid Method

In this section, a fast and accurate method is presented to analyze circuits with two patches or more. A similar idea, as presented in Chapter 3, has been developed to calculate the coupling between blocks in the circuit. Our method can be summarized into two steps.

First the circuit should be divided into simple blocks. The Z matrix of each block should be calculated, for instance using the method explained in Chapter 3 for each patch element. Using Z -parameters of these blocks, the multiport connection method [58] is used to analyze the structure. From the mathematical point of

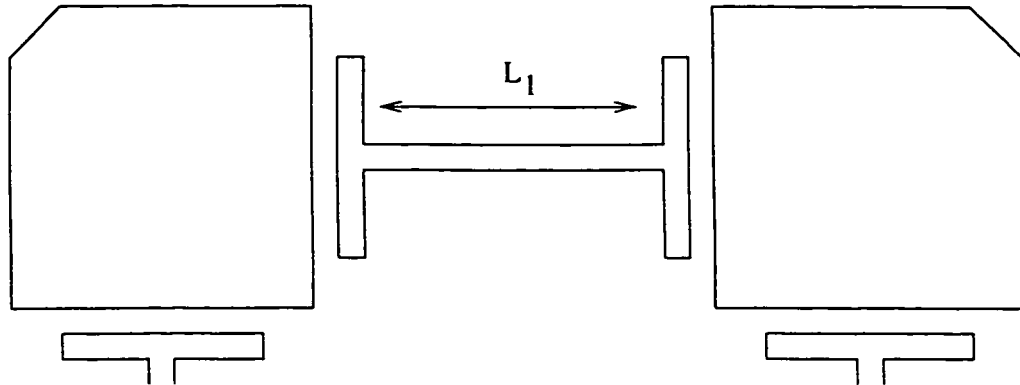


Figure 5.1: 4-pole Chebyshev dual mode filter

view, the multiport connection method is almost the same as the segmentation method described in Section 2.3. At this step, the analysis is not very accurate and the coupling between blocks is ignored, and the structure is considered as cascaded blocks. In the second step, we include the coupling between blocks using a double line integral expression which is a very fast one, in comparison with regular numerical methods.

5.2.1 Cascaded Blocks

To explain our method, we consider a 4-pole Chebyshev filter shown in Figure 5.1, as an example. This circuit can be considered as three blocks: two patches and one connecting line, Figure 5.2. The first patch with two ports (1) and (2) can be analyzed by our hybrid method explained in Chapter 3. The relation between voltage and current of two ports is given by the Z matrix of the patch as,

$$\begin{pmatrix} V_1 \\ V_2 \end{pmatrix} = \begin{pmatrix} Z_{11}^P & Z_{12}^P \\ Z_{21}^P & Z_{22}^P \end{pmatrix} \cdot \begin{pmatrix} I_1 \\ I_2 \end{pmatrix} \quad (5.1)$$

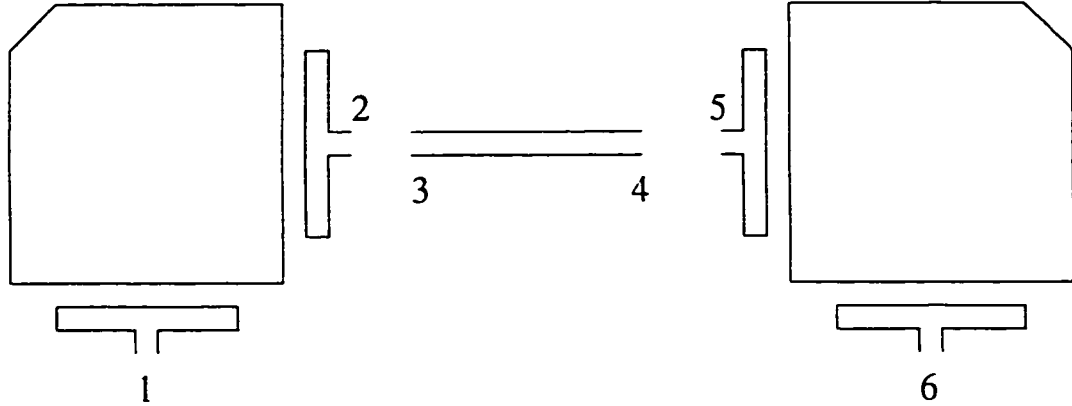


Figure 5.2: Three blocks in 4-pole Chebyshev dual mode filter

where Z_{ij}^p was defined in Section 3.1 as :

$$Z_{ij}^p = Z_{ij}^{2D} - \frac{1}{I_i I_j} \int_{Edge1} H(M_i) M_j ds + Z_g \delta_{ij} \quad (5.2)$$

In the above equation, the third term is added only because of the gap coupling in the patch shown in Figure 5.1. In Equation (5.2) Z_g is the impedance of the gap, as describe in Chapter 4, and should be added to the self term only (δ_{ij} is Kronecker delta).

For the next block, the connecting line with two ports (3) and (4) Figure 5.2, the relation between voltage and current of two ports is given by the Z matrix of the line as,

$$\begin{pmatrix} V_3 \\ V_4 \end{pmatrix} = \begin{pmatrix} -jZ_o \cot(\beta l) & -jZ_o \sec(\beta l) \\ -jZ_o \sec(\beta l) & -jZ_o \cot(\beta l) \end{pmatrix} \cdot \begin{pmatrix} I_3 \\ I_4 \end{pmatrix} \quad (5.3)$$

where l is the length of transmission line, and Z_o and β are the characteristic impedance and propagation constant of the line. In the above formulation, for simplicity, a transmission model is considered for this piece of microstrip and the

radiation from the strip is ignored. Here, using this model is a good approximation for our case in which the circuit is in a box. For general formulation, and including the radiation, a general moment method may be used, as briefly explained in Section 2.4 [14].

Similarly, for the second patch, with ports (5) and (6) in Figure 5.2, the relation between voltage and current of two ports is given by Z matrix of the second patch as,

$$\begin{pmatrix} V_5 \\ V_6 \end{pmatrix} = \begin{pmatrix} Z_{55}^p & Z_{56}^p \\ Z_{65}^p & Z_{66}^p \end{pmatrix} \cdot \begin{pmatrix} I_5 \\ I_6 \end{pmatrix} \quad (5.4)$$

where Z_{ij}^p is similar to (5.2), but calculated for the second patch.

Now after finding the Z matrix of each block, (5.1), (5.3) and (5.4), we can use the segmentation method describe in Section 2.3. The voltage and current variables for the connected ports (i.e. 2, 5 and 3, 4) and external ports (i.e. 1, 2) are grouped separately, as shown in the following matrix equation,

$$\begin{pmatrix} V_1 \\ V_6 \\ \dots \\ V_2 \\ V_5 \\ \dots \\ V_3 \\ V_4 \end{pmatrix} = \begin{pmatrix} Z_{11}^p & 0 & \vdots & Z_{12}^p & 0 & \vdots & 0 & 0 \\ 0 & Z_{66}^p & & 0 & Z_{65}^p & & 0 & 0 \\ \dots & \dots & & \dots & \dots & & \dots & \dots \\ Z_{21}^p & 0 & \vdots & Z_{22}^p & 0 & \vdots & 0 & 0 \\ 0 & Z_{56}^p & & 0 & Z_{55}^p & & 0 & 0 \\ \dots & \dots & & \dots & \dots & & \dots & \dots \\ 0 & 0 & \vdots & 0 & 0 & \vdots & -jZ_o \cot(\beta l) & -jZ_o \sec(\beta l) \\ 0 & 0 & & 0 & 0 & & -jZ_o \sec(\beta l) & -jZ_o \cot(\beta l) \end{pmatrix} \cdot \begin{pmatrix} I_1 \\ I_6 \\ \dots \\ I_2 \\ I_5 \\ \dots \\ I_3 \\ I_4 \end{pmatrix} \quad (5.5)$$

The advantage of the above formulation is the possibility of including coupling between ports in future steps. The above coefficient matrix (6×6) is divided into 9 submatrices for simplicity in matrix manipulations. Therefore, the above coefficient matrix can be rewritten as,

$$\begin{pmatrix} Z_{aa} & Z_{ab} & Z_{ac} \\ Z_{ba} & Z_{bb} & Z_{bc} \\ Z_{ca} & Z_{cb} & Z_{cc} \end{pmatrix} \quad (5.6)$$

All submatrices in (5.6) are 2×2 , and the elements of these submatrices are defined in the coefficient matrix in (5.5).

To connect the blocks and reduce the above matrix to the Z -matrix of the circuit, we have to apply the boundary conditions which are:

$$V_2 = V_3 \quad , \quad V_4 = V_5 \quad (5.7)$$

$$I_2 = -I_3 \quad , \quad I_4 = -I_5 \quad (5.8)$$

Using (5.7) and (5.8) in (5.5), we can get the overall Z -matrix of the circuit (between port 1 and port 6). This overall Z -matrix is calculated as,

$$Z = Z_{aa} + (Z_{ab} - Z_{ac})(Z_{bb} - Z_{bc} - Z_{cb} + Z_{cc})^{-1}(Z_{ca} - Z_{ba}) \quad (5.9)$$

It should be mentioned that in the above matrix equation all the submatrices are defined in (5.5) and (5.6), and we have,

$$Z_{ac} = Z_{bc} = Z_{ca} = Z_{cb} = 0$$

Therefore, (5.9) reduces to the following matrix equation,

$$Z = Z_{aa} - Z_{ab}(Z_{bb} + Z_{cc})^{-1}Z_{ba} \quad (5.10)$$

Using the above Z-matrix, we can calculate other parameters, such as S-parameter, of the circuit.

5.2.2 Mutual Couplings

In this section a general method is presented to calculate the coupling between patches. However, for simplicity the method is explained for patches with two ports as shown in Figure 5.1. The method is easily expandable for structures with three port patches such as for the Elliptic filter which will be analyzed at the end of this chapter.

In this structure, Figure 5.1, on each patch there are two sets of modes driven by two ports. Therefore the coupling between two patches are coupling between these modes. In this section, to calculate these couplings, a very fast method is presented without sacrificing accuracy.

As we mentioned in the last step, Equation (5.5), the coupling between two patches is ignored. To include the coupling between patches, we could calculate the coupling between modes in two patches. Using variational expression, coupling between modes can be written as:

$$Z_{ij}^{P_1 P_2} = \frac{1}{I_i^{P_1} I_j^{P_2}} \int_{Patch2} E(J_i^{P_1}) \cdot J_j^{P_2} ds \quad (5.11)$$

where $J_i^{P_1}$ and $J_j^{P_2}$ are currents on patch one and patch two, $i = 1, 2$ and $j = 5, 6$ relates to ports of patch one and patch two, respectively. It is clear that the above

integral is a double surface integral on the surface area of the patches; therefore, it is very time consuming.

From the above variational expression, we have to calculate four coupling terms. It should be mentioned that we use reciprocity, $Z_{ij}^{P_1 P_2} = Z_{ji}^{P_2 P_1}$, so there are really eight terms which should be put in the Z-matrix, (5.5). Therefore, the total Z-matrix in (5.5) is changed to:

$$\begin{pmatrix} Z_{11}^P & Z_{16}^{P_1 P_2} & \vdots & Z_{12}^P & Z_{15}^{P_1 P_2} & \vdots & 0 & 0 \\ Z_{61}^{P_1 P_2} & Z_{66}^P & & Z_{62}^{P_1 P_2} & Z_{65}^P & & 0 & 0 \\ & \dots & & \dots & & & \dots & \\ Z_{21}^P & Z_{26}^{P_1 P_2} & \vdots & Z_{22}^P & Z_{25}^{P_1 P_2} & \vdots & 0 & 0 \\ Z_{51}^{P_1 P_2} & Z_{56}^P & & Z_{52}^{P_1 P_2} & Z_{55}^P & & 0 & 0 \\ & \dots & & \dots & & & \dots & \\ 0 & 0 & \vdots & 0 & 0 & \vdots & -jZ_o \cot(\beta l) & -jZ_o \sec(\beta l) \\ 0 & 0 & & 0 & 0 & & -jZ_o \sec(\beta l) & -jZ_o \cot(\beta l) \end{pmatrix} \quad (5.12)$$

As mentioned before, calculation of the coupling terms between two patches by Equation (5.11), is a double surface integral on the surface area of two patches; therefore, it is very time consuming. To increase the speed of the calculation, without sacrificing the accuracy, we transform the double surface integral to a double line integral, similar to the method explained in Chapter 3.

The expression in (5.11) is exact, if the currents are known. Since this expression is variational, we could replace the current with an approximated one. The first approximation for the currents is the one from 2D analysis. In 2D methods, each patch can be modeled by a cavity with magnetic wall. Therefore, there will be electric current J on the patch and magnetic current M on the magnetic wall

(Edge). The total tangential electric field due to electric and magnetic currents of each patch is zero. Therefore, for magnetic and electric currents of patch one, we can write,

$$E_{tan}(J_i^{P1}) + E_{tan}(M_i^{P1}) = 0 \quad (5.13)$$

So, we can replace $E_{tan}(J_i^{P1})$ by $-E_{tan}(M_i^{P1})$ in (5.11):

$$Z_{ij}^{P1P2} = \frac{-1}{I_i^{P1} I_j^{P2}} \int_{Patch2} E_{tan}(M_i^{P1}) \cdot J_j^{P2} ds \quad (5.14)$$

Using reciprocity between electric current on the second patch and the magnetic current on the edge of the first patch, we can rewrite (5.14) as,

$$Z_{ij}^{P1P2} = \frac{1}{I_i^{P1} I_j^{P2}} \int_{Edge1} H_{tan}(J_j^{P2}) \cdot M_i^{P1} ds \quad (5.15)$$

On the edge of the first patch (PMC), the tangential component of magnetic field is zero, so we have $H_{tan}(J_j^{P2}) = -H_{tan}(M_j^{P2})$. Therefore, (5.15) reduces to

$$Z_{ij}^{P1P2} = \frac{-1}{I_i^{P1} I_j^{P2}} \int_{Edge1} H_{tan}(M_j^{P2}) \cdot M_i^{P1} ds \quad (5.16)$$

The above expression, (5.16), is a double line integral on the edges of the patches, therefore, it is much faster than (5.11).

After finding coupling terms, using Z-matrix in (5.12), we can find the overall Z-parameter of the circuit (between port 1 and port 6). In the same way as before, to reduce the Z-matrix in (5.5) to the Z-matrix of the circuit, we have to apply the boundary conditions in (5.7) and (5.8). Using the same procedure, the Z-parameter of the circuit, can be found as (5.10). However, here the definition of matrices is based on (5.6) and (5.12).

5.3 Numerical Results

As a verification for our new presented method, in this section two structures are analyzed by our method and the results are compared with the Sonnet results from ComDev. As mentioned earlier, in experiment there are tolerances in dielectric and dimension of a circuit. Therefore, the experimental results may change from sample to sample. However, to verify our method, we need reliable results. As a benchmark, we use Sonnet result provided by ComDev to compare with our simulated results.

5.3.1 Chebyshev Filter

A 4-pole Chebyshev filter, shown in Figure 5.1, is analyzed by the method explained in this Chapter. Then the numerical results of our method are compared with Sonnet results from ComDev.

This filter was designed in a box, and the effect of box is considered in Sonnet. However, in our simulation the Green's function of multilayer structure has been used. So, the top cover of box is considered as an infinite metallic layer in calculation of the Green's function. Since there is no radiation from the circuit in the box, we delete the real part of Z-parameter of the circuit. The real parts of coupling terms are also deleted to remove the radiation effect due to surface waves. However, the real parts of coupling terms are very small in compare with the imaginary parts. To show the effect of different part of the circuit; such as gap coupling, coupling between patches, and box, the output of our simulation was presented in different steps of simulation.

The Chebychev filter was design by ComDev, and it has equi-ripple in pass

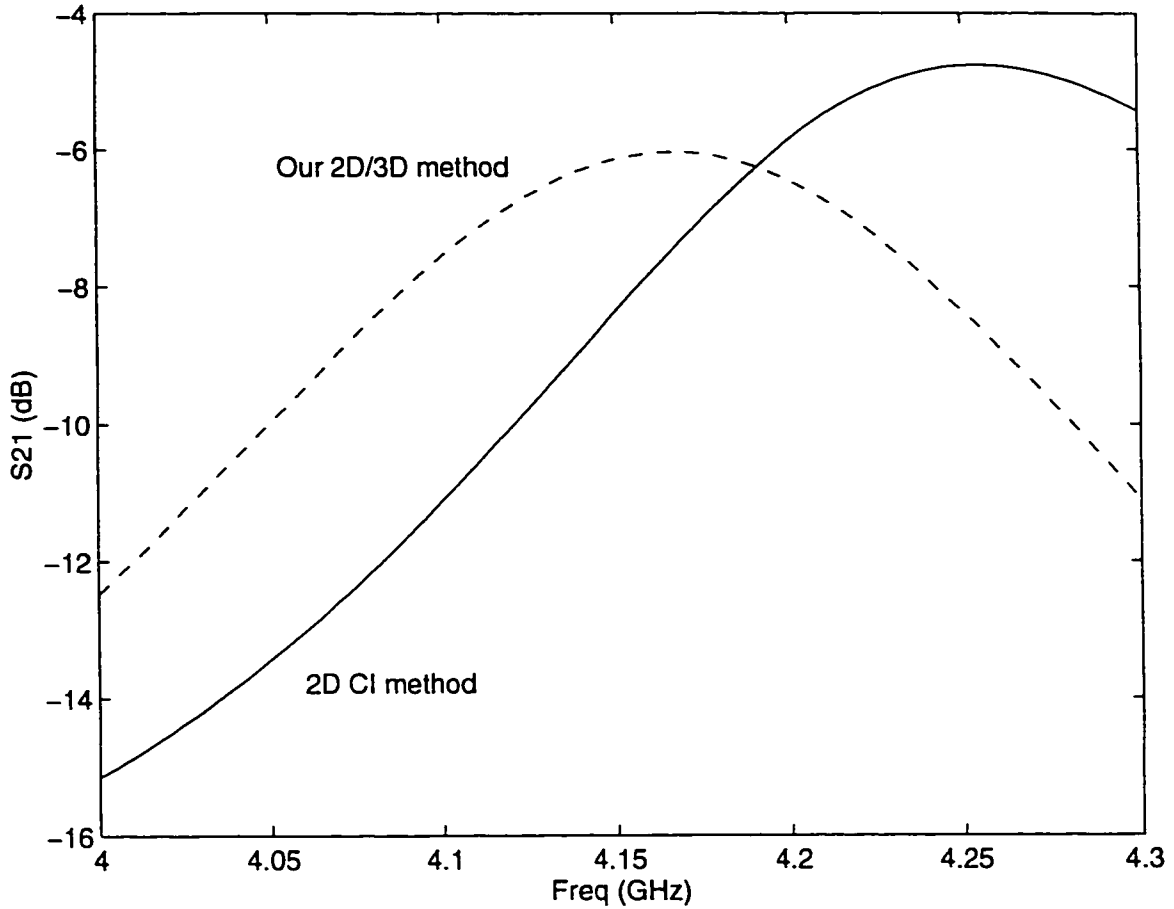


Figure 5.3: 2D contour integral method, and our 2D/3D method.

band. The filter was simulated by our method and very good results were achieved [56]. In here similar structure will be analyzed, however, the frequency response is not quite like a Chebychev filter.

The dimensions of each patch, defined in Figure 4.7, are $a = 7.419 \text{ mm}$, $b = 6.368 \text{ mm}$, $s = g = 58.42 \text{ } \mu\text{m}$, $l_g = 5.083 \text{ mm}$, $w = 0.175 \text{ mm}$, and the distance between two patches is $L_1 = 7.886 \text{ mm}$, Figure 5.1. The substrate height is $h = 0.508 \text{ mm}$, and dielectric constant is $\epsilon_r = 24$.

In the first step, we have to analyze one patch only with direct connection which

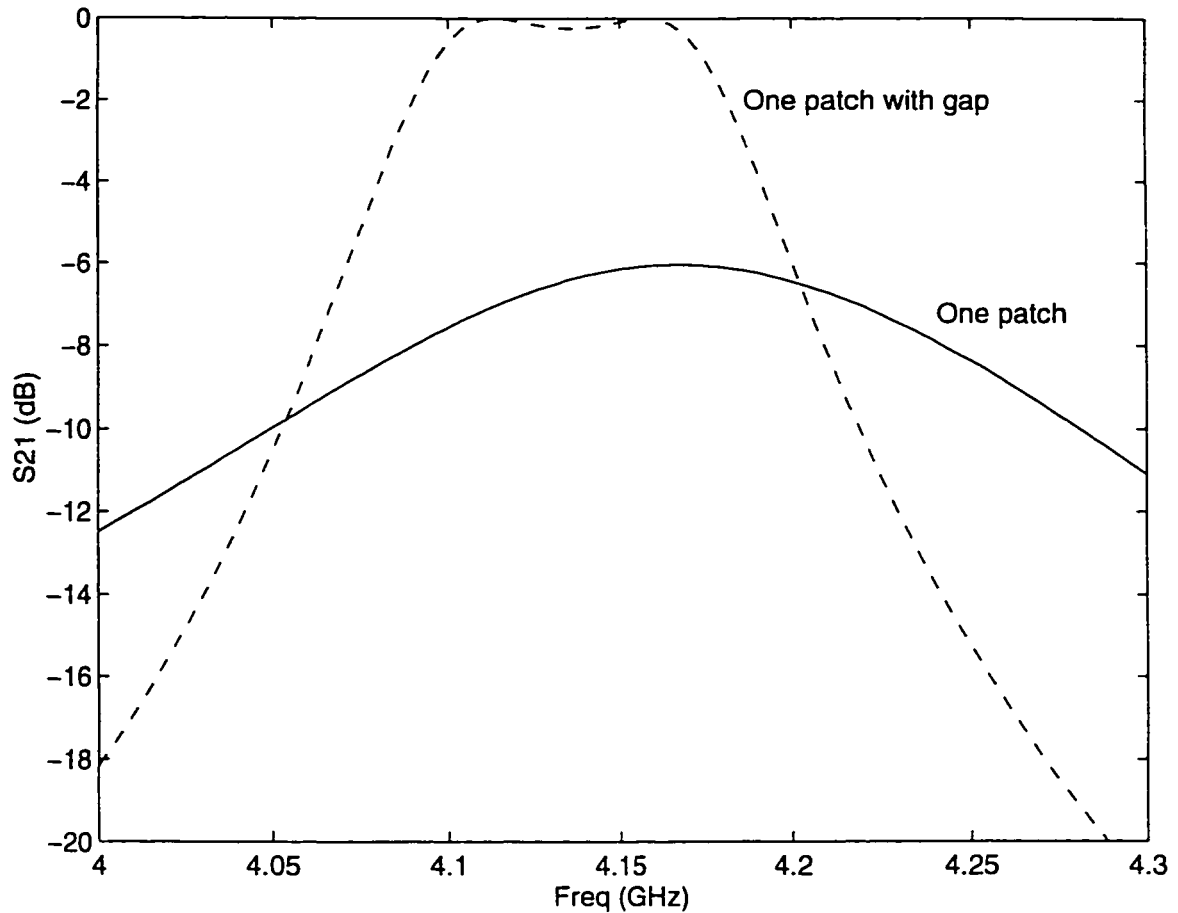


Figure 5.4: Insertion loss of one patch with direct coupling and gap coupling.

is simply a dual mode filter. To analyze this dual mode filter, our hybrid 2D/3D method presented in Chapter 3 is used. The results of 2D contour integral (CI) analysis and 2D/3D method (our method) are shown in Figure 5.3. The capacitive fringe field of the edge changes the input impedance and reduces the resonant frequency by 2% (4.255 GHz to 4.165 GHz).

In the next step, to include the gap coupling, the transmission line model for gap structure, explained in Chapter 4, is added. The results of simulation for one patch with direct connection and gap coupling is given in Figure 5.4.

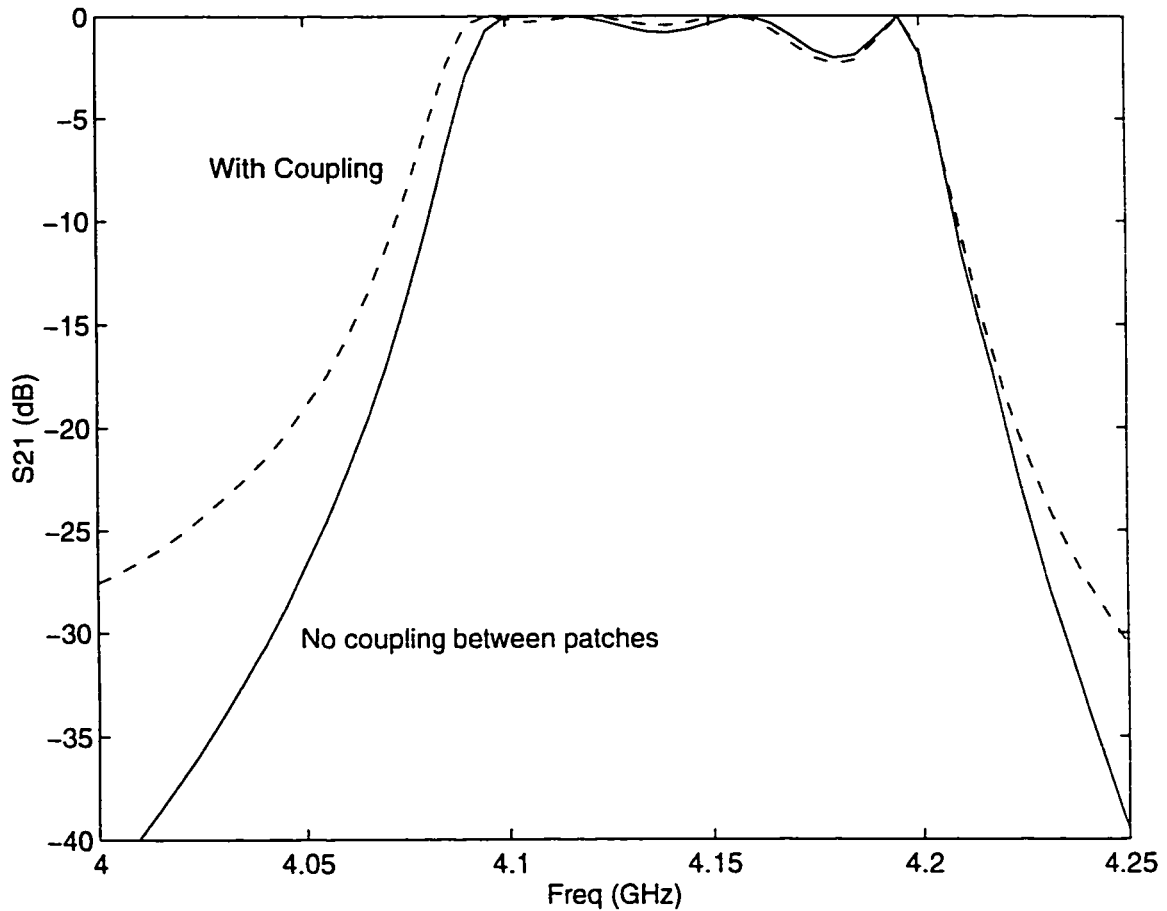


Figure 5.5: Insertion loss of filter with and without coupling between patches.

As we can see in Figure 5.4, the gap coupling changes the input impedance for better match. It increases the Q due to loose coupling [48].

At the next step, after adding a gap structure to one patch, we put two patches in cascade with a connecting transmission line between them, Figure 5.1. When the coupling between patches are not included, and the blocks are cascaded, we can follow the procedure in Section 5.2.1. Considering coupling between two patches, we apply the method explained in Section 5.2.2. The numerical results from these two analyses are shown in Figure 5.5.

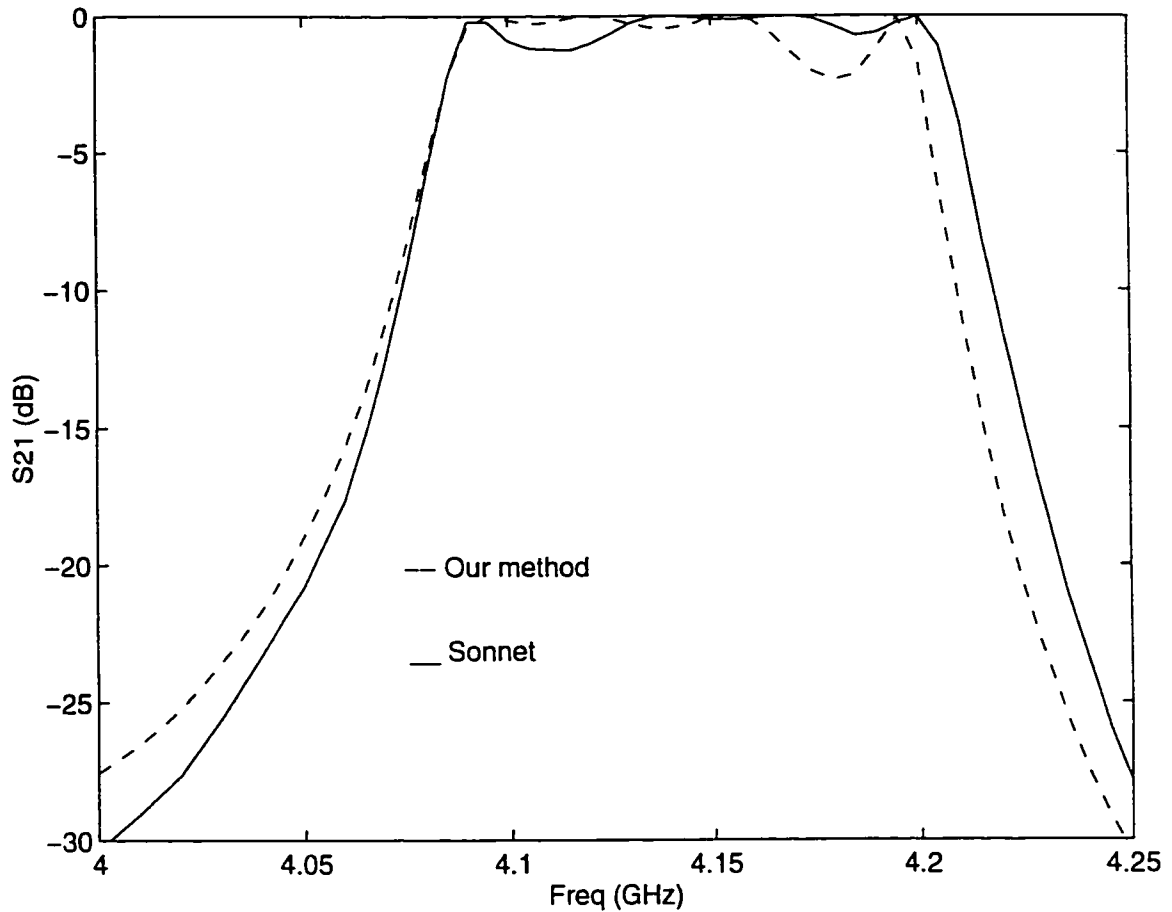


Figure 5.6: Results of S_{21} from our method and Sonnet.

The result of our simulation using the new method to calculate coupling between patches is also compared with Sonnet results from ComDev. Both results from our method and Sonnet are shown in Figures 5.6 and 5.7.

As we can see, there is a good agreement between two results, especially in resonance frequency. The difference in resonant frequency is around 0.1%, which means our method is very accurate in predicting the resonant frequency. It should be mentioned that Sonnet considers the metalization thickness in its analysis. However, in our analysis this thickness is ignored. The metalization thickness may be

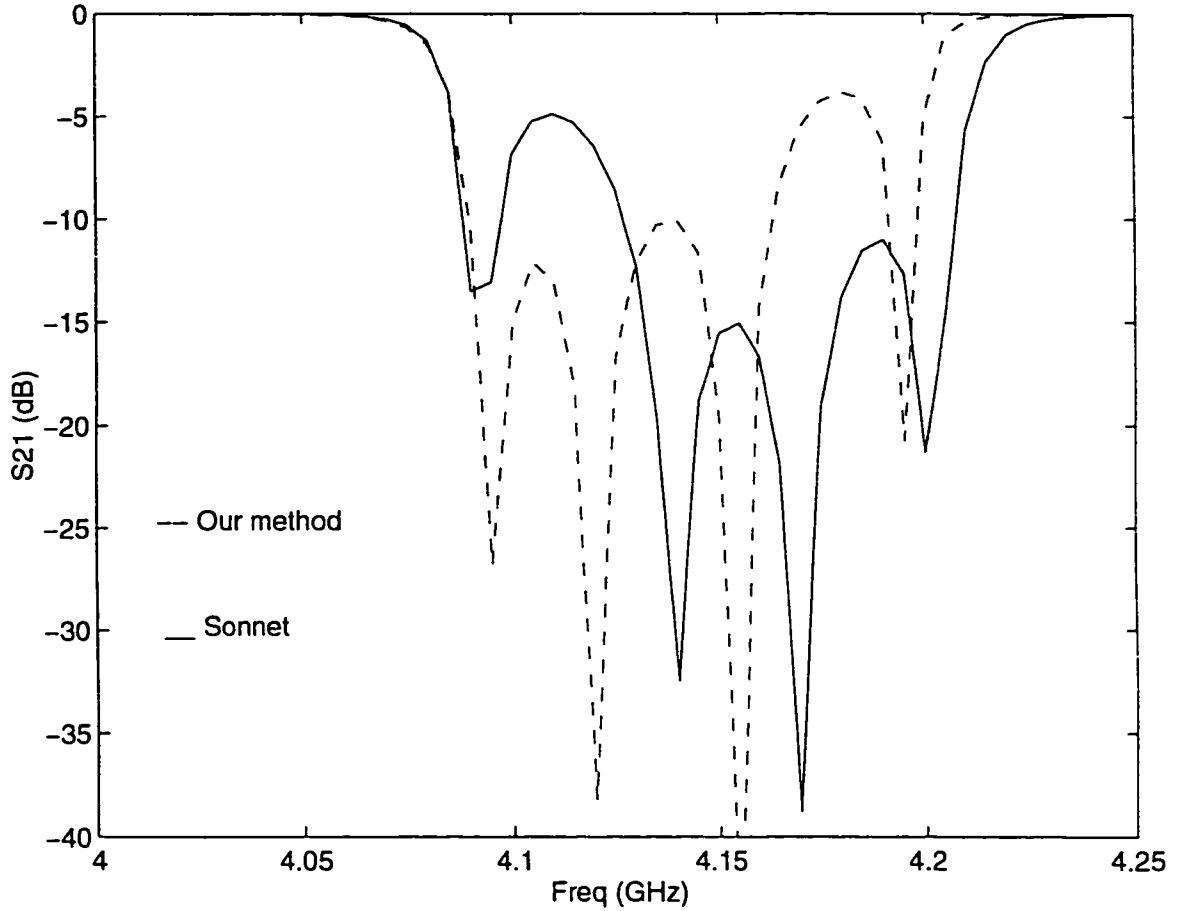


Figure 5.7: Results of S_{11} from our method and Sonnet.

reduce the resonant frequency.

For this filter, Sonnet gives -1.25 dB ripple in pass band, and we get about -2.25 dB ripple. There is also a maximum difference of 3 dB between Sonnet and our method at two edges. This means that there is a voltage deviation of 0.8% between two methods at those frequencies.

In terms of speed, our method is faster than Sonnet. For the results of this filter Sonnet spends about 16 minutes and our method spends about 12 seconds for each frequency. This means that ours is about 80 times faster than Sonnet. These

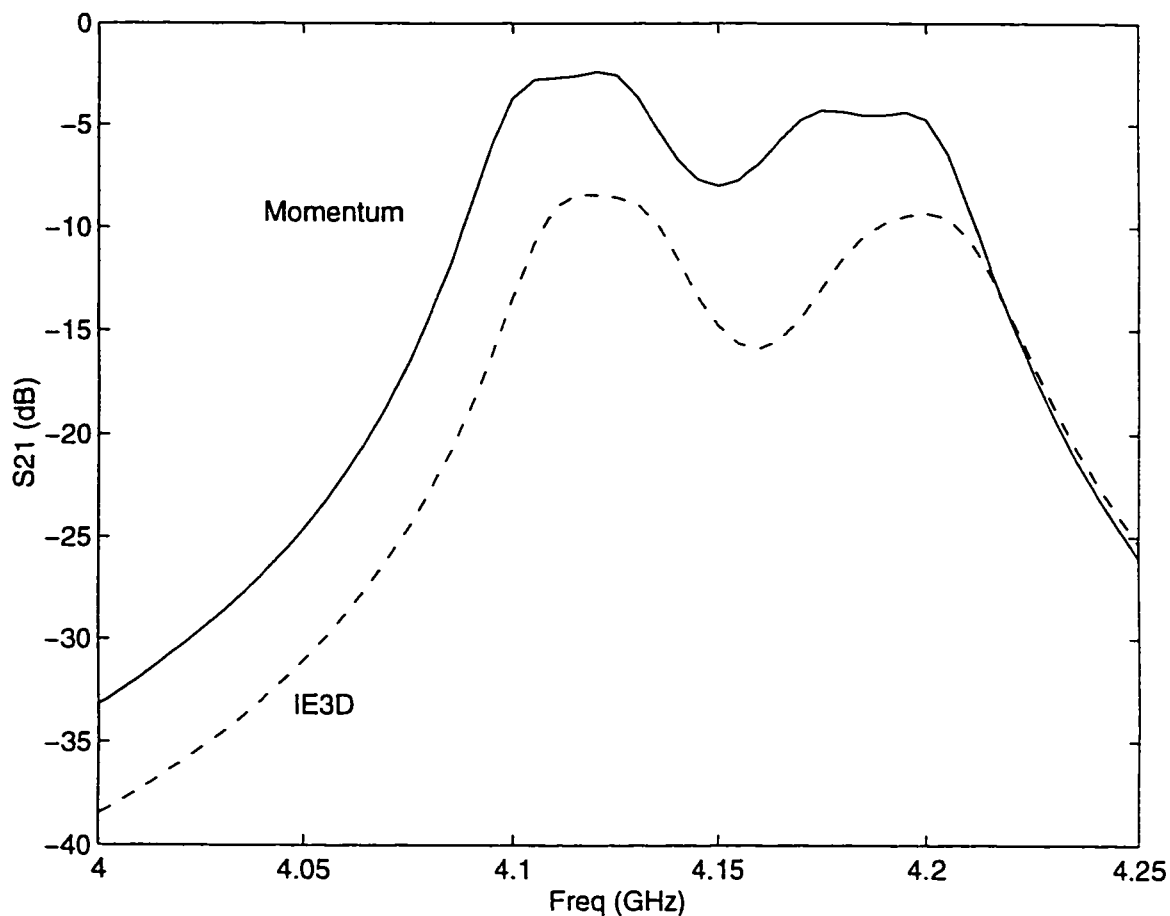


Figure 5.8: IE3D and Momentum results for the structure with radiation (no box).

times were calculated based on HP-Unix system (series 735). We have to consider that Sonnet is one of the best commercial software in the market, and uses advance computer algorithms to increase the speed.

The difference between two results, our simulation and Sonnet, in Figure 5.6 and 5.7 is because of the box effect. In our analysis, we simulate the box by putting a top metallic cover and delete the radiation. However, the effect of side walls in box were not considered in our simulation.

The effect of box is very important in the characteristic of this structure. The

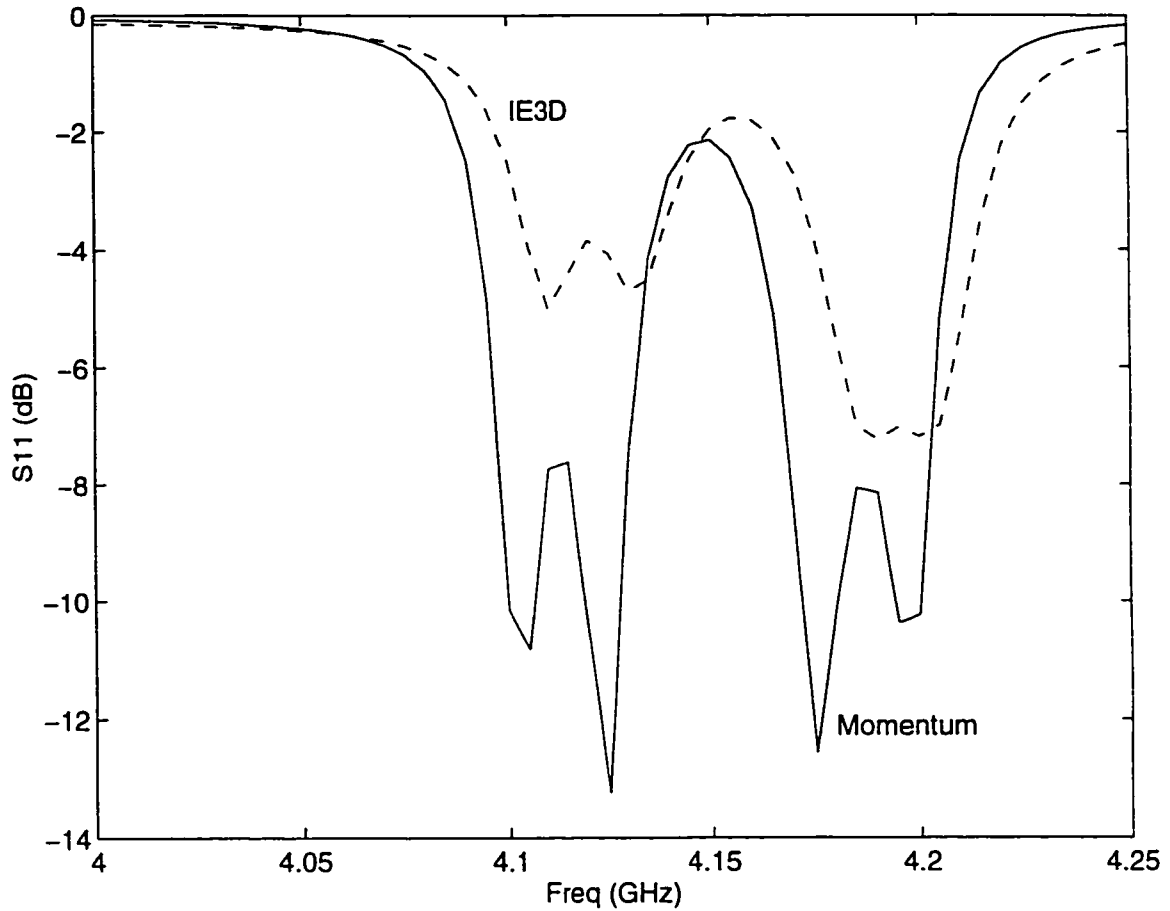


Figure 5.9: S_{11} from IE3D and Momentum simulations.

structure without box is also simulated using two other commercial softwares, IE3D and Momentum. These two methods are based on moment method. The results from these two methods are shown in Figure 5.8 and 5.9.

As we can see from the graphs in Figure 5.8 and 5.9, there is a radiation from the structure with no box. At center frequency, say 4.15 GHz in IE3D simulation, there is about -2 dB as reflected wave and -14.8 dB as transmitted. Therefore, there is about -9.5 dB radiation loss. This value for Momentum is about -13 dB.

IE3D and Momentum are two programs that use moment method as their base

of numerical calculation. However, their results are different especially in pass band. This difference is due to error in the numerical method. These softwares are very well known, however, they are not very accurate for structures with big radiating elements.

From the result of Momentum (or IE3D) and Sonnet, it is clear that box has an important role in the characteristics and performance of the circuit, and should be modeled more accurately.

5.3.2 Elliptic Filter

Another structure is a 4-pole Elliptic filter designed by ComDev [59], and shown in Figure 5.10. The structure was analyzed by our new method and good agreement between our result and Sonnet was achieved [56].

In here a similar structure is analyzed. The numerical result of our method is compared with Sonnet result which is our bench mark as explained. The dimension of this structure is the same as the one in previous section, and $L_2 = 1.81 \text{ mm}$, Figure 5.10.

To analyze this filter, we follow the procedure explained in Section 5.2. However, each patch element is considered as a three port network, therefore the Z-matrix of each patch is a 3×3 matrix, in Equations (5.1) and (5.4). In analyzing this filter, similar to Chebyshev, the coupling between each patch and connecting lines are ignored. The coupling between two lines is also ignored, in the formulation. In the simulation, we found that the coupling between those two lines does not effect the results.

The Elliptic filter is also designed in a box, and we simulate the effect of the box by deleting the real part of the Z-matrices. The response of the Elliptic filter is

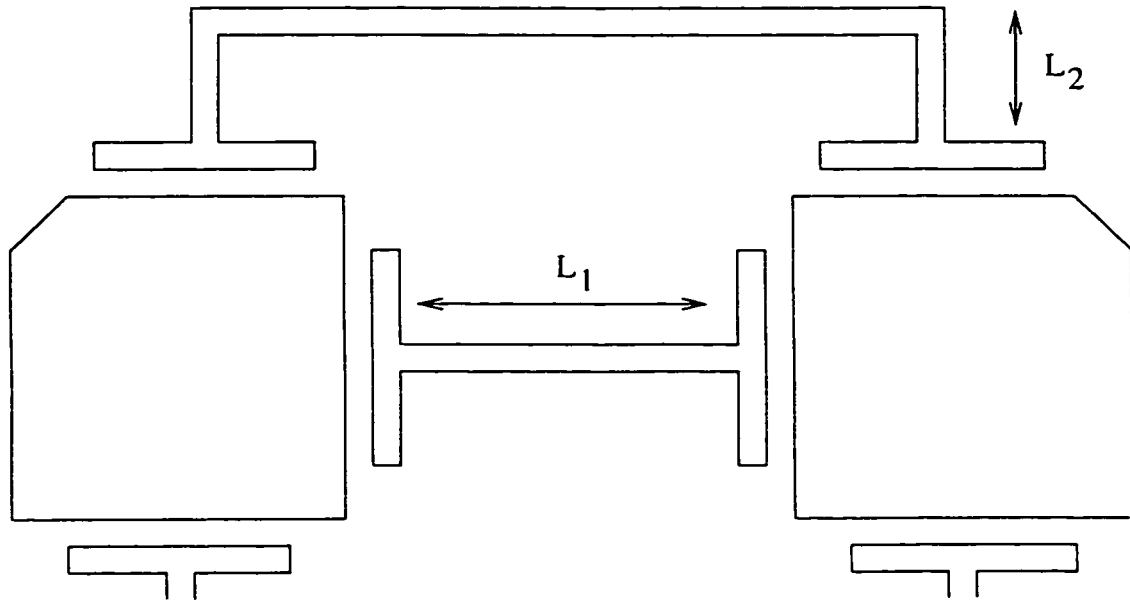


Figure 5.10: 4-pole Elliptic filter.

very similar to Chebyshev one, so in this section the response of the whole circuit is presented, and the responses of each block is not presented.

The result of our simulation using the new method in calculation of coupling between patches is compared with Sonnet results from ComDev. Both results from our method and Sonnet are shown in Figure 5.11 and 5.12. It is clear from the graphs, there is a good agreement between two results, especially in the resonant frequency. The difference in resonant frequency is around 0.2%, which means our method is accurate in predicting the resonant frequency. As mentioned before, in our analysis we do not consider the metalization thickness, and this may be a source of error in resonant frequency.

As mentioned before, Sonnet considers the structure in a box, and we did not accurately model the box. The difference between results of our simulation and Sonnet is due to box effect. To have a better result, we have to use Green's function

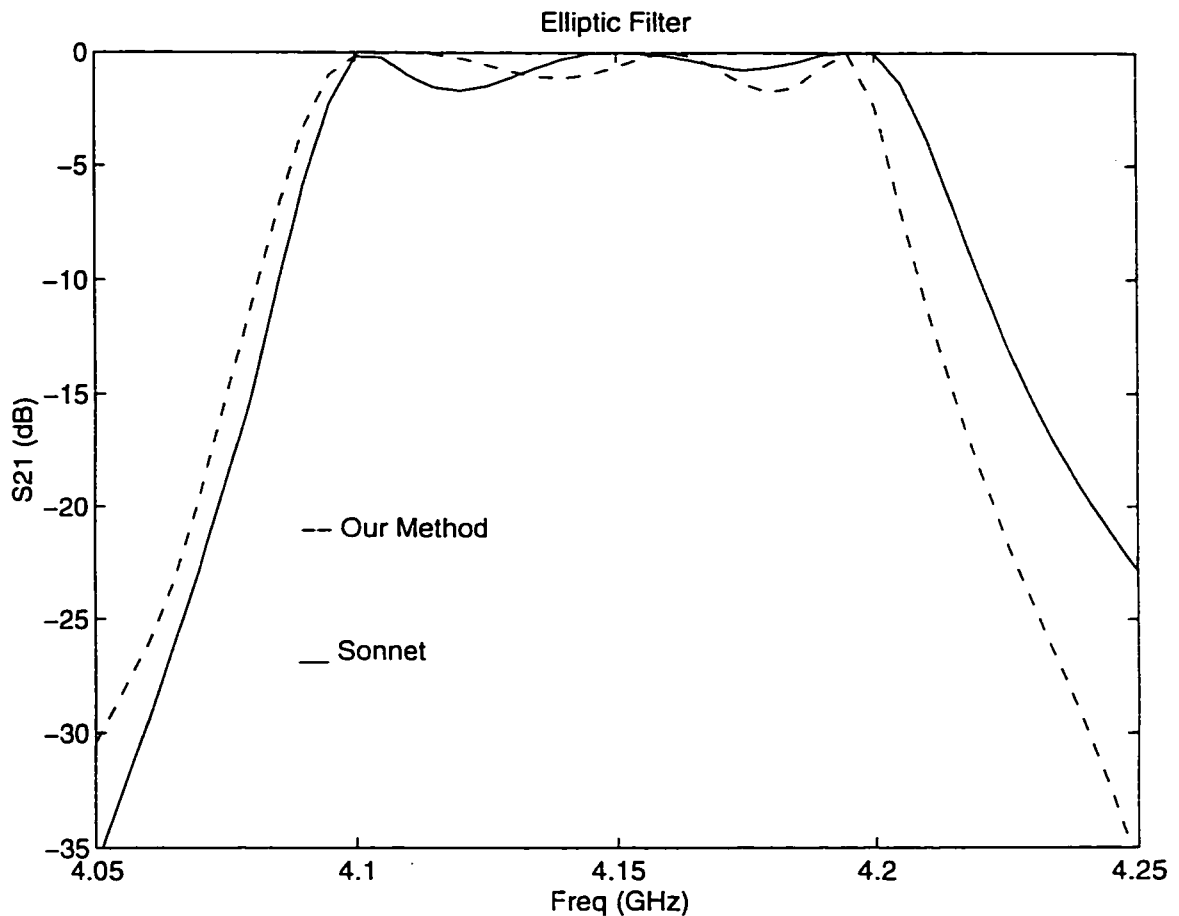


Figure 5.11: S_{21} for Elliptic filter from our method and Sonnet.

of multilayer structure in a box.

Similar to the Chebychev filter, the coupling between lines are ignored in the simulation of this Elliptic filter. The simulation was also done considering the coupling between two lines, and the same result was achieved.

For this filter, our method spends 15 seconds and Sonnet spends 20 minutes. This means our method is about 80 times faster than Sonnet. The speeds of two methods are based on HP-Unix system (series 735). As we expected, our method is very fast. The accuracy is not sacrificed for the speed, and the method has good

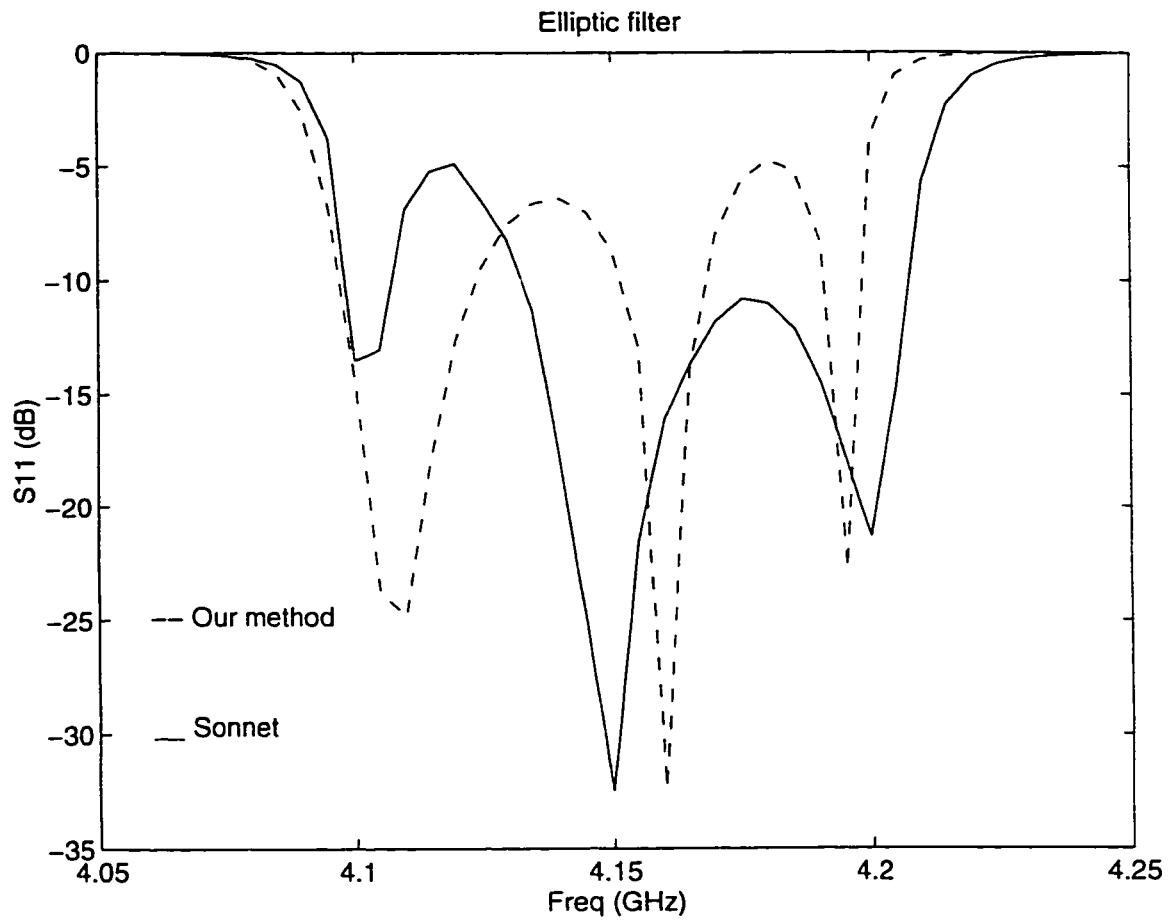


Figure 5.12: Results of S_{11} from our method and Sonnet.

accuracy. This means our algorithm can compete with one of the best commercial CAD tools in this area.

Chapter 6

Simulated Images

6.1 Introduction

To analyze patch resonators with our method, we have to calculate the magnetic (or electric) field due to magnetic current on the edge of patches. To calculate the field in a multilayer structure, we can use the *complex images technique*. However, a new and simpler method is developed in this work, and used in our hybrid method to analyze patch resonators. This new method which is also fast, is called the *simulated images technique*.

To avoid time consuming numerical Sommerfeld integrals in calculating spatial Green's functions in multilayer structure, Chow et al [33] developed the complex images technique to arrive at a closed form spatial Green's function for the thick microstrip substrate. This technique was also developed for calculation of Green's functions of a multilayer structure [60]. The complex images technique considers the spectral Green's function to be the result of three factors: quasi-dynamic images, surface wave and complex images. Quasi-dynamic images, developed by

Chow [55], are used to model near field potentials, replacing the traditionally utilized Sommerfeld integrals and dominating the spectral Green's function in the region immediately adjacent to the source. The surface waves contribution manifests itself in the form of poles in the Green's function which dominate the function in the far field regions on the surface of the substrate. The remaining part of the Green's function dominating the intermediate region between near and far field, is represented as complex images having complex amplitudes as well as complex locations.

Sophisticated as they sound, *complex images*, are derived from curve fitting in the spectral domain of a multilayer medium, and are therefore non unique. This non uniqueness leads to the possibility of complex images with fixed real locations which do not require the complicated and computationally expensive Prony's method to solve for the amplitudes and locations of complex images. Such images may be called simulated images [39]. This Chapter shows that with nearly three or four simulated images positioned in the static image locations, the simulated images technique results in a Green's function as accurate as that derived using the complex images technique. The new technique has a very good accuracy, specially in the low frequency range. It can be used at higher frequencies; however, higher a number of images should be considered to include the far field and higher frequency effects, such as surface wave effect. On the other hand, the fixed image locations lead to fast and convenient computations which can be used for wide band (e.g. digital) applications.

In this chapter, we start with a brief review of Green's function in the spectral domain. The simulated images method is then explained, and at the end some numerical results are presented.

6.2 Green's Functions of Multilayer Structure

The spatial domain Green's functions are represented by the Sommerfeld integral [61] as

$$G = \frac{1}{4\pi} \int \tilde{G}(k_\rho) H_o^{(2)}(k_\rho \rho) k_\rho dk_\rho \quad (6.1)$$

where G and \tilde{G} are the Green's functions in the spatial and spectral domains, respectively, $H_o^{(2)}$ is the Hankel function of the second kind. The Sommerfeld integral given in (6.1) cannot be integrated analytically, except for a few special cases. The integrand of (6.1) is also an oscillatory and slowly decaying function, so the numerical calculation is very time consuming if not impractical for many configurations. Moreover, the singularities of the integrand (correspond to the surface wave poles of the spectral Green's function) add to the complexity of evaluating such an integral. In the next section, a method is explained to approximate the evaluation of the Green's function in the spectral domain and calculate the integral to find the spatial Green's function. Before that, we have to derive the Green's function in the spectral domain.

To derive the spectral domain Green's functions for a multilayer medium shown in Figure 6.1, we can use a multisection transmission line model. The propagation through the line sections, layers, is simply given by a chain product of a series of wave transmission matrices [A]. The details of this method is given in [60]. Using this method all Green's functions can be derived in the spectral domain. Here, the most common two Green's functions, vector and scalar potentials for a horizontal electric dipole are listed.

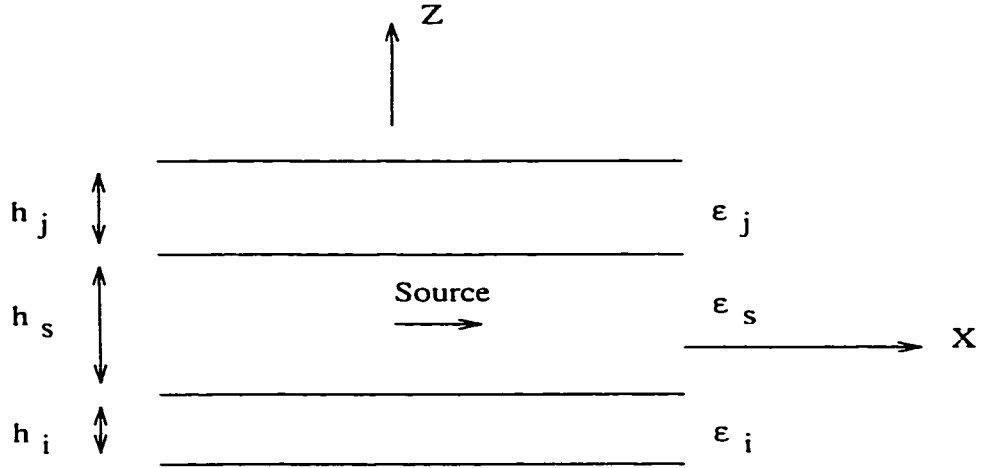


Figure 6.1: Multilayer planar structure with embedded source.

$$\bar{A}_{xx} = \frac{1}{2jk_{zs}} T^{TE} \quad (6.2)$$

$$\bar{Q}_x = \frac{1}{2jk_{zs}\epsilon} \left[T^{TE} + \frac{k_{zs}^2}{k_p^2} \left(T^{TE} \mp \frac{jk_{zs}}{k_{zf}^2} \frac{\partial T^{TM}}{\partial z_f} \right) \right] \quad (6.3)$$

where the subscripts s and f refer to source and field layers, and the transfer functions, T , have superscripts for transmissions of TE or TM waves.

For the vertical electric dipole, there is another vector potential Green's function:

$$\bar{A}_{zx} = \frac{-k_x}{2jk_{zs}} \frac{\mu_s}{\mu_f k_p} \left(\frac{\mu_f k_{zs}}{\mu_s} T_{TM}^H - j \frac{\partial T_{TE}^H}{\partial z_f} \right) \quad (6.4)$$

The closed form Green's functions, in the spectral domain, for vector and scalar potentials of a horizontal electric dipole (HED), vertical electric dipole (VED), horizontal magnetic dipole (HMD) and a vertical magnetic dipole (VMD) located in an arbitrary layer of a planar layered medium are listed in Appendix D. In the

following section, our method is explained to calculate these Green's functions in the spatial domain.

6.3 Simulated Images Technique

As mentioned before, the approximation of Green's function by images are not unique, and different sets of images can be used. Therefore, the simulated images method and the complex images method are similar. In this section only the details of simulated images are presented, and for details of complex images you may read some references in the literatures [33, 62].

As mentioned, evaluating the Sommerfeld integral (6.1) is very difficult or impossible. However, this integral has an analytical solution for a specific case. If the spectral domain representation of the Green's function \tilde{G} , is a complex exponential then an analytical evaluation of the integral becomes possible via the Sommerfeld identity which is,

$$\frac{e^{-jk_r r}}{r} = \int \frac{e^{-jk_z |z|}}{2jk_z} H_0^{(2)}(k_\rho \rho) k_\rho dk_\rho \quad (6.5)$$

where $r = \sqrt{\rho^2 + z^2}$ and $k_z = \sqrt{k^2 - k_\rho^2}$. Therefore, if the spectral Green's function can be approximated in terms of complex exponentials, then the Green's function in the spatial domain can be derived analytically.

The contributions of the direct term and surface waves in the spectral Green's function are in the form of $e^{-jk_{zi}|z|}/k_{zi}$, and can be calculated analytically. Therefore, they are excluded from the Green's function to be approximated.

$$\tilde{G} = \tilde{G}_0 + \tilde{G}_{sw} + \frac{1}{2jk_z} F_1 \quad (6.6)$$

The first two components in (6.6), \tilde{G}_0 and \tilde{G}_{sw} , are the effects of the direct term (or first quasi dynamic image) and surface waves. The last term, F_1 , is the left over spectral domain quantity that the quasi-dynamic part and surface waves part do not cover. Since the first two terms in (6.6), can be evaluated, F_1 is known. To use the Sommerfeld identity, the complex image method approximated this term, F_1 , with several complex images, images with complex amplitude and complex locations. In the simulated images technique, the approximation of the last term, F_1 , is done using simulated images which have complex amplitudes and fixed real locations, as is shown below,

$$F_1 = \sum_{i=1}^n a_i e^{-jb_i k_z} \quad (6.7)$$

where a_i , the amplitude of the images, are complex, and b_i , the location of quasi-dynamic images, are real numbers and known. To find a_i , we choose n points in k_z , plane and calculate both sides of (6.7) at each of these n points. Therefore, we will have n equations for a_i , $i = 1, \dots, n$. Solving this n equations with n unknowns, we can find a_i .

The surface wave contributions for thin layered structures are small, so the exclusion of the surface wave contribution is not critical for such geometries. Meanwhile, the extraction of the surface poles could improve the approximation for geometries with thick layers.

All the Green's functions in the spectral domain are functions of k_ρ (or k_z), except A_{zz} , given in Equation (6.4) and F_{zz} (See Appendix D). Therefore, the above approximation, (6.7), can be applied for all kinds of Green's functions except

A_{zx} and F_{zx} . The problem with these two functions is an extra parameter which is the wave number in \hat{x} , k_x . To handle these two cases, k_x is excluded from the approximation, and its effect is considered in the spatial domain (after obtaining the spatial domain representations of \tilde{A}_{zx}/k_x and \tilde{F}_{zx}/k_x) by differentiating analytically with respect to x .

The simulated image method is simpler than the complex images technique, because Prony's method is not employed (Prony's method is used to find two sets of complex unknowns in (6.7), a_i and b_i). We also require fewer sampling points and have fewer unknowns in comparison with the complex images technique. This makes our new method simpler and also faster.

In the simulated images technique, we have more freedom in choosing sampling points in the k_z plane. In complex images method, we have to choose specific points on k_z plane, because of Prony's method.

In comparison with the regular quasi-static image method, this new approach also simplifies the quasi-static or near field analysis. Instead of using tens of real images required by the quasi static method, we may use only a few, say three or four, simulated images.

6.4 Numerical Results

The closed form Green's function in the spatial domain using simulated images can be used for multilayered geometries having an arbitrary number of layers with arbitrary parameters and general (electric or magnetic, horizontal or vertical) sources. To verify the accuracy of our new simulated images method, in this section some numerical results of this method are compared with complex images or numerical

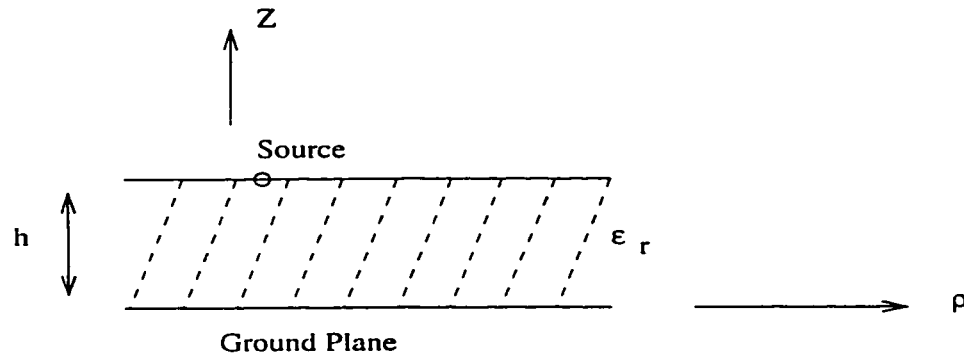


Figure 6.2: Microstrip structure.

integration.

In this section, this technique is used to calculate a few Green's functions for two structures. One is a simple microstrip structure, Figure 6.2, and the second one is a multilayer structure, Figure 6.7, with two dielectric layers on top of the ground plane.

6.4.1 Microstrip Structure

A microstrip structure is shown in Figure 6.2 with a dielectric height of 1 *mm* and dielectric constant $\epsilon_r = 12.6$. The spatial vector and scalar potential Green's functions, A_{xx} and Q_x , defined in (6.2) and (6.3) are calculated using simulated images. In this case four images are located at the position of the first four quasi-static images. The results are presented in Figure 6.3 and Figure 6.4. These two functions are also calculated using complex images method [33] and shown in Figure 6.3 and Figure 6.4. As we can see from the Figures, there is a very good agreement between the results of the simulated images technique and complex image method. However, the simulated images method is about 2 times faster.

The four simulated images are located at $b_i = -2ih$ where $h =$ substrate thick-

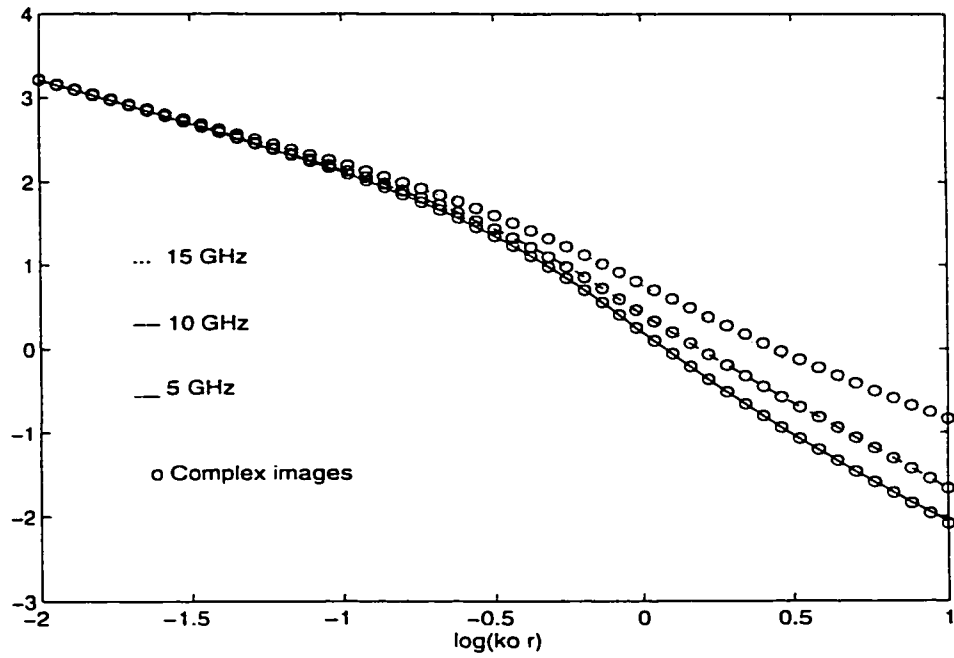


Figure 6.3: The amplitude of the vector potential A_{xx} .

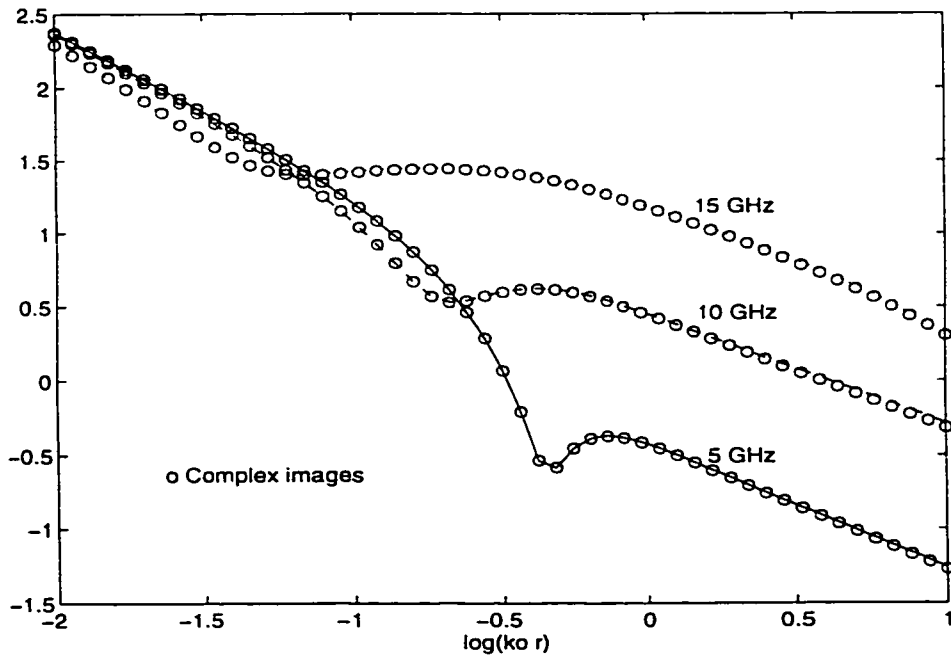


Figure 6.4: The amplitude of the scalar potential Q_x .

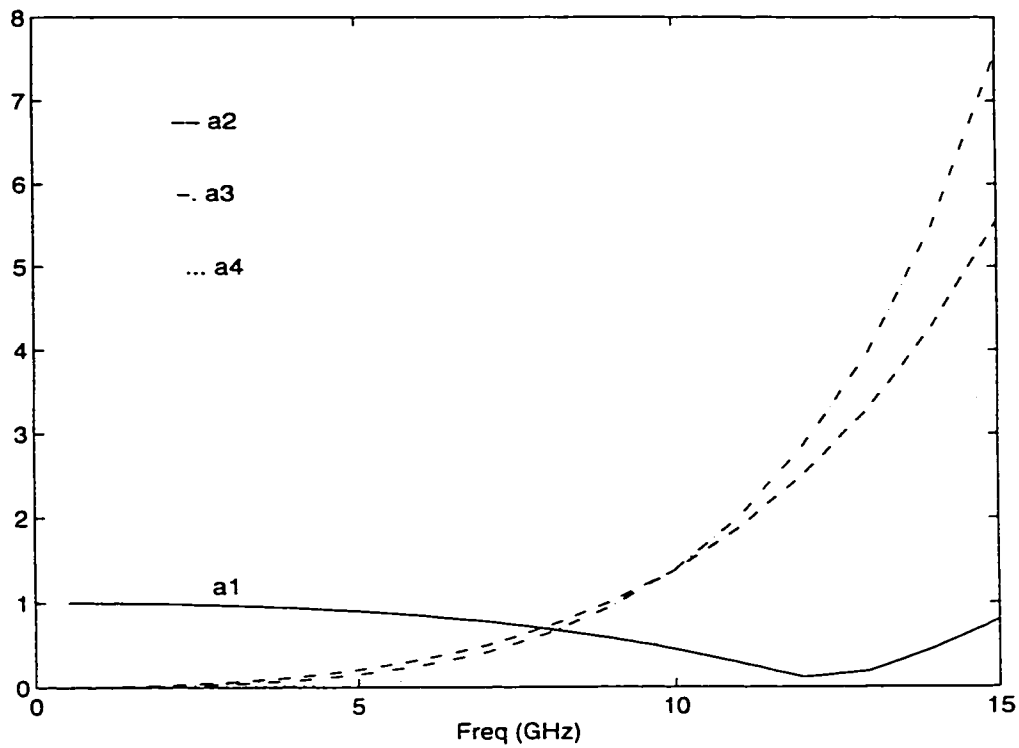


Figure 6.5: The amplitude of images for A_{xx} .

ness and $i = 1$ to 4. The amplitudes of the images are plotted in Figure 6.5 and Figure 6.6. They do not include the source or quasi-dynamic image at $z = 0$. Figures 6.5 and 6.6 show the variations of the amplitudes of the simulated images of the vector and scalar potentials, A_{xx} and Q_x .

It is observed that beyond 6.7 GHz, when the first simulated image is one electric radian from the source, the image amplitudes begin to vary with frequency. Below 6.7 GHz, the amplitudes of the simulated images are near constant but are not equal to those of the quasi-dynamic images. For good accuracy the quasi-dynamic images may number 80, for $\epsilon_r = 12.6$, instead of just the first four.

The advantage of slowly varying image amplitudes with frequency, Figures 6.5

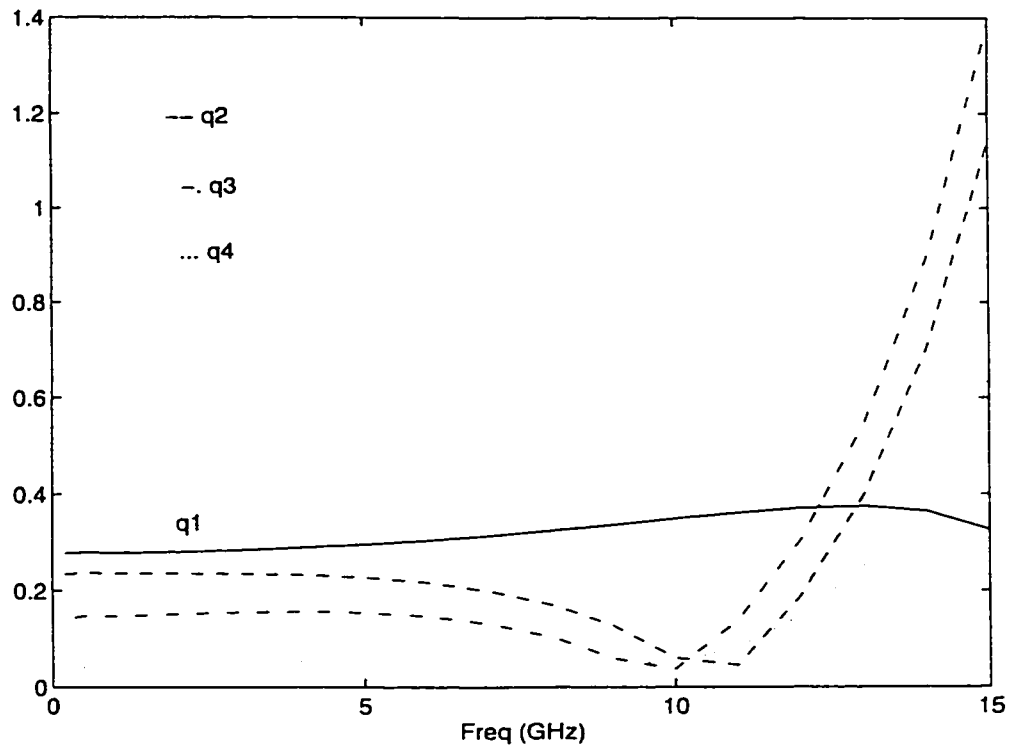


Figure 6.6: The amplitude of images for Q_x .

and 6.6, makes the simulated images a better choice for interpolation and rapid convergence in the analysis of many wide band (e.g. digital) applications. We can find the amplitude of these images at a few frequencies, and use a curve fitting to find an expression for image amplitudes as a function of frequency. Then the expression can be used over the frequency range to calculate the Green's functions.

6.4.2 Multilayer Structure

Another geometry which is investigated in this section consists of a substrate and a superstrate, and modeled as a 4-layer structure, the ground plane and air are considered as two layers. The parameters of the layers are: conductor (PEC), as a

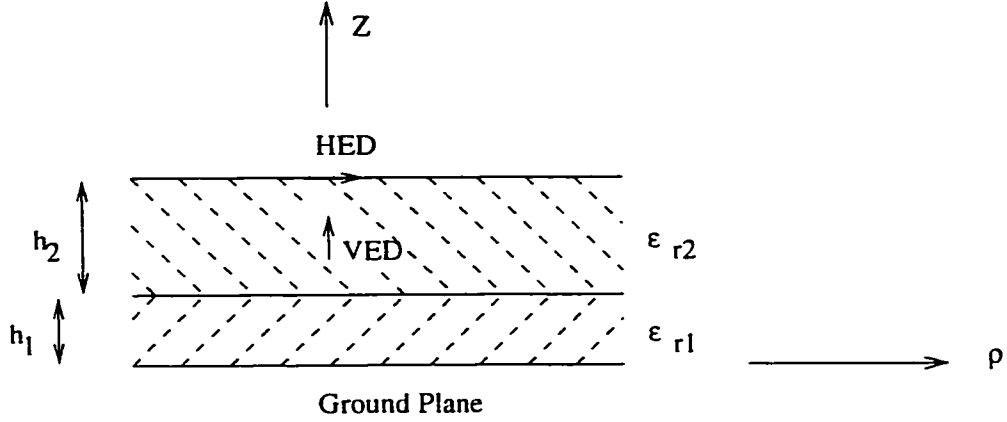


Figure 6.7: Geometry of structure with 2-layer dielectric.

first layer, $\epsilon_{r1} = 10$, $\epsilon_{r2} = 2$, $\epsilon_{r3} = 1$, $h_1 = 0.75 \text{ mm}$ and $h_2 = 1.5 \text{ mm}$ as shown in Figure 6.7.

Two dipoles are considered in this structure, and some of the Green's functions related to these two sources are calculated. The horizontal dipole (HED) is located at the air-dielectric interface, and the vertical dipole (VED) is located in the middle of the top layer ($h_2/2$). In all cases, the observation points are chosen at the source plane, which is the worst case as far as the convergence of the Green's functions are concerned.

For the VED in the structure, the A_{zx} Green's function is calculated. Figure 6.8 shows the magnitude of $\int A_{zx} dx$ with respect to the distance $k_o \rho$. In this figure, $\int A_{zx} dx$ is given instead of A_{zx} , because the approximation is performed on \tilde{A}_{zx}/k_x in the spectral domain, as explained. In this figure the results are shown for the simulated images technique and numerically evaluating the corresponding Sommerfeld integrals at a frequency of 1 GHz. As it is shown, the results of simulated images method is very accurate. The numerical calculation of the Green's function is very time consuming and difficult; however, the simulated images method is very

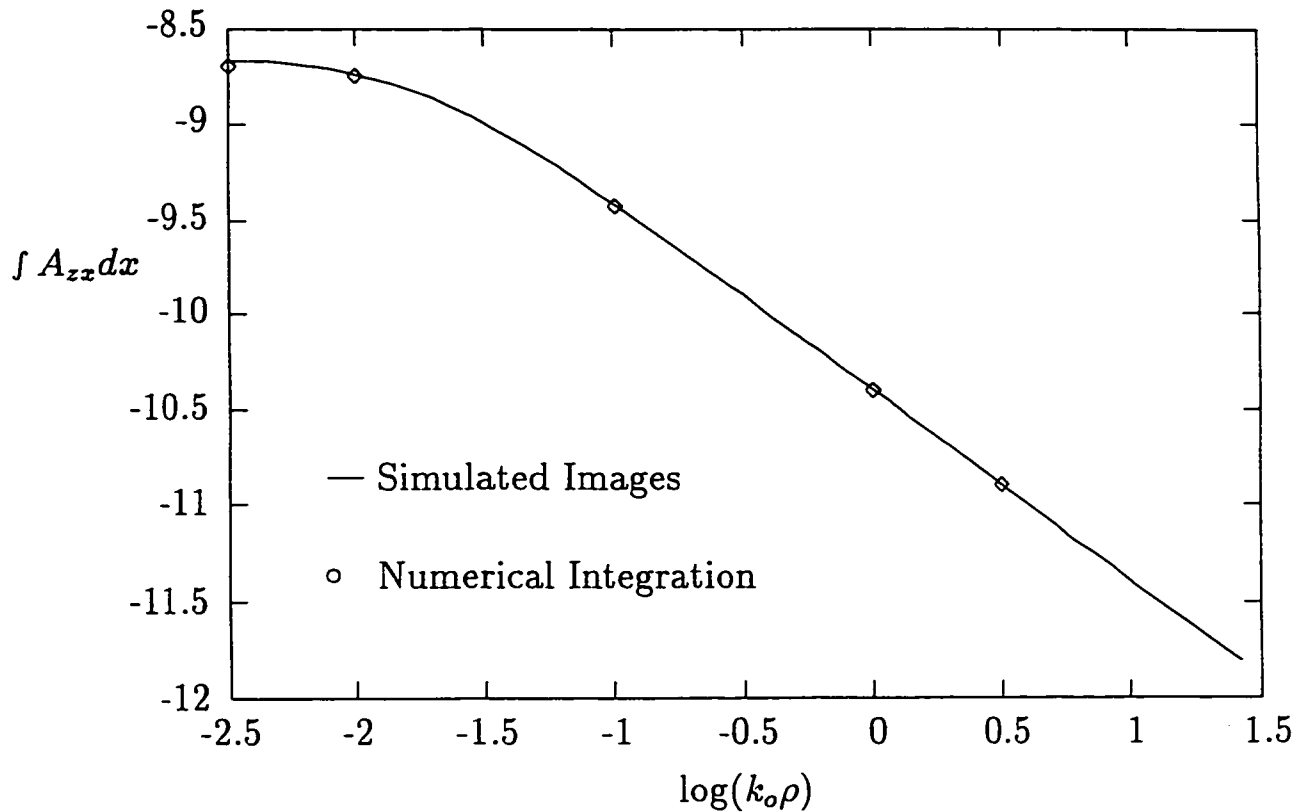


Figure 6.8: The amplitude of $\int A_{zx} dx$ for 2-layer dielectric structure.

simple and much faster. In terms of accuracy, our new method is very accurate, as we can see in Figure 6.8.

For the HED which is located at the air-dielectric interface of the structure, as usual the two most useful Green's function A_{xx} and Q_x are evaluated. Figures 6.9 and 6.10 show the magnitude of A_{xx} and Q_x , respectively. In these figures the results are shown for the simulated images technique and complex images method at two frequencies of 1 and 5 GHz. As we can see, there is a good agreement between two methods, and the accuracy of the simulated images method is the same as complex image method. However, the simulated images method is simpler and faster.

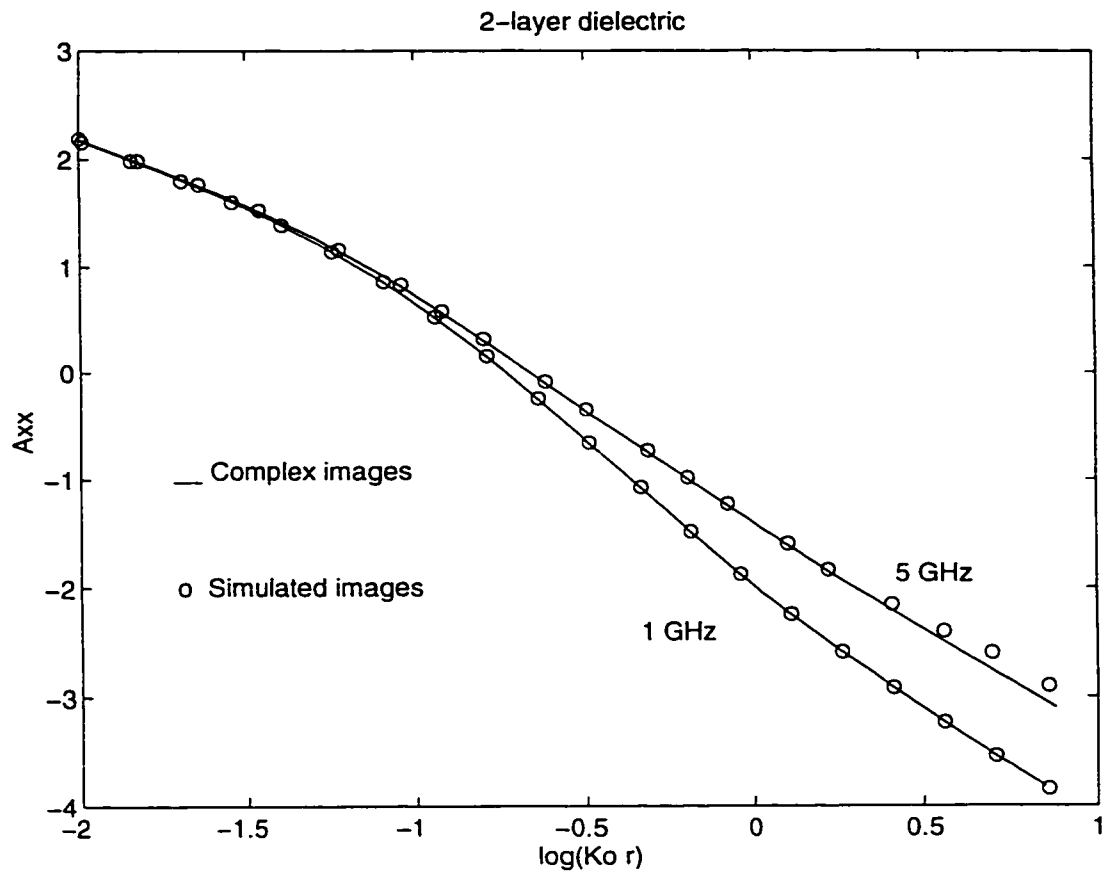


Figure 6.9: The amplitude A_{xx} for 2-layer dielectric structure.

In this section a few examples were shown to illustrate the accuracy of the new developed simulated images. Other Green's functions of a multilayer structures can also be evaluated with this simple method. Other Green's functions are not presented in this thesis, because the calculation of Green's functions was a minor area in this research.

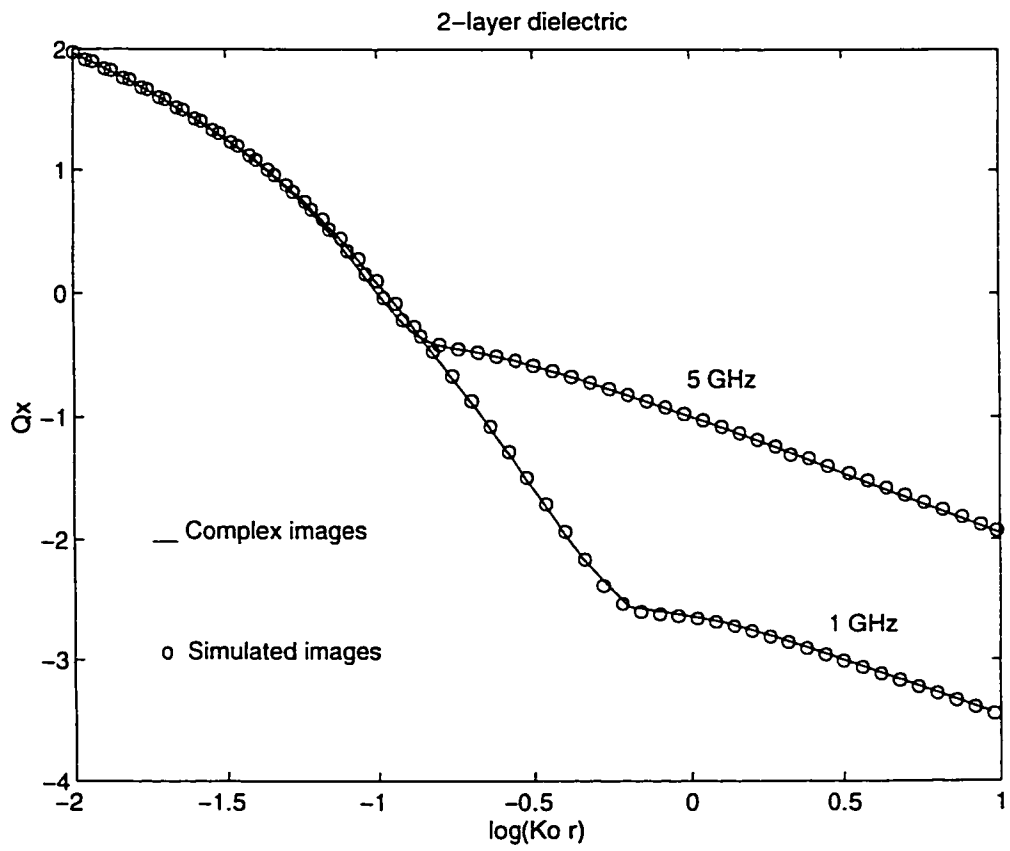


Figure 6.10: The amplitude Q_x for 2-layer dielectric structure.

Chapter 7

Conclusion and Future Work

7.1 Conclusion

A new method has been developed to analyze high Q planar patch filters. The proposed method is a hybrid method which is a combination of the two-dimension (2D) methods (modal or contour integral) and the numerical moment method using three-dimension (3D) Green's functions of multilayer structures. We start with a 2D method, and analyze the patch filter ignoring fringing fields, considering a magnetic wall around the patch. This model of 2D patch, comprising of electric current on the patch and magnetic current around the patch on the wall, can be viewed as a 3D structure, i.e. cavity with a magnetic wall. The magnetic wall is then removed to consider the fringing fields at the edge of the patch. This correction term is formulated in terms of a line integral only around the patch, on the edge.

This new method has the following two main advantages. First, it is fast compared with regular numerical methods, such as integral equation-moment method. Basically, there are two steps in this method. The first is a 2D method, followed

by a correction term using 3D Green's functions. Both of these two steps are fast, because a 2D method is either using an analytical expression (in modal method) or applying a line integral (in contour integral method), and the correction term is a double line integral on the edge of patch, that is much faster than double surface integrals in the regular moment method. Our new method is also faster than the multiport network method (segmentation or desegmentation methods). The later method needs matrix inversion, and for better accuracy it would be time consuming if the number of ports is large.

The second advantage of this method is accuracy which is necessary in analyzing high Q patch filters. In this method accuracy was not sacrificed for speed. The 2D method, as a first step, is accurate for the structure with magnetic wall (no fringe field). The edge effect, fringing field, is taken into account using a variational expression by removing the magnetic wall. Since this expression is variational, and we use the result of 2D analysis in this variational expression, the correction term would also be accurate. On the other hand this correction term is relatively small and we can afford to have larger relative error.

Most high Q circuits have gap coupling to reduce the load effect on Q . In this work, a model is presented for the gap structure in patch filters with gap coupling. This model of the gap is used with our hybrid method to analyze the whole circuit. The gap is formed between a strip and the patch. This structure can be considered as a transmission line. Therefore, the impedance of the gap is the impedance of transmission line stubs. The parameters of this transmission line are found using conformal mapping. The advantage of this model for the gap is its simplicity and speed. In our analysis, we increased the length of the strip to include the fringing field effect. In regular numerical methods, such as the moment method, a huge number of segments should be used for accurate results, and this

makes the moment method very time consuming. However, very fine segmentation may reduce the accuracy of moment method, because of ill condition of matrix coefficient

High order patch filters use more than one patch element. In this research the coupling between patches is investigated. Extending the same method for one patch element filter, hybrid method, we could consider the coupling between two patches. To calculate the coupling between patches, we found a double line integral which should be performed around the edges of patches. The new method, developed in this thesis, makes the analysis very fast. In the moment method, coupling between patches was performed using a double surface integral on the surface of the patches, and this makes the moment method very slow. Our method is accurate and fast in analyzing a structure with more than one patch element or having large metallic area.

In this work, we need to calculate the Green's function of multilayer structures. The complex image method which was developed at the University of Waterloo by Prof. Y.L.Chow, was simplified to a new method called *simulated images method*. This new method approximates the Green's function by images located at the fixed real locations which are the locations of quasi-static images but with complex amplitude. The simulated images method is simpler and faster than the old method, and has the same accuracy.

7.2 Future Work

In order to improve some parts of this work and as a continuation of the present approach, the following topics of research could be considered for future work.

i- To reduce the radiation loss, most of the microwave filters are enclosed by a box, specially high Q filters. To analysis a circuit in a box, we have to use proper Green's functions. In this work, to simulate a structure in a box, we used Green's functions of a multilayer structure and deleted the real part (radiation) of the Z-parameters. This is not accurate enough for all the cases, because the effect of the side walls of the box is not considered. As an important future step, the Green's function of multilayer structure in a box should be developed, and used with our new presented method. There are some works by Dr. Faraji-Dana and Prof. Y.L. Chow in formulation of Geen's function of multilayer structure in a box [63], and we can make use of those works.

ii- In analyzing the gap structure, Chapter 4, to calculate the parameter of the transmission line between strip and half plane, we ignored the effect of the ground plane, when the strip is narrow. For gap structures with large strip ($s \geq h/4$), our approximation is not good, and we have to include the effect of the ground plane. As mentioned in Chapter 4, for more accurate analysis quasi-dynamic images should be considered in the analysis.

iii- In Chapter 4, to calculate the impedance of the gap, an open stub model has been used. To include the fringing fields at the end of the open stub, we just increased the length of stub by 5%. To improve the accuracy of the analysis, a more accurate model should be found for this structure.

iv- With the presented method, we can analyze structures with more patches and gap couplings. Examples of these high Q circuits are 2-pole Chebyshev filters, or 3-pole split resonators [64] used in high power high temperature superconductors planar filter designed by Dr. Mansour's research group at ComDev. These structures could be analyzed using our method.

v- The accuracy and speed of our method should enable us to make many iterative computations, within a limited time, of the analysis for the synthesis and optimization of high order filter. As the next step of this work, our method can be used in an optimization algorithm to design (high Q) patch filters.

Appendix A

Expansion of Green's Function by Eigenfunctions

In Section 2.2, when a 2D modal analysis was presented, we used the expansion of Green's function by eigenfunctions, Equation (2.18). In this appendix, this relationship is derived in detail.

The wave equation for the structure is given as follow, with the Neumann type boundary condition given in Equation (2.3),

$$(\nabla_t^2 + k^2)V = 0 \tag{A.1}$$

Let the eigenvalues and eigenfunctions of the above wave equation be denoted by k_n and ϕ_n , respectively. As we know, any function satisfying (A.1) can be expanded by a set of ϕ_n . Therefore, The Green's function $G(x, y|x_0, y_0)$ can be expressed as

$$G(x, y|x_0, y_0) = \sum_n A_n \phi_n \tag{A.2}$$

The remaining problem is how to compute the coefficients A_n .

As a preliminary step, we show first that G satisfies a differential equation

$$(\nabla^2 + k^2)G = -j\omega\mu h \delta(x - x_0)\delta(y - y_0) \quad (\text{A.3})$$

where δ denotes a delta function. To prove the above equation, we integrate this after multiplying both sides by the fictitious injection current $i(x_0, y_0)$. Then we obtain from the left hand side

$$\int \int (\nabla^2 + k^2)G(x, y|x_0, y_0) i(x_0, y_0) dx_0 dy_0 = (\nabla^2 + k^2)V(x, y) \quad (\text{A.4})$$

and from the right hand side

$$-j\omega\mu h \int \int i(x_0, y_0) \delta(x - x_0)\delta(y - y_0) dx_0 dy_0 = -j\omega\mu h i(x, y) \quad (\text{A.5})$$

Therefore, (A.2) can be proved if we can show that, with the presence of fictitious current $i(x_0, y_0)$, $(\nabla^2 + k^2)V = 0$ would become

$$(\nabla^2 + k^2)V = -j\omega\mu h i(x, y) \quad (\text{A.6})$$

This equation can easily be proved if we rewrite Maxwell's equation in (2.1), and add $-i(x, y)$ to the displacement current density $j\omega\epsilon E_z$, as

$$\frac{\partial H_y}{\partial x} - \frac{\partial H_x}{\partial y} = j\omega\epsilon E_z - i(x, y) \quad (\text{A.7})$$

and modify the computation performed to derive (2.4) from (2.1). Similar to (2.4), the Equation in (A.3) can be proved [9].

Next we substitute (A.2) into (A.3) and use $(\nabla^2 + k_n^2)\phi_n = 0$ to obtain

$$\sum_n A_n(k^2 - k_n^2)\phi_n = -j\omega\mu h \delta(x - x_0)\delta(y - y_0) \quad (\text{A.8})$$

*APPENDIX A. EXPANSION OF GREEN'S FUNCTION BY EIGENFUNCTIONS*114

We multiply both sides of the above equation by ϕ_m , integrate both sides in the region D , and finally use the ortho-normalizing condition. Then, the Green's function can be derived given in terms of the eigenfunctions as [9]

$$G(x, y|x_0, y_0) = j\omega\mu h \sum_n \frac{\Phi_n(x_0, y_0)\Phi_n(x, y)}{k_n^2 - k^2} \quad (\text{A.9})$$

Appendix B

Weber's Solution Using Cylindrical Waves

The Green's theorem expressed in cylindrical coordinates and Weber's solution for cylindrical waves are used to convert the two dimensional wave equation into a contour integral [9].

This approach proceeds by considering the two functions ν and ω , which satisfy

$$(\nabla_t^2 + k^2)v = 0 \quad (\text{B.1})$$

in D , where D is a two dimensional region inside a contour C as shown in Figure 2.5, and v stands for ν and ω . Setting $\nu = v$ and $\omega = H_0^{(2)}(kr)$, zeroth-order Hankel function of the second kind, into Green's theorem, which is

$$\int_C \left(\nu \frac{\partial \omega}{\partial n} - \omega \frac{\partial \nu}{\partial n} \right) ds_0 = \int \int_D (\nu \nabla^2 \omega - \omega \nabla^2 \nu) ds = 0 \quad (\text{B.2})$$

we obtain

$$\int_C \left(v(s_0) \frac{\partial H_0^{(2)}(kr)}{\partial n} - H_0^{(2)}(kr) \frac{\partial v}{\partial n} \right) ds_0 = 0 \quad (\text{B.3})$$

when the point P is located outside the contour C. If point P is inside the contour C, p becomes a singular point for ω , and the area integral in (B.2) does not vanish. Applying Green's theorem to the region that excludes the singular point, we get

$$\int_C [v(s_0) \frac{\partial H_0^{(2)}(kr)}{\partial n} - H_0^{(2)}(kr) \frac{\partial v}{\partial n}] ds_0 = \int_{C_1} [v(s_0) \frac{\partial H_0^{(2)}(kr)}{\partial n} - H_0^{(2)}(kr) \frac{\partial v}{\partial n}] ds_0 \quad (\text{B.4})$$

where C_1 stands for the contour surrounding the excluded small circular area whose radius is chosen to be δ . Here, we have also used $\partial n = -\partial r$ on C_1 . When $H_0^{(2)}(kr)$ is replaced by its small argument expression, which holds for $kr < 1$, and when v and $\partial v/\partial n$ are taken to be constant on C_1 , the right-hand side of (B.4) can be written as

$$\int_{C_1} [-\frac{2j}{\pi r} v(s_0) + (\frac{2j}{\pi} \ln \frac{kr}{2}) \frac{\partial v}{\partial n}] ds_0 = -4jv(s) + 4j\delta \ln \frac{k\delta}{2} \frac{\partial v}{\partial n} \quad (\text{B.5})$$

when the term δ tends to zero, the second term on the right-hand side of (B.5) vanishes. Thus for a point inside the contour C we obtain

$$4jv(s) = \int_C [H_0^{(2)}(kr) \frac{\partial v}{\partial n} - v(s_0) \frac{\partial H_0^{(2)}(kr)}{\partial n}] ds_0 \quad (\text{B.6})$$

This equation gives the potential at point P in the region D in terms of v and $\partial v/\partial n$ along the contour C that surrounds D.

When the point P is on the contour C, the right-hand side of (B.6) is reduced by a factor 2 and may be written as

$$v(s) = \frac{1}{2j} \int_C [H_0^{(2)}(kr) \frac{\partial v}{\partial n} - v(s_0) \frac{\partial H_0^{(2)}(kr)}{\partial n}] ds_0 \quad (\text{B.7})$$

Combining the above equation with

$$\frac{\partial v}{\partial n} = j\omega\mu h J_n \quad (\text{B.8})$$

which is used in (2.9), and

$$\frac{\partial H_0^{(2)}(kr)}{\partial n} = -k \cos \Theta H_0^{(1)}(kr) \quad (\text{B.9})$$

therefore, we obtain

$$v(s) = \frac{1}{2j} \oint [k \cos \Theta H_1^{(2)}(kr)V(s_0) + j\omega\mu h H_0^{(2)}(kr)J_n(s_0)] ds_0 \quad (\text{B.10})$$

Appendix C

2D Green's Functions of Regular Patches

As mentioned in Section 2.2 , the Green's function of simple shaped patches can be found using an eigenfunction, modal, expansion. In our proposed method for analyzing patch filters, Chapter 3, a 2D modal method should be used. If we have a simple patch, we may use the modal method. Therefore, in this Appendix, the Green's function of simple patches is briefly listed [20]. As an example of Z matrix using 2D Green's function, the Z matrix of a rectangular patch is also driven.

In this section, the height of substrate is h with dielectric of permittivity ϵ . In the expressions that follow, σ_i is given by

$$\sigma_i = \begin{cases} 1 & i = 0 \\ 2 & i \neq 0 \end{cases}$$

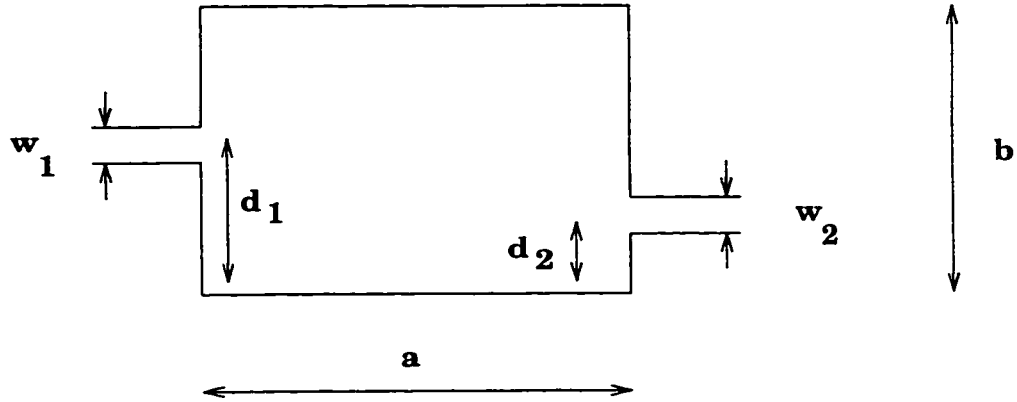


Figure C.1: Two port rectangular patch filter

C.1 Rectangular Patch

The Green's function for a rectangular circuit having dimensions $a \times b$ as shown in Figure C.1, is

$$G(x, y | x_o, y_o) = \frac{j\omega\mu h}{ab} \sum_{m=0}^{\infty} \sum_{n=0}^{\infty} \frac{\sigma_m \sigma_n}{k_x^2 + k_y^2 - k^2} \cos(k_x x_o) \cos(k_y y_o) \cos(k_x x) \cos(k_y y) \quad (\text{C.1})$$

where

$$k_x = m\pi/a \quad , \quad k_y = n\pi/b$$

C.1.1 Z-matrix of a Rectangular Patch

The Z-matrix of a rectangular patch shown in Figure C.1, using (2.17) and (C.1), can be written as

$$Z_{ii} = \frac{j\omega\mu h w_i}{ab} \sum_{m=0}^{\infty} \sum_{n=0}^{\infty} \frac{\sigma_m^2 \sigma_n^2}{k_x^2 + k_y^2 - k^2} f_{ni}^2 \quad , \quad i = 1, 2 \quad (\text{C.2})$$

and

$$Z_{12} = Z_{21} = \frac{j\omega\mu h\sqrt{w_1 w_2}}{ab} \sum_{m=0}^{\infty} \sum_{n=0}^{\infty} (-1)^m \frac{\sigma_m^2 \sigma_n^2}{k_x^2 + k_y^2 - k^2} f_{n1} f_{n2} \quad (\text{C.3})$$

where

$$f_{ni} = \begin{cases} \cos(k_y d_i) \frac{\sin(k_y w_i/2)}{k_y (w_i/2)} & n \neq 0 \\ 1 & n = 0 \end{cases}$$

C.2 Circular Patch

For the circular patch with radius a , shown in Figure C.2a, the 2D Green's function can be derived as,

$$G(\rho, \phi | \rho_o, \phi_o) = \frac{h}{j\omega\epsilon\pi a^2} + j\omega\mu h \sum_{m=1}^{\infty} \sum_{n=0}^{\infty} \frac{\sigma_n J_n(k_{mn}\rho) J_n(k_{mn}\rho_o) \cos[n(\phi - \phi_o)]}{\pi(a^2 - n^2/k_{mn}^2)(k_{mn}^2 - k^2) J_n^2(k_{mn}a)} \quad (\text{C.4})$$

where J_n is Bessel's function of the n th order, and k_{mn} satisfy

$$\frac{\partial}{\partial \rho} J_n(k_{mn}\rho) |_{\rho=a} = 0 \quad (\text{C.5})$$

The subscript m in k_{mn} represents the m th root of (C.5).

C.3 Annular Ring

An annular ring patch with radius a and b , $a < b$ is shown in Figure C.2b. The 2D Green's function for this structure is

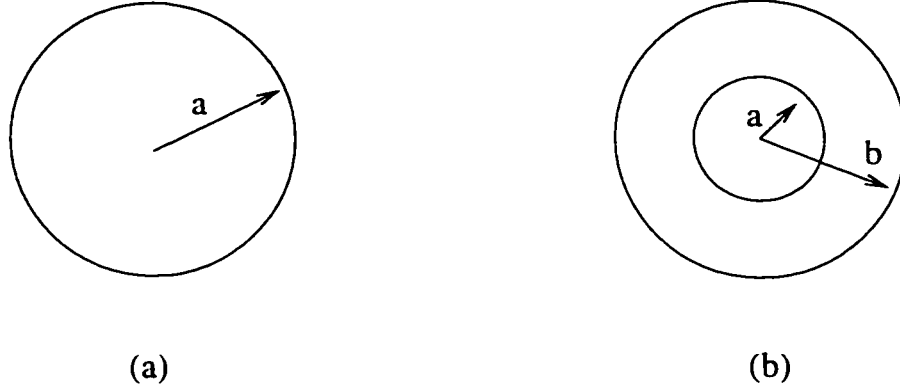


Figure C.2: (a) Circular Patch (b) Annular Ring

$$G(\rho, \phi | \rho_o, \phi_o) = \frac{h}{j\omega\epsilon\pi(b^2 - a^2)} + \quad (C.6)$$

$$j\omega\mu h \sum_{m=1}^{\infty} \sum_{n=0}^{\infty} \frac{\sigma_n F_{mn}(\rho) F_{mn}(\rho_o) \cos[n(\phi - \phi_o)]}{\pi[(b^2 - n^2/k_{mn}^2)F_{mn}^2(b) - (a^2 - n^2/k_{mn}^2)F_{mn}^2(a)](k_{mn}^2 - k^2)}$$

where

$$F_{mn}(\rho) = N'_n(k_{mn}a)J_n(k_{mn}\rho) - J'_n(k_{mn}a)N_n(k_{mn}\rho) \quad (C.7)$$

and k_{mn} are solutions of

$$\frac{J'_n(k_{mn}a)}{N'_n(k_{mn}a)} = \frac{J'_n(k_{mn}b)}{N'_n(k_{mn}b)} \quad (C.8)$$

In the above relations N_n is Neumann's function of order n and J'_n and N'_n are first derivatives with respect to the arguments.

C.4 Circular Sector

A circular sector with radius a and sector angle α is shown in Figure C.3a. The 2D Green's for this structure can be derived only if the sector angle α takes on certain discrete values which is π/p and p is an integer.



Figure C.3: (a)Circular Sector (b)Annular Sector

$$G(\rho, \phi | \rho_o, \phi_o) = \frac{2ph}{j\omega\epsilon\pi a^2} + \quad (C.9)$$

$$2jp\omega\mu h \sum_{m=1}^{\infty} \sum_{n=0}^{\infty} \frac{\sigma_m \sigma_n J_{n_i}(k_{mn_i} \rho_o) J_{n_i}(k_{mn_i} \rho) \cos(n_i \phi_o) \cos(n_i \phi)}{\pi [a^2 - n_i^2 / k_{mn_i}^2] (k_{mn_i}^2 - k^2) J_{n_i}^2(k_{mn_i} a)}$$

where $n_i = np$ and k_{mn_i} is given by

$$\frac{\partial}{\partial \rho} J_n(k_{mn} \rho) |_{\rho=a} = 0 \quad (C.10)$$

C.5 Annular Sector

An annular sector patch is shown in Figure C.3b. Similar to a circular sector patch, the 2D Green's function can be derived only for $\alpha = \pi/p$.

$$G(\rho, \phi | \rho_o, \phi_o) = \frac{2ph}{j\omega\epsilon\pi(b^2 - a^2)} + \quad (C.11)$$

$$jp\omega\mu h \sum_{m=1}^{\infty} \sum_{n=0}^{\infty} \frac{\sigma_n F_{mn_i}(\rho) F_{mn_i}(\rho_o) (\cos(n_i \phi) - \cos(n_i \phi_o))}{\pi [(b^2 - n_i^2 / k_{mn_i}^2) F_{mn_i}^2(b) - (a^2 - n_i^2 / k_{mn_i}^2) F_{mn_i}^2(a)] (k_{mn_i}^2 - k^2)}$$

where $n_i = np$ and F_{mn_i} is defined in (C.7). The values of k_{mn_i} are obtained from (C.8).

C.6 Equilateral Triangle

An equilateral patch is shown in Figure C.4a. The 2D Green's function is

$$G(x, y | x_o, y_o) = 4j\omega\mu h \sum_{m=-\infty}^{\infty} \sum_{n=-\infty}^{\infty} \frac{T_1(x_o, y_o)T(x, y) + T_2(x_o, y_o)T_2(x, y)}{16\sqrt{3}\pi^2(m^2 + mn + n^2) - 9\sqrt{(3)a^2k^2}} \quad (\text{C.12})$$

where

$$\begin{aligned} T_1(x, y) = & (-1)^l \cos\left(\frac{2\pi lx}{\sqrt{3}a}\right) \cos\left(\frac{2\pi(m-n)y}{3a}\right) \\ & + (-1)^m \cos\left(\frac{2\pi mx}{\sqrt{3}a}\right) \cos\left(\frac{2\pi(n-l)y}{3a}\right) + (-1)^n \cos\left(\frac{2\pi nx}{\sqrt{3}a}\right) \cos\left(\frac{2\pi(l-m)y}{3a}\right) \end{aligned} \quad (\text{C.13})$$

and

$$\begin{aligned} T_2(x, y) = & (-1)^l \sin\left(\frac{2\pi lx}{\sqrt{3}a}\right) \sin\left(\frac{2\pi(m-n)y}{3a}\right) \\ & + (-1)^m \sin\left(\frac{2\pi mx}{\sqrt{3}a}\right) \sin\left(\frac{2\pi(n-l)y}{3a}\right) + (-1)^n \sin\left(\frac{2\pi nx}{\sqrt{3}a}\right) \sin\left(\frac{2\pi(l-m)y}{3a}\right) \end{aligned} \quad (\text{C.14})$$

and $l = -(m + n)$.

C.7 Right-Angled Isosceles Triangle

The 2D Green's function for the right angled isosceles triangle shown in Figure C.4b is given as

$$G(\rho, \phi) = \frac{j\omega\mu h}{2} \sum_{m=0}^{\infty} \sum_{n=0}^{\infty} \frac{\sigma_m \sigma_n T(x, y) T(x_o, y_o)}{(m^2 + n^2)\pi^2 - a^2k^2} \quad (\text{C.15})$$

where

$$T(x, y) = \cos \frac{m\pi x}{a} \cos \frac{n\pi y}{a} + (-1)^{(m+n)} \cos \frac{n\pi x}{a} \cos \frac{m\pi y}{a}$$

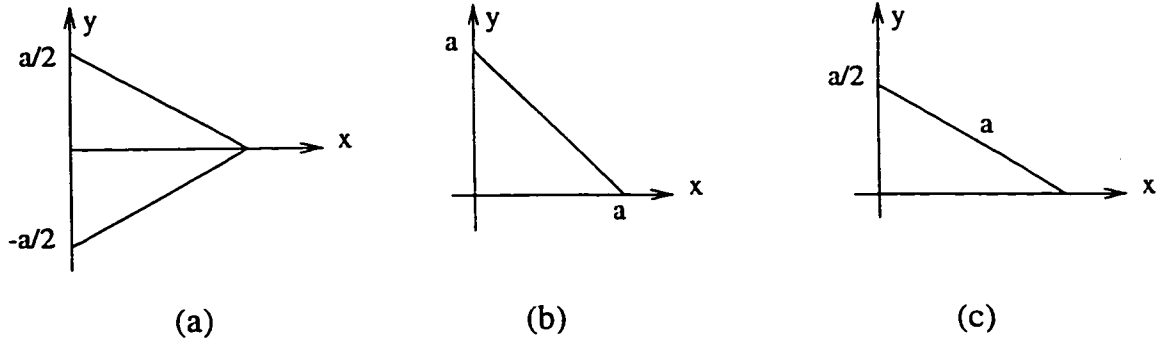


Figure C.4: Triangle patches, (a)Equilateral (b)Right-angled isosceles (c)30° – 60° right-angled

C.8 30° – 60° Right-Angled Triangle

A patch with 30° – 60° right-angled triangle shape is shown in Figure C.4c. The 2D Green's function for the structure is as follow,

$$G(x, y|x_o, y_o) = 8j\omega\mu h \sum_{m=-\infty}^{\infty} \sum_{n=-\infty}^{\infty} \frac{T_1(x_o, y_o)T_1(x, y)}{16\sqrt{3}\pi^2(m^2 + mn + n^2) - 9\sqrt{3}a^2k^2} \quad (C.16)$$

where $T_1(x, y)$ is defined in (C.14).

Appendix D

Green's Functions

One method of defining Green's functions for electric or magnetic fields is Green's function of scalar and vector potentials. The relations between fields and potentials are as follow,

$$\vec{E} = -\nabla \times \vec{F} \quad (\text{D.1})$$

$$\vec{H} = \nabla \times \vec{A} \quad (\text{D.2})$$

$$\hat{s} \cdot (\nabla_s \Phi_q^m) = -\nabla \cdot \vec{F} \quad (\text{D.3})$$

$$\hat{s} \cdot (\nabla_s \Phi_q^e) = -\nabla \cdot \vec{A} \quad (\text{D.4})$$

Where \vec{E} and \vec{H} are electric and magnetic fields, respectively. \vec{A} and \vec{F} are electric and magnetic vector potentials, Φ_q^e and Φ_q^m are electric and magnetic scalar potentials.

In multilayer structures, and in spectral domain (k_x and k_y), vector and scalar potentials can be written as follow,

$$\bar{A}_{xx} = \frac{1}{2jk_{zs}} \frac{\mu_s}{\mu_f} T_{TE}^H \quad (D.5)$$

$$\bar{A}_{zx} = \frac{-k_x}{2jk_{zs}} \frac{\mu_s}{\mu_f k_\rho} \left(\frac{\mu_f k_{zs}}{\mu_s} T_{TM}^H - j \frac{\partial T_{TE}^H}{\partial z_f} \right) \quad (D.6)$$

$$\bar{\Phi}_x^{qe} = \frac{1}{2jk_{zs} k_\rho^2} \left(\frac{\mu_s k_f^2}{\mu_f} T_{TE}^H - j k_{zs} \frac{\partial T_{TM}^H}{\partial z_f} \right) \quad (D.7)$$

$$\bar{A}_{zz} = \frac{1}{2jk_{zs}} T_{TM}^V \quad (D.8)$$

$$\bar{\Phi}_z^{qe} = \frac{1}{2jk_{zs}^3} \frac{\partial^2 T_{TM}^V}{\partial z_s \partial z_f} \quad (D.9)$$

$$\bar{F}_{xx} = \frac{1}{2jk_{zs}} \frac{\epsilon_s}{\epsilon_f} T_{TM}^T \quad (D.10)$$

$$\bar{F}_{zx} = \frac{-k_x}{2jk_{zs} k_\rho} \left(k_{zs} T_{TE}^V - j \frac{\epsilon_s}{\epsilon_f} \frac{\partial T_{TM}^V}{\partial z_f} \right) \quad (D.11)$$

$$\bar{\Phi}_z^{qm} = \frac{1}{2jk_{zs} k_\rho^2} \left(\frac{\epsilon_s k_f^2}{\epsilon_f} T_{TM}^V - j k_{zs} \frac{\partial T_{TE}^V}{\partial z_f} \right) \quad (D.12)$$

$$\bar{F}_{zz} = \frac{1}{2jk_{zs}} T_{TE}^H \quad (D.13)$$

$$\bar{\Phi}_z^{qm} = \frac{1}{2jk_{z_s}^3} \frac{\partial^2 T_{TE}^H}{\partial z_s \partial z_f} \quad (\text{D.14})$$

where T^{TE} and T^{TM} are the transmission coefficients from the source plane, z_s , to field plane, z_f , and k_{z_f} and k_{z_s} are wavenumbers in two planes, field and source planes. We also have,

$$k_\rho^2 = k_x^2 + k_y^2 \quad (\text{D.15})$$

$$k_{z_s} = \pm \sqrt{\epsilon_s k_o^2 - k_\rho^2} \quad (\text{D.16})$$

where k_o is the wave number in free space, and the imaginary part of k_{z_s} is always negative.

Bibliography

- [1] G.C. Liang et al. “High Power HTS Microstrip Filters for Cellular Base Station Applications”. *IEEE Trans. on Applied Superconductivity*, 5(2):2062–2056, June 1995.
- [2] W.P. Harokopus et al. “Surface wave excitation from Open Microstrip Discontinuities”. *IEEE Trans. on Microwave Theory and Techniques*, 39(7):1098–1107, July 1991.
- [3] G.L. Matthaei and G.L. Hey-Shipton. “Concerning the Use of High-Temperature Superconductivity in Planar Microwave Filters”. *IEEE Trans. on Microwave Theory and Techniques*, 42(7):1287–1293, July 1994.
- [4] Tatsuo Itoh. “*Numerical Techniques for Microwave and Millimeter-wave Passive Structures*”. J. Wiley, 1989.
- [5] G. Mur. “Finite difference method for the solution of electromagnetic wave guide discontinuity problem”. *IEEE Trans. on Microwave Theory and Techniques*, 22(1):54–57, Jan 1974.
- [6] P. Silvester. “Finite Element Analysis of planar microwave networks”. *IEEE Trans. on Microwave Theory and Techniques*, 21(2):104–108, Feb. 1973.

- [7] Y.C. Shih and W.J.R. Hofer. "Dominant and second order cutoff frequencies in fin lines with two dimensional TLM". *IEEE Trans. on Microwave Theory and Techniques*, 28(12):1443–1448, Dec. 1980.
- [8] J.R. Mosig. "Arbitrarily Shaped Microstrip Structures and Their Analysis with a Mixed Potential Integral Equation". *IEEE Trans. on Microwave Theory and Techniques*, 36(2):314–324, Feb. 1988.
- [9] "K.C. Gupta and M.D. Abouzahra". "Planar Circuits analysis". In T. Itoh, editor, *Numerical Techniques for Microwave and Millimeter-wave Passive Structures*, chapter 4, pages 214–333. J. Wiley, 1989.
- [10] R. Chadha and K.C. Gupta. "Green's Functions for Triangular Segments in Planar Microwave Circuits". *IEEE Trans. on Microwave Theory and Techniques*, 28(10):1139–1143, Oct. 1980.
- [11] R. Chadha and K.C. Gupta. "Green's Functions for Circular Sectors, Annular Rings and Annular Sectors in Planar Microwave Circuits". *IEEE Trans. on Microwave Theory and Techniques*, 29(1):68–71, Jan. 1981.
- [12] T. Okoshi. *Planar Circuits For Microwaves and Lightwaves*. Springer-Verlag, New York, 1985.
- [13] J. Helszjan and D.S. James. "Planar Triangular Resonators with Magnetic Walls". *IEEE Trans. on Microwave Theory and Techniques*, 26(2):95–100, Feb. 1978.
- [14] R.F. Harrington. *Field Computation by Moment Method*. Macmillan Company, New York, 1968, pp 25-31 and 62-68.

- [15] G.S. Hilton, C.J. Railton, and M.A. Beach. "Modelling parasitically coupled patch antenna using the FDTD technique". *IEE-Eighth International Conference on Antenna and Propagation*, 1:186–189, March 1993.
- [16] D.M.Sheen, S.M.Ali, M.D.Abouzahra, and J.A.Kong. "Application of the Three-Dimensional Finite-Difference Time-Domain Method to the Analysis of Planar Microstrip Circuits". *IEEE Trans. on Microwave Theory and Techniques*, 38(7):849–857, July 1990.
- [17] T. Okoshi and T. Miyoshi. "The Planar Circuit - An Approach to Microwave Integrated Circuitry". *IEEE Trans. on Microwave Theory and Techniques*, 20:245–252, 1972.
- [18] T.M. Martinson and E.F. Kuester. "Accurate Analysis of Arbitrarily Shaped Patches Resonators on Thin Substrates". *IEEE Trans. on Microwave Theory and Techniques*, 36(2):324–331, Feb. 1988.
- [19] G.G. Gentili and G. Macchiarella. "Efficient Analysis of Planar Circulators by New Boundary Integral Technique". *IEEE Trans. on Microwave Theory and Techniques*, 42(3):489–493, March 1994.
- [20] K.C. Gupta, R. Garg and R. Chadha. "*Computer Aided Design of Microwave circuits*". Artech House, 1981, pp. 353 - 368.
- [21] P.C. Sharma and K.C. Gupta. "Desegmentation method for analysis of two-dimensional microwave circuits". *IEEE Trans. on Microwave Theory and Techniques*, 29:1094–1098, Oct 1981.
- [22] K.C. Gupta and M.D. Abouzahra. "*Analysis and Design of planar Microwave Components*", chapter 3, pages 75–88. IEEE Press, 1994.

- [23] H.A. Wheeler. "Transmission Line Properties of Parallel Wide Strips by Conformal Mapping Approximation". *IEEE Trans. on Microwave Theory and Techniques*, 12(5):280–289, May 1964.
- [24] H.A. Wheeler. "Transmission Line Properties of Parallel Strips Separated by a Dielectric Sheet". *IEEE Trans. on Microwave Theory and Techniques*, 13(3):172–185, March 1965.
- [25] G. D'Inzeo , F. Giannini ,C.M Sodi and R. Sorrentino. "Method of Analysis and Filtering Properties of Microwave Planar Networks". *IEEE Trans. on Microwave Theory and Techniques*, 26(7):462–471, July 1978.
- [26] P.S. Hall J.R. James and C. Wood. "*Microstrip Antenna theory and design*". Peter Peregrinus, UK, 1981.
- [27] K.C. Gupta and M.D. Abouzahra. "*Analysis and Design of planar Microwave Components*", chapter 11, pages 473–493. IEEE Press, 1994.
- [28] G. Kumar and K.C. Gupta. "Broad-band Microstrip Antennas Using Additional Resonators Gap-Coupled to Radiating Edges". *IEEE Trans. on Microwave Theory and Techniques*, 32:1375–1379, 1984.
- [29] J.R. Mosig. Integral equation techniques. In T. Itoh, editor, "*Numerical Techniques for Microwave and Millimeter-wave Passive Structures*", chapter 3, pages 133–146. J. Wiley, 1989.
- [30] J.R. Mosig and F.E. Gardiol. "A Dynamic Radiation model for Microstrip Structures". *Advances in Electronics and Electron Physics*, 59:139–239, 1982.

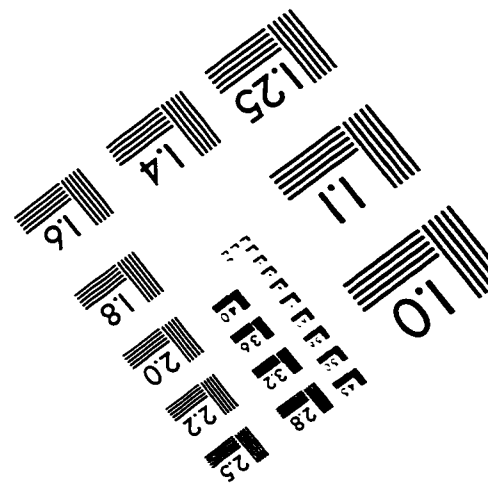
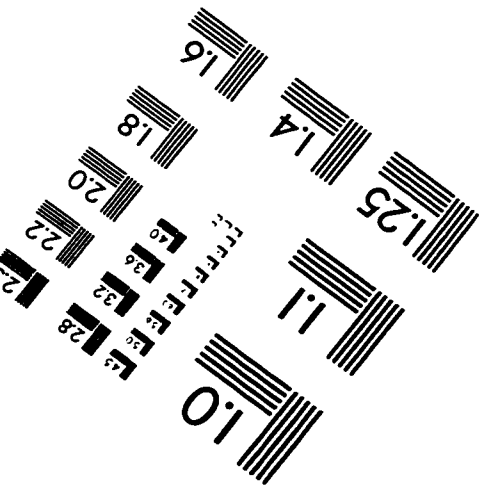
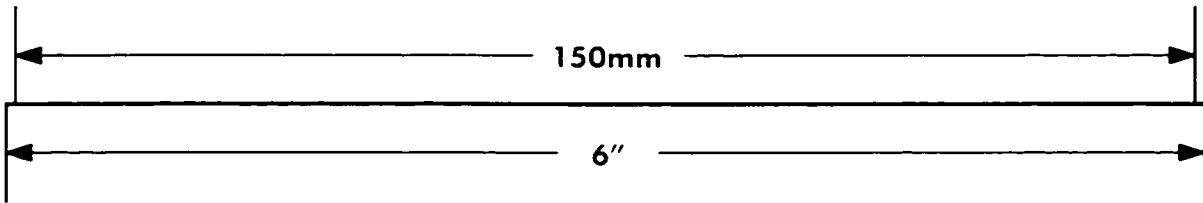
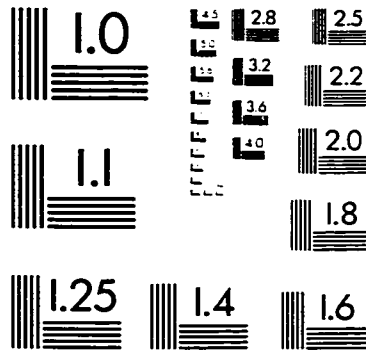
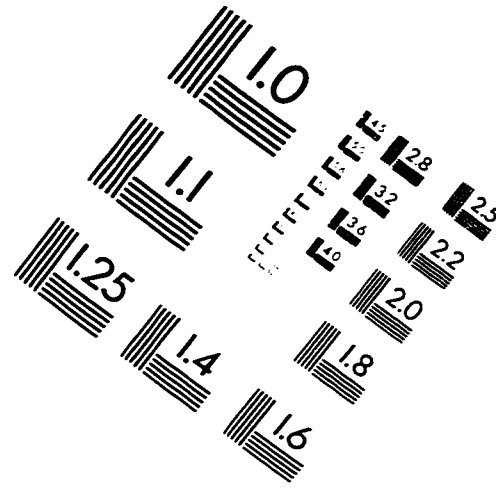
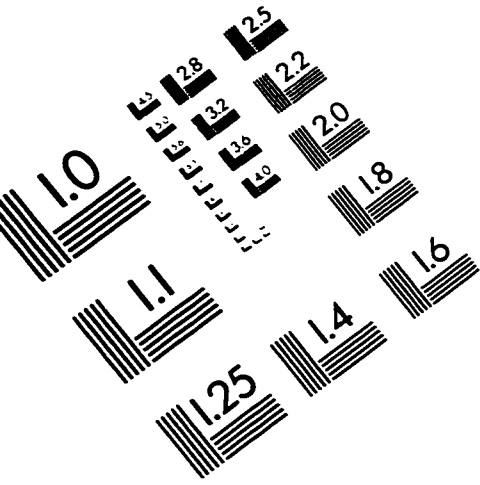
- [31] K.A. Michalski and D. Zheng. "Analysis of Microstrip Resonators of Arbitrary Shape". *IEEE Trans. on Microwave Theory and Techniques*, 42(7):1411–1418, July 1994.
- [32] I. Park, R. Mittra and M.I. Aksun. "Numerically Efficient Analysis of Planar Microstrip Configurations Using Closed Form Green's Functions". *IEEE Trans. on Microwave Theory and Techniques*, 43(2):314–324, Feb. 1995.
- [33] Y.L.Chow, J.J. Yang, D.G. Fang and G.E. Howard. "A Closed Form Spatial Green's Function for Thick Microstrip substrate". *IEEE Trans. on Microwave Theory and Techniques*, 39(3):588–593, March 1991.
- [34] N. Hojjat. "*The Green's Functions of a multilayer media in a simple computational form and it's application for Analyzing Microwave circuits*". PhD thesis, University of Tehran, Tehran, Iran, 1997.
- [35] F.Alessandria, M.Mongiardo and R Sorrentino. "Full wave modeling of via hole grounds in microstrip by three dimensional mode matching technique". *IEEE International Symposium on Microwave Theory and Techniques*, pages 1237–1240, Oct 1992.
- [36] R.M. Shubair. "*Efficient Analysis of Vertical and Horizontal Electric Dipoles in Multilayered Media*". PhD thesis, University of Waterloo, 1993.
- [37] A. Torabian-Esfahani. "Analysis for the Optimum Via Through a Ground Plane Hole Connecting Microstriplines on both sides". Master's Thesis, University of Waterloo, 1994.
- [38] R.F. Harrington. "*Time-Harmonic Electromagnetic Fields*". McGraw Hill, New York, 1961, pp. 98-103.

- [39] Y.L. Chow, A. Torabian-Esfahani and N. Hojjat. "Simulated Images for Multilayer Media, Complex Images without Prony's Method". *IEEE-APS*, pages 818-821, June 18-23, 1995.
- [40] Y.T.Lo, D.Solomon, and W.F. Richards. "Theory and Experiment on Microstrip Antennas". *IEEE Trans. on Antennas and Propagation*, 27:137-146, 1979.
- [41] S.C.Wu, N.G.Alexopoulos, and O.Fordham. "Feeding structure contribution to radiation by patch antennas with rectangular boundaries". *IEEE Trans. on Antennas and Propagation*, 40(10):1245-1249, Oct. 1992.
- [42] M.D. Abouzahra, and K.C. Gupta. "Multiport power divider-combiner circuits using circular-sector-shaped planar components". *IEEE Trans. on Microwave Theory and Techniques*, 36:1747-1751, 1988.
- [43] S.P.Yeo, M.S. Leong, P.S. Kooi, T.S. Yeo, and X.D. Zhou. "Contour Integral analysis of microstrip sectorial power divider (with arbitrary sector angle)". *IEE Proceedings - part H*, 140(1):62-65, Feb. 1993.
- [44] A. Torabian and Y.L. Chow. "A new method for analyzing sectorial power divider". *IEE-Electronics Letters*, 33(20):1713-1714, Sept. 1997.
- [45] L. Young G.L. Matthaei and E.M.T.Jones. "*Microwave Filters, Impedance-Matching Networks and Coupling Structures*". McGraw-Hill, 1964. pp 440.
- [46] K.C. Gupta, R. Garg, I. Bahl, and P. Bhartia. "*Microstrip Lines and Slotlines*". Artech House, 2nd edition, 1986, pp. 161 - 173.
- [47] T. Okoshi. "*Planar Circuits For Microwaves and Lightwaves*". Springer-Verlag, New York, 1985. pp 33-34.

- [48] Raafat R. Mansour. "Design of Superconductive Multiplexers Using Single-Mode and Dual-Mode Filters". *IEEE Trans. on Microwave Theory and Techniques*, 42(7):1411–1418, July 1994.
- [49] A. Torabian and Y.L. Chow. "Modeling of Narrow-Gap Coupling to a Patch Filter". *IEEE-APS*, pages 1744–1447, July 1997.
- [50] A. Torabian and Y.L. Chow. "Analysis of Arbitrary Gap Coupling in a Patch Filter". *Asia and Pasific Microwave Conf.*, pages pp. 797–800, Dec. 1997.
- [51] R.V. Churchill, J.W. Brown, R.F. Verhey. "*Complex Variables and Applications*". McGraw-Hill, third edition edition, 1974.
- [52] E. Jahnke, and F. Emde. "*Table of Functions with Formulae and curves*". Dover Publications, four edition, 1945.
- [53] M. Abramowitz and I.A. Stegun. "*Handbook of Mathematical Functions*". National Bureau of Standards, 1964.
- [54] R. Goyal. "*Monolithic Microwave Integrated Circuits: Technology and Design*". Artech House, Norwood, MA, 1989. Section 4.7.
- [55] Y.L. Chow. "An Approximate dynamic Spatial Green's Function in Three Dimensions for Finite Length microstrip Lines". *IEEE Trans. on Microwave Theory and Techniques*, 28:393–397, 1980.
- [56] A. Torabian and Y.L. Chow. "A Fast and Accurate Simulator for High Q Patch Resonators, Program and its user manual.". Technical report, University of Waterloo to Com Dev, Cambridge, Ontario, 1998.
- [57] T.Itoh. *Numerical Techniques for Microwave and Millimeter wave Passive Structures*, chapter 12, pages 203–206. John Wiley & Sons, 1989.

- [58] K.C. Gupta, R. Garg and R. Chadha. “*Computer Aided Design of Microwave circuits*”. Artech House, 1981, pp. 341 - 352.
- [59] R. R. Mansour, S. Ye, V. Dokas, B. Jolley, G. Thomson, W.C. Tang and C.M. Kudsia. “Design Consideration of Superconductiv Input Multiplexer for Satellite Applications”. *IEEE Trans. on Microwave Theory and Techniques*, 44(7):1213–1228, July 1996.
- [60] Y.L. Chow, R. Faraji-Dana, S.Safavi-Naeini and and N. Hojjat. “Spectral Green’s Functions for Multilayer Media in a Simple Form”. *IEEE-APS*, pages 1270–1273, June 18-23 1995.
- [61] A. Sommerfeld. “*Partial Differential Equations in Physics*”. Academic, NewYork, 1949.
- [62] Y.L. Chow, N. Hojjat, S.Safavi-Naeini and R. Faraji-Dana. “Spectral Green’s Functions for Multilayer Media in a convenient form”. *IEE - Proc. H*, 1(145):85–91, Jan. 1998.
- [63] R. Faraji-Dana. “*An Efficient and Accurate Green’s Function Analysis of Packaged Microwave Integrated Circuits*”. PhD thesis, University of Waterloo, 1993.
- [64] S. Ye and R.R. Mansour. “A Novel Split-Resonator High Power HTS Planar Filter”. *IEEE International Symposium on Microwave Theory and Techniques*, 1:299–302, June 1997.

IMAGE EVALUATION TEST TARGET (QA-3)



APPLIED IMAGE, Inc
1653 East Main Street
Rochester, NY 14609 USA
Phone: 716/482-0300
Fax: 716/288-5989

© 1993, Applied Image, Inc., All Rights Reserved